EPFL

Thèse n° 10 466

Probing unconventional performance of fiber resonators: light storage, generation and manipulation

Présentée le 23 mars 2021

Faculté des sciences et techniques de l'ingénieur
Laboratoire de systèmes photoniques
Programme doctoral en photonique

pour l'obtention du grade de Docteur ès Sciences

par

Ivan CARDEA

Acceptée sur proposition du jury

Prof. A. Radenovic, présidente du jury
Prof. C. S. Brès, directrice de thèse
Prof. K. Tsakmakidis, rapporteur
Prof. P. Petropoulos, rapporteur
Prof. L. Thévenaz, rapporteur

École polytechnique fédérale de Lausanne

2021

To my parents and my sister.

To my love Sabrina.

Ti solleverò dai dolori e dai tuoi sbalzi d'umore
Dalle ossessioni delle tue manie
Supererò le correnti gravitazionali
Lo spazio e la luce per non farti invecchiare.

I will relieve you from your pains and mood changes
From the obsessions of your quirks
I will overcome the gravitational currents
The space and light to keep you from getting old.

E guarirai da tutte le malattie
Perché sei un essere speciale
Ed io, avrò cura di te.

And you will heal from all the illnesses
Because you are a special (human) being
and I, will take care of you.

— da *La cura* di Franco Battiato

— from "La cura" by Franco Battiato

To the doctors and all healthcare professionals who, in these days, are risking their life
for taking care of people affected by the virus Sars-CoV-2.
Thank you.

Acknowledgements

The Doctorate is a journey full of experiences during which you learn to work either independently and, at the same time, with other people of different cultures and personalities. Who did not have the opportunity to make this journey, is probably wondering how it is. The answer to this question is obviously subjective and I will give you here my brief and sincere answer.

When you start the doctoral studies, you unconsciously think that there should be a right path that leads you to a successful result. Then, you quickly realize that there is not a unique path, a list of instructions to follow for becoming a researcher, a scientist or a professor. The always-good habit of hard working is certainly helpful but my experience taught me that, sometimes, it is not sufficient. I failed many times despite my hard work, but this does not mean it was not worth it. Your accomplishments are much more appreciated if you have failed along the way. In his last lecture at the Carnegie Mellon University, Prof. Randoulph Pausch said: "Even if you don't achieve your dreams, you can still get a lot by trying for it [...] the experience is what you get when you don't get what you wanted". Failure teaches to be humble, to look at things from different points of view, and more importantly, to listen to other people. People are fundamental in the scientific research. They bring an essential value to a work group, which is qualitatively more important than that of any technical equipment. A set of diverse expertise joined together can significantly increase the chance to achieve a successful result in a research work and, likely, in every field of work. At the time I am writing, millions of people are working together to take care of who is affected by COVID-19. The number of deaths in the world has overcome one million, and more than 70 thousand people are hospitalized. Therefore my first thought goes to these people and those who are continuously working to save lives.

My experience as a Ph.D. student had a strong impact on my life with many ups and downs. During these moments, my thesis director, Prof. Camille Brès, always offered me her support and supervision. One of the main skills a supervisor should have is the ability to behave differently depending on the student's personality. She has been capable to brilliantly do that, saying always the right words at the right moments. She believed in me even when the results I got were not promising. I sincerely thank her for

all the support she gave me and for the kindness she demonstrated in every situation.

My sincere thanks goes also to the president of the jury, Prof. Aleksandra Radenovic, and the jury members, Prof. Luc Thévenaz, Prof. Kosmas Tsakmakidis and Prof. Periklis Petropoulos, for reviewing on my work and providing helpful comments and suggestions.

I would also like to acknowledge Prof. Robert Boyd, Prof. Kosmas Tsakmakidis, Prof. Hatice Altug, Dr. Davide Grassani, Dr. Simon Fabbri, Dr. Jeremy Upham and Dr. Sebastian Schulz for their precious and valuable collaboration during these years.

This journey also offered me the opportunity to meet and work with other people. During these years, the PHOSL group has continuously grown integrating many co-workers with whom I had great times sharing experiences and opinions. I thank them all for the interesting discussions we have had and the support they gave me. I also would like to thank Madam Françoise Behn who helped me to orient myself in the big world of bureaucracy and, specially, for giving me some tips in improving my French. My office mate Eirini Tagkoudi deserves a special mention for being a friend as well as a colleague and for having contributed to a pleasant and "clean" coexistence in the office environment.

My special thanks goes to my parents and my sister who taught me the real values of life, which I always keep in mind. They sacrificed a lot for giving me the opportunity to study and have been always present when I needed their help. I will always thank them for leaving me free to make my own choices.

I could probably spend at least another page to acknowledge my soulmate Sabrina, since all my accomplishments during my Ph.D. studies would have not been possible without her support. I will only say that a picture of her and some post-its with her words are attached on the screen of my office computer, so that I can read them whenever I need her comfort.

Lausanne, 22 October 2020 Ivan Cardea

Abstract

This thesis aims at investigating the performance of figure-9 (figure-of-nine) optical fiber resonators as a practical solution for light storage, light generation and manipulation. The first part of the thesis focuses on a theoretical and experimental study describing the performance of the figure-9 laser as a function of different coupling strengths and output coupling conditions. The study provides new insights on Sagnac interferometer-based fiber lasers, which can be useful also for other types of cavities that include this structure, such as the figure-8 (figure-of-eight) or the theta cavity laser. The work on the figure-9 laser is then followed by a generalized theoretical model, validated by numerical results, to demonstrate that resonant systems with a decoupled input and output energy rates can exhibit an arbitrarily high time-bandwidth performance, thus providing a longer delay/storage time. The developed model shows that the time-bandwidth product (TBP) of such a resonant system is only limited by the cavity finesse. This description fits with the time-bandwidth limit (TBL), which states that the cavity bandwidth $\Delta\omega_{\mathrm{cav}}$ is the inverse of the photon lifetime τ (i.e. $\Delta\omega_{\mathrm{cav}} \cdot \tau = 1$), only when the resonator is reciprocal. The results also show that a longer storage time is accompanied by a significant improvement of the intra-cavity power enhancement, with respect to that provided by a reciprocal resonator, which is strongly desirable in all the applications that demand high efficiency in nonlinear processes. By comparing the total power enhancement in the reciprocal and nonreciprocal case, we prove that the TBP can be used as a figure of merit that characterizes the gain of total power enhancement, attained over one free spectral range (FSR) through nonreciprocal coupling, with respect to the reciprocal case considering the same amount of in-coupled power. The model is then used as a reference for an experimental implementation of such a system, at telecommunication wavelengths (around $1.55\,\mu\mathrm{m}$), using a time-variant figure-9 cavity. The results report a TBP that exceeds by a factor of 30 the TBL and is limited only by experimental constraints of the setup used. Lastly, the Sagnac interferometer in the context of generation of light is explored as to achieve electro-optic comb generation with a flat-topped spectral shape.

Keywords: Figure-9 resonator, figure-9 laser, Sagnac interferometer, nonlinear amplifying loop mirror, time-bandwidth product, time-bandwidth limit, nonreciprocal coupling, time-reversal symmetry, electro-optic frequency combs.

Résumé

Cette thèse vise à étudier les performances des résonateurs à fibre optique à figure-9 (figure-de-neuf) en tant que solution pratique pour le stockage, la génération et la manipulation de la lumière. La première partie de la thèse se concentre sur une étude théorique et expérimentale décrivant les performances du laser à figure-9 en fonction de différentes forces de couplage et conditions de couplage de sortie. L'étude fournit de nouvelles informations sur les lasers à fibre à base d'interféromètre de Sagnac qui peuvent être utiles également pour d'autres types de cavités qui incluent cette structure, comme le laser à figure-8 (figure-de-huit) ou le laser à cavité theta. Le travail sur le laser figure-9 est ensuite suivi d'un modèle théorique généralisé, validé par des résultats numériques, pour démontrer que les systèmes résonants avec des débits d'énergie d'entrée et de sortie découplés peuvent présenter des performances temps-bande arbitrairement élevées, offrant ainsi un temps de retard/stockage plus long. Le modèle dévelopé montre que le produit temps-band (PTB) d'un tel système résonnant n'est limité que par la finesse de la cavité. Cette description correspond à la limite de temps-bande (LTB), qui indique que la bande passante de la cavité $\Delta\omega_{\mathrm{cav}}$ est l'inverse de la durée de vie du photon τ (c'est à dire : $\Delta\omega_{\mathrm{cav}} \cdot \tau = 1$), seulement quand le résonateur est réciproque. Les résultats montrent également qu'un temps de stockage plus long s'accompagne d'une amélioration significative de l'augmentation de puissance intra-cavité, par rapport à celui fourni par un résonateur réciproque, ce qui est fortement souhaitable dans toutes les applications qui exigent une efficacité élevée dans les processus non linéaires. En comparant l'augmentation de puissance totale dans le cas réciproque et non réciproque, nous prouvons que le PTB peut être utilisé comme une facteur de mérite qui caractérise le gain d'augmentation de puissance totale, atteint sur un free spectral range (FSR) par couplage non réciproque, par rapport au cas réciproque en considérant la même quantité de puissance couplée. Le modèle sert ensuite de référence pour une implémentation expérimentale d'un tel système, aux longueurs d'onde de télécommunication (environ $1.55\,\mu\mathrm{m}$), utilisant une cavité à figure-9 temps-variant. Les résultats rapportent un PTB qui dépasse d'un facteur 30 le LTB et n'est limité que par les contraintes expérimentales du setup utilisé. Enfin, l'interféromètre de Sagnac dans le contexte de la génération de lumière est exploré pour obtenir une génération de peigne électro-optique avec une forme spectrale à

sommet plat.

Mots clefs : Résonateur à figure-9, laser à figure-9, interféromètre de Sagnac,miroir de boucle d'amplification non linéaire, produit temps-band, limite de temps-bande, couplage non réciproque, symétrie d'inversion du temps, peignes de fréquence électro-optiques.

List of Publications

Journal articles

1. **Cardea I.**, Grassani D., Fabbri S. J., Upham J., Boyd R. W., Altug H., Schulz S. A., Tsakmakidis K. L., & Brès C. S., Arbitrarily high time bandwidth performance in a nonreciprocal optical resonator with broken time invariance, *Sci. Rep.* 10, 15752 (2020).

2. **Cardea I.**, Grassani D., Upham J., Schulz S. A., Tsakmakidis K. L., & Brès C. S., Unconventional time-bandwidth performance of resonant cavities with nonreciprocal coupling, *Physical Review A*, (2020), (*accepted*).

3. Lacava C., **Cardea I.**, Demirtzioglou I., Khoja A. E., Ke L., Thomson D. J., Ruan X., Zhang F., Reed G. T., Richardson D. J., & Petropoulos P., 496 Gb/s direct detection DMT transmission over 40 km single mode fibre using an electrically packaged silicon photonic modulator, *Opt. Express* 25, 29798-29811 (2017).

Conference proceedings

1. **Cardea I.**, Kharitonov S. & Brès, C. S. Experimental and theoretical investigation of the operating principles of the Figure-9 laser, in *Advanced Photonics Congress* 2018 (OSA, 2018), SoW2H.6.

2. **Cardea I.**, Grassani D., Upham J., Boyd R. W., Schulz S. A., Tsakmakidis K. L., & Brès C. S., Theoretical and numerical study of the time-bandwidth product in resonant cavities with nonreciprocal coupling, in *Conference on Lasers and Electro-Optics, OSA Technical Digest* (Optical Society of America, 2020), STh4J.4.

3. Grassani D., **Cardea I.**, Fabbri S. J., Upham J., Boyd R. W., Altug H., Schulz S. A., Tsakmakidis K. L., & Brès C. S., Demonstration of ultra-high time-bandwidth product in a non-reciprocal fiber-optic system, in *Frontiers in Optics / Laser Science, OSA Technical Digest* (Optical Society of America, 2018), JTu3A.32.

4. Schulz S. A., Grassani D., **Cardea I.**, Fabbri S. J., Upham J., Boyd R. W., Tsakmakidis K. L., & Bres C. S., Optical delay beyond the time-bandwidth limit: From pipe dream to reality, in *Int. Conf. Transparent Opt. Networks* (IEEE Computer Society, 2019), We.B4.2 ⧉.

5. S. A. Schulz, Grassani D., **Cardea I.**, Fabbri S. J., Upham J., Boyd R. W., Tsakmakidis K. L., & Bres C. S., "Overcoming the time-bandwidth limit," *2018 IEEE British and Irish Conference on Optics and Photonics (BICOP)*, (2018), doi: 10.1109/BICOP.2018.8658316 ⧉.

6. Lacava C., Demirtzioglou I., **Cardea I.**, Khoja A. E., Li K., Thomson D. J., Ruan X., Zhang F., Reed G. T., Richardson D. J., & Petropoulos P., Spectrally Efficient DMT Transmission over 40 km SMF Using an Electrically Packaged Silicon Photonic Intensity Modulator, in *European Conference on Optical Communication, ECOC*. (2018), doi: 10.1109/ECOC.2017.8345965 ⧉.

Contents

List of Figures

List of Tables

Acronyms

- ADMR Add-drop micro-ring resonator
- AWG Arbitrary waveform generator
- CW Clockwise
- CCW Counter-clockwise
- DD-MZM Dual-drive Mach-Zehnder modulator
- EDFA Erbium-doped fiber amplifier
- EO Electro-optic
- EOM Electro-optic modulator
- ESA Electrical spectrum analyzer
- FBG Fiber Bragg grating
- FP Fabry-Perot
- FSR Free spectral range
- FWHM Full width at half maximum
- GT Gires-Tournois
- GU Gain unit
- IM Intensity modulator
- LIDAR Laser Imaging Detection and Ranging
- MLL Mode-locked laser
- MZM Mach-Zehnder modulator

- NALM Nonlinear amplifying loop mirror
- NOLM Nonlinear optical loop mirror
- OFC Optical frequency comb
- OSA Optical spectrum analyzer
- OSNR Optical signal-to-noise ratio
- PC Polarization controller
- PCF Power coupling formalism
- PM Phase modulator
- PS Phase shifter
- RF Radio frequency
- RT Round trip
- SESAM Semiconductor saturable absorber mirror
- TBL Time-bandwidth limit
- TCMT Temporal coupled-mode theory
- TBP Time-bandwidth product
- WDM Wavelength division multiplexer

1 Introduction

1.1 Thesis motivation

Signal generation, processing and storing are the main tasks required (not necessarily together) by any kind of optical system. These tasks involve the generation, storage and manipulation of light, subjects that cover most of the scientific research in Photonics. Although the generation of light has reached an unquestionable level of maturity, thanks to the growing and rapid development of light sources and lasers, it still remains among the most investigated research topics. In particular, fiber lasers have received increasing attention during the last thirty years, due to their undoubted advantages compared to traditional solid-state lasers. They are becoming one of the most used sources in various applications including distributed [1] and remote sensing [2], material processing, spectroscopy, medicine [3]. A key factor that contributed to the rapid technological evolution of fiber lasers is the well-established class of gain media represented by the rare-earth doped optical fibers, which provide very broad absorption and emission lineshapes. Moreover, multimode semiconductor diode lasers used as optical excitation for the gain medium are efficient and low-cost devices, and available for most of the absorption bands of the rare-earth doped materials.

The storage of energy through the alteration of the speed of a light wave or simply by spatial confinement is one of the most intricate missions in Photonics. The capability to slow down or trap light without imposing an excessive distortion to the signal is a key tool of many research areas such as optical communications [4, 5], quantum information processing [6], metamaterials [7] and photovoltaics [8–10]. In particular, it is of fundamental importance in all the applications requiring optical signal processing or light storage [11–17]. For instance, in wavelength division multiplexed (WDM) multichannel systems, the temporary storage of data has proved necessary to overcome critical problems such as synchronization and packet contention resolution. Storage devices and delay lines are used at the receiver end to store high-rate data packets as they are read out at a slower rate or for queuing while the transmitter awaits access to

the network [18, 19]. Optical buffers have also been considered in other research fields such as optical computing or short-range optical transmission systems, where they are useful to store large amounts of data transmitted from different sources (cameras, RF over fiber, etc.) without passing through optoelectronic conversion. However, despite the significant efforts made to enable the all-optical transport of data, switching and routing are still operations mostly performed in the electrical domain. Light trapping is even more crucial for energy technology. In fact, the performance in trapping and absorbing light strongly affect the efficiency of photovoltaic solar-energy conversion. In this sense, photonic crystals have been proved a promising technology as they can provide a photocurrent four times higher than a standard thin-film silicon solar cell built with the same amount of silicon [8, 20].

Generally, what is required from the practical point of view is the ability to impart a delay to a signal that is independent of the signal's bandwidth. The easiest way to fulfill this requirement is to use a long piece of waveguide such as an optical fiber. However, to delay a telecom pulse for $1\ \mu$s, the length of a silica optical fiber must be of the order of 200 meters, a value that is considerably large in terms of footprint. A light pulse can also be delayed, while keeping the device footprint relatively small, by circulating it through many round trips in a resonator, which may be in the form of a ring resonator or as a defect mode in a photonic crystal. As already discussed, there are two main requirements that an ideal delay line needs to fulfill: it should provide a large delay and it should operate over a wide range of frequencies with low insertion loss. In the last two decades, different implementations of resonant structures have been explored for the realization of delay lines and storage devices [21–27]. As it is well known, increasing the interaction time requires the cavity bandwidth to be proportionally narrow. However, this leads to a constraint that unavoidably imposes a trade-off between the storage/delay time achievable and the width of the operational spectral bandwidth [28–30]. In mathematical terms, this trade-off is described by the time-bandwidth limit (TBL), a fundamental rule that arises from Fourier-reciprocity considerations, which dictates that the time-bandwidth product (TPB) must be $\Delta\omega \cdot \tau = 1$, with $\Delta\omega$ the system bandwidth and τ the energy decay time [31–33]. Both high-finesse and losses limit the storage capacity of microresonator-based devices [34]. Any attempt to realize broadband devices that provide a considerable delay, without suffering too much the limitations produced by dispersion and losses, means that somehow this seemingly fundamental rule needs to be overcome. A TBP larger than 1 offers the capability to control the storage time without suffering from the restriction dictated by the cavity bandwidth. This allow to release the system from the compromise imparted by the TBL that prevent to realize an ideal delay line. One more benefit that would follow from realizing a TBP > 1, stems from considerations on the power balance of the resonant system. In fact, light confined in a localized spatial region is also accompanied by a dramatic increase of the energy stored within the resonator. This is crucial specially in nonlinear optics applications, such as frequency comb and Kerr soliton generation

[35, 36], where a large intra-cavity power enhancement factor reduces the input power required to reach the threshold for nonlinear effects.

An alternative approach for delaying a light pulse is to reduce the group velocity of the signal by exploiting strong resonances resulting from energy transfer between the electromagnetic wave and the medium (atomic resonances) or between two or more modes of the electromagnetic radiation (photonic resonances). A propagating wave packet having a central frequency in the vicinity of one of these strong resonances experiences a significant reduction of its group velocity, the so called "slow light phenomenon", owing to a large variation of the refractive index [11]. Over the last twenty years, several slow light schemes aiming at overcoming the TBL have been proposed, where the resonances exhibit an optical [37–43] or electronic nature [44–47]. They were proven capable of providing performance beyond the TBL by exploiting the characteristic refractive index dispersion near resonances, due to the intrinsic electronic transitions or induced by stimulated Brillouin or Raman scattering, or Bragg reflections in periodic structures [11–13, 15, 21, 48]. However, despite the initial excitement for their promising benefits of being capable to support relative wide-band signals, they are not yet considered as the definitive technology for the realization of ideal delay lines. In fact, these systems are still characterized in terms of a group-index–bandwidth limit [14] or a time-delay–bandwidth–footprint limit. In both of these terms, slow-light waveguides are intrinsically limited, and – similarly to resonant systems – the achievable delay times remain inversely proportional to (a power of) the guide's bandwidth, $\Delta t \sim \Delta\omega^{-\alpha}$, where typically $\alpha = 2$ or 3 [11, 29, 30]. Here, the trade-off arises from pulse temporal broadening owing to various dispersion phenomena (2nd and 3rd order dispersion, dispersion of gain/absorption), preventing significant slowing-down (i.e., storage times) of broadband signals.

Recently, a theoretical proposal [49] was put forward stating that the TBL can be overcome by breaking Lorentz reciprocity [50, 51] in a resonant system in which the input and output energy rates are decoupled one from the other. In such a system, it was shown that the TBL can be exceeded by orders of magnitude, without accompanying adiabaticity or signal distortion limitations. The theoretical proposal has reinvigorated an avid, and still ongoing, debate about whether (or not) the time-bandwidth limit can indeed be exceeded in resonant systems, by considering symmetry, mode coupling and even thermodynamics-based arguments [52–55]. However, much of this recent, and fully theoretical, activity has focused on nonreciprocal but *time-invariant* resonant systems.

1.2 Thesis goal and description of the work

This thesis aims at investigating the performance of figure-9 (said figure-of-nine) optical fiber resonators as a practical solution for light storage, light generation and

manipulation. A figure-9 cavity, consists of a Sagnac interferometer connected to a highly reflective element. The Sagnac interferometer has been widely used in the past for the realization of optical gyroscopes [56]. More recently, this type of structure has also attracted interest, for the development of nonlinear all-optical switches, where the nonlinear switch is obtained, via optical Kerr effect, exploiting the relative phase shift between the two counter-propagating waves. An interferometer in a Sagnac configuration has the unique feature of providing the same physical path for the two counter-propagating waves. This allows to remove all the issues due to path instabilities that are caused by environmental disturbances. A Sagnac interferometer can easily turn into a laser cavity by placing a doped fiber inside the loop and connecting a highly reflecting element to one of the input ports of the coupler, thus earning it the moniker of figure-9 cavity. This type of laser, first proposed by Cowle et al. [57], offers a clear benefit in terms of simplicity of the configuration since it requires only one reflective element or even none if one uses a fiber loop mirror. As a consequence, figure-9 cavities can be fully fiberized and thus robust. The figure-9 laser has been intensively investigated to develop pulsed fiber lasers. Mode-locking operation has been demonstrated using a figure-9 cavity with a SESAM (semiconductor saturable absorber mirror) at the place of the reflective element [58]. The SESAM is used to initiate the mode-locking, while the doped fiber placed within the Sagnac loop acts as a nonlinear amplifying loop mirror (NALM) leading to a significant suppression of the pulse pedestal. In a recent work carried out by Kharitonov et al. [59], a dissipative soliton resonance (DSR) mode-locked laser was built using this layout with a Thulium-doped fiber, obtaining nanosecond pulses with a record value of the pulse energy, for this type of laser, of 400 nJ. Despite the wide interest aroused by such lasers, very little efforts have been made to fully understand their performance, in particular, the interesting aspect of the influence of the coupling ratio of the output coupler. Therefore the first part of this thesis work was devoted to a theoretical and experimental investigation of the performance of this type of laser at different coupling conditions.

The deep understanding of the operating principles of the figure-9 cavity was then used to pursue the objective of the light storage. Moved by this objective, we first carried out a theoretical study on a resonant system with a nonreciprocal coupling interface to unveil the condition required for overcoming the TBL. The topic was addressed by developing a time-variant figure-9 resonator since it represents one of the simplest methods to realize a resonant system with a nonreciprocal coupling interface. In fact, the reflection and transmission coefficients of the figure-9 cavity can be easily changed in time by just imparting a phase difference between the two wave traveling within the fiber loop. The time-bandwidth performance of the resonator was evaluated through a detailed theoretical study, supported by numerical simulations, followed by an experimental implementation. Overall the study aimed at providing an accurate understanding of the benefits of the nonreciprocal coupling on the time-bandwidth performance of a resonant system.

The last part of the thesis is focused on the generation and equalization of electro-optic (EO) frequency combs. The equalization of EO frequency combs plays an important role in all those applications where even a power difference of few dB between each comb line can represent a measurement handicap. Several methods aiming at generating flat EO combs have been proposed, but all of them require the use of two or more EO modulators (EOMs) [60–66] or a further processing of the driving RF signal [67–70]. In the wake of realizing a more simple and cost-effective scheme, we developed a system capable of providing flat-topped EO frequency combs using only one phase modulator integrated in a fiber optic Sagnac interferometer.

1.3 Thesis structure

Chapter 2 contains all the fundamental basics required to understand the content of the thesis. It starts with a description of passive optical resonators using two different approaches: the power coupling formalism and the temporal coupled-mode theory. Then the discussion moves towards the main characteristics of fiber lasers. **Chapter 3** covers the theoretical and experimental investigation on the figure-9 laser. The chapter begins with the description of the theoretical model of the laser and ends with a comparison of the theory with the experimental results. In **chapter 4** I introduce the theoretical model of a generic resonant system based on a Fabry-Perot structure. Through an analysis of the frequency response and power balance of the resonator the model provides the required conditions on how to overcome the TBL by implementing a nonreciprocal coupling interface. Numerical simulations are also presented to support the work, confirming the results of the theory. This analytical work is then put in practice in **chapter 5**, where an arbitrarily high TBP is demonstrated using the resonant system described in chapter 4. Moreover, the reported results are compared with numerical simulations to demonstrate that the TBP of such a resonant system is only limited by the cavity finesse when the intra-cavity losses are kept sufficiently low. In **chapter 6**, we exploit the characteristics of the Sagnac interferometer to develop a system for the generation and equalization of electro-optic frequency combs. The motivation of this scheme is explained by the significant improvement in terms of complexity and cost of the entire system, compared to other approaches proposed in literature. The quality and effectiveness of the frequency combs obtained with such a system are then compared to those generated from a single-stage phase modulator in terms of maximum power variation over the comb lines.

2 Analytical models of passive and active optical resonators

Optical resonators, in their passive configuration, are generally used to confine and store light over a certain frequency range. Their structure forces light to propagate repeatedly within its boundaries, resulting in a regenerative feedback of the electromagnetic wave that enhances the interaction between light and matter. An essential aspect of trapping electromagnetic energy within a resonant cavity, is the efficiency of the coupling process. Specifically, the total power that can be transferred into a conventional resonator depends on the coupling coefficient of each coupling element and the intra-cavity losses experienced by a given resonant mode. The design and implementation of the coupling elements is therefore crucial for the realization of resonant structures that must be capable of efficiently trap the electromagnetic energy over a certain spectral bandwidth.

Optical resonators also represent a key element of a laser system. They have the fundamental task of providing, under specific conditions on the balance between gain and loss, the positive feedback for the laser oscillation, thus turning a simple amplifier into an optical oscillator. Moreover, the optical resonator is responsible for the spectral selectivity of the laser beam and the sharpness of the resonance mode, two characteristics that play a crucial role in many research areas and practical applications.

This chapter aims at providing a fundamental background for a complete understanding of the experimental and theoretical work included in this thesis. The discussion starts with an introduction to the physics of resonant cavities analyzing two different approaches for the evaluation of the transfer characteristic and key parameters of a generic passive optical resonator. Then we will have a look into the working principles of an optical oscillator by examining and modeling an optical resonator that includes a gain medium. The chapter ends with a general description of the characteristics of a fiber laser, which is the topic of the next chapter.

2.1 Analytical model of an optical resonator according to the power coupling formalism

Optical resonators have been intensively investigated since the birth of photonics. In general, two main formalisms are used for their analysis depending on the case of study: the energy coupling formalism, also known as temporal coupled-mode theory (TCMT) [31, 71–73], and the power coupling formalism [74, 75]. In the energy coupling formalism the response of the resonant system is derived considering the energy exchange between the resonator and the external bus waveguides, that is quantitatively represented by the rates of energy coupled into and out of the resonator. The power coupling formalism is based on the analysis of the power exchange between the resonant system and the external waveguides. In this case the coupling junctions are modeled by lumped coupling elements described by proper coupling coefficients, which, in the case of a directional coupler, can be retrieved from the solution of the coupled mode equations in space [31, 75].

2.1.1 S-parameters of a generic coupling element

Transmission and reflection at the boundaries between different media are the primary aspects to consider when treating the coupling of light inside a cavity. To understand how energy is transferred to an optical resonator we need the transfer characteristic of the coupling element, which represents the interface element between the cavity and the outside world. This coupling element can be, for instance, a directional coupler, a partially reflecting mirror or a simple thin dielectric slab.

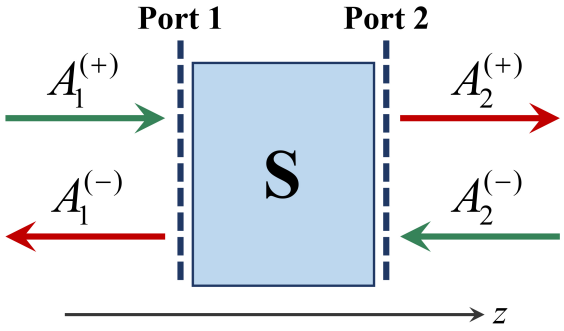

Figure 2.1 – Two-port optical device representing a generic coupling element of a resonant system. The transfer characteristic of the device is obtained from the scattering matrix **S**.

Let us represent this coupling element as a generic two-port optical system, as depicted in Fig. 2.1, and express the complex fields of the outgoing waves A_2^+ and A_1^- in terms of those of the incoming waves A_1^+ and A_2^-. The subscript 1,2 indicates the corresponding input/output port, while the superscript symbol +,- indicates if the wave propagates

towards the positive or negative direction of the z axis. Using the *scattering matrix formalism* [76] we can relate these four fields as follows:

$$\begin{bmatrix} A_2^+ \\ A_1^- \end{bmatrix} = \begin{bmatrix} \mathrm{t}_{12} & \mathrm{r}_{21} \\ \mathrm{r}_{12} & \mathrm{t}_{21} \end{bmatrix} \begin{bmatrix} A_1^+ \\ A_2^- \end{bmatrix} \tag{2.1}$$

where the parameters t_{12} and r_{12} are the complex transmission and reflection coefficients, respectively, of a wave incident from port 1, while t_{21} and r_{21} are the complex transmission and reflection coefficients, respectively, of a wave incident from port 2. We can write Eq. 2.1 in a more compact form as:

$$\mathbf{A}_{\mathrm{out}} = \mathbf{S} \times \mathbf{A}_{\mathrm{in}} \tag{2.2}$$

where $\mathbf{S}$ is the scattering matrix, while $\mathbf{A}_{\mathrm{in}}$ and $\mathbf{A}_{\mathrm{out}}$ are the vectors of the complex amplitudes of the incoming and outgoing waves respectively. In general, for a multi-port system, the diagonal elements t_{ij} of the $\mathbf{S}$ matrix represent the complex transmission coefficients of a wave entering and exiting the system from port i and j respectively, while the off-diagonal elements r_{ij} are the reflection coefficients at each port i.

Energy conservation and symmetry relations

The optical powers of the incoming and outgoing waves are given by the square magnitudes of their complex amplitudes $|A_{1,2}^{\pm}|^2$. Using the matrix notation we can write the power flowing out of the optical system as a function of the complex amplitudes of the incoming waves and the scattering matrix:

$$P_{\mathrm{out}} = \mathbf{A}_{\mathrm{out}}^{\dagger}\,\mathbf{A}_{\mathrm{out}} = (\mathbf{S}\,\mathbf{A}_{\mathrm{in}})^{\dagger}(\mathbf{S}\,\mathbf{A}_{\mathrm{in}}) = (\mathbf{A}_{\mathrm{in}}^{\dagger}\mathbf{S}^{\dagger})(\mathbf{S}\,\mathbf{A}_{\mathrm{in}}) = \mathbf{A}_{\mathrm{in}}^{\dagger}(\mathbf{S}^{\dagger}\mathbf{S})\mathbf{A}_{\mathrm{in}} \tag{2.3}$$

where the symbol † as superscript denotes the *transpose conjugate* of the vector. In deriving Eq.2.3, the following rules have been used: (i) the associative property of the matrix multiplication i.e. $\mathbf{A}(\mathbf{BC}) = (\mathbf{AB})\mathbf{C}$ and (ii) the equivalency between the transpose conjugate of any vectorial product and the product of the individual conjugate of each vector taken in reverse order, i.e. $(\mathbf{ABC})^{\dagger} \equiv \mathbf{C}^{\dagger}\mathbf{B}^{\dagger}\mathbf{A}^{\dagger}$. If the optical system is lossless, this relation must ensure the conservation of energy, meaning that the power flowing out of the system must be equal to the total input power, which is just $P_{\mathrm{in}} = \mathbf{A}_{\mathrm{in}}^{\dagger}\,\mathbf{A}_{\mathrm{in}}$. This leads to a condition on the scattering matrix of the system which dictates that the inverse of the $\mathbf{S}$ matrix must be equal to its transpose conjugate, i.e. $\mathbf{S}$ must be a *unitary matrix* [50]:

$$\mathbf{S}^{\dagger} \equiv \mathbf{S}^{-1} \qquad \text{or} \qquad \mathbf{S}^{\dagger}\mathbf{S} = \mathbf{I} \tag{2.4}$$

where $\mathbf{I}$ represents the identity matrix. Most common optical components used as coupling elements are also *reciprocal*, meaning that the transmission and reflection

in the two directions are identical. Specifically, the scattering parameters of a lossless reciprocal two-port optical system must obey the following relations [76]:

$$|t_{12}| = |t_{21}| \equiv |t|, \quad |r_{12}| = |r_{21}| \equiv |r|, \quad |t|^2 + |r|^2 = 1, \quad t_{12}r_{21}^* + r_{12}t_{21}^* = 0 \tag{2.5}$$

These relations must be satisfied by any coupling element that is lossless and reciprocal. Standard optical devices such as highly reflective optical mirrors, directional couplers and beam splitters, for which the internal losses are sufficiently small to be neglected, fall in this category.

2.1.2 Frequency response of a Fabry-Perot resonator

In order to derive the frequency response of an optical resonator we can consider its simplest form: the Fabry-Perot (FP) cavity, which consists of two parallel planar mirrors enclosing a center medium characterized by a refractive index n_c. Although this structure is a simplification rather than a generalization of a generic optical resonator, we will see later on, that this configuration is fundamentally equivalent to other resonator layouts and the equations we will obtain are also valid, with the appropriate equivalencies, for optical resonators of different kind. An illustration of the FP resonator is depicted in Fig. 2.2. Let L_d be the distance between the two mirrors, so that the total length of one cavity round-trip is then $L_{RT} = 2L_d$.

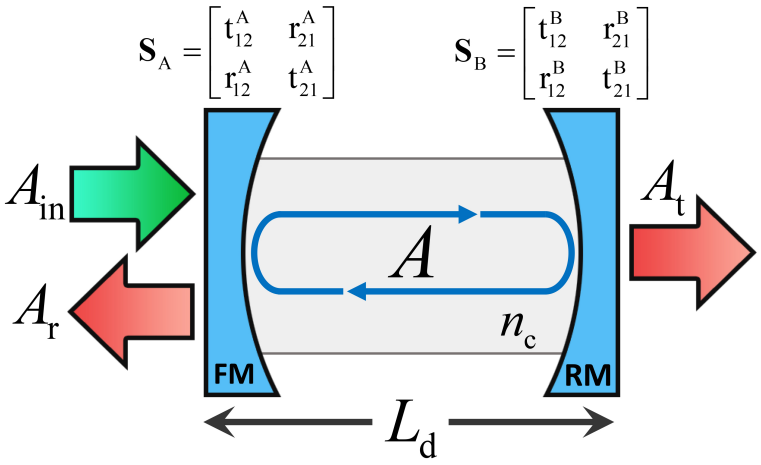

Figure 2.2 – Schematic illustration of a Fabry-Perot resonator enclosing a medium with refractive index n_c. FM: front mirror; RM: rear mirror.

Light incident on this structure bounces back and forth between the two mirrors repeatedly and, under specific conditions on the frequency, interferes with the new incoming light from the front mirror.

To determine the total power transmitted and reflected by the FP cavity let us consider

a monochromatic light wave of frequency ω normally incident on the front mirror of the resonator. Its electric field $\mathbf{E}_{\text{in}}(\mathbf{r},t)$ can be expressed as:

$$\mathbf{E}_{\text{in}}(\mathbf{r},t) = E_0\mathbf{A}(x,y)e^{j(\omega t-\beta z)} \tag{2.6}$$

In this expression $\mathbf{A}(x,y)$ describes the transverse spatial distribution of the electric field, β is the propagation constant along the direction of propagation z, which corresponds to the longitudinal axis of the resonator. We then define the complex amplitude of the wave as:

$$A_{\text{in}} = E_0 e^{-j\beta z} \tag{2.7}$$

and the scattering matrices of the front and rear mirror respectively as:

$$\mathbf{S}_{\text{A}} = \begin{bmatrix} \text{t}_{12}^{\text{A}} & \text{r}_{21}^{\text{A}} \\ \text{r}_{12}^{\text{A}} & \text{t}_{21}^{\text{A}} \end{bmatrix} \qquad \mathbf{S}_{\text{B}} = \begin{bmatrix} \text{t}_{12}^{\text{B}} & \text{r}_{21}^{\text{B}} \\ \text{r}_{12}^{\text{B}} & \text{t}_{21}^{\text{B}} \end{bmatrix} \tag{2.8}$$

whose parameters, we recall, are complex quantities. For a cleaner form of the equations that will follow, let us rewrite these scattering matrices as:

$$\mathbf{S}_{\text{A}} = \begin{bmatrix} \text{t}_{\text{A}} & \text{r}'_{\text{A}} \\ \text{r}_{\text{A}} & \text{t}'_{\text{A}} \end{bmatrix} \qquad \mathbf{S}_{\text{B}} = \begin{bmatrix} \text{t}'_{\text{B}} & \text{r}_{\text{B}} \\ \text{r}'_{\text{B}} & \text{t}_{\text{B}} \end{bmatrix} \tag{2.9}$$

where the apostrophe indicates that the coefficient is related to the wave coming from inside the cavity. Using these scattering matrices, we can calculate the complex amplitudes of the reflected wave at every cavity round-trip [75]:

$$\begin{aligned} A_{1\text{r}} &= \text{r}_{\text{A}} A_{\text{in}} \\ A_{2\text{r}} &= \text{t}_{\text{A}}\text{t}'_{\text{A}}\text{r}'_{\text{B}} a_{\text{RT}} A_{\text{in}} e^{-j\phi_{\text{RT}}} \\ A_{3\text{r}} &= \text{t}_{\text{A}}\text{t}'_{\text{A}}\text{r}'_{\text{A}}\text{r}'^{2}_{\text{B}} a^2_{\text{RT}} A_{\text{in}} e^{-j2\phi_{\text{RT}}} \\ &\vdots \\ A_{\text{Nr}} &= \text{t}_{\text{A}}\text{t}'_{\text{A}}\text{r}'^{(N-2)}_{\text{A}} (\text{r}'_{\text{B}} a_{\text{RT}})^{(N-1)} A_{\text{in}} e^{-j(N-1)\phi_{\text{RT}}} \end{aligned} \tag{2.10}$$

where $a_{\text{RT}} = e^{-(\alpha/2)L_{\text{RT}}}$ is the intra-cavity attenuation factor (with α being the attenuation constant), that describes the exponential attenuation of the optical field over one cavity round-trip due to absorption and scattering losses occurring in the intra-cavity medium, while $\phi_{\text{RT}} = \beta L_{\text{RT}}$ is the round-trip phase delay experienced by the wave during one cavity round-trip. The first of equations 2.10 is the complex amplitude of the field directly reflected from the front mirror, while the other expressions represent the multiple reflections between the two mirrors. The total overall reflection is given

by the sum of all these contributions:

$$A_r = A_{in}\{r_A + t_A t'_A r'_B a_{RT} e^{-j\phi_{RT}}[1 + (r'_A r'_B a_{RT} e^{-j\phi_{RT}}) + (r'_A r'_B a_{RT} e^{-j\phi_{RT}})^2 + \cdots \\ \cdots + (r'_A r'_B a_{RT} e^{-j\phi_{RT}})^{N-2}]\} \quad (2.11)$$

Recalling that, as long as the number of terms of the series in square brackets approaches infinity, the series converges to $1/(1-r'_A r'_B a_{RT} e^{-j\phi_{RT}})$, Eq. 2.11 can be rewritten as:

$$A_r = A_{in}\left[r_A + \frac{t_A t'_A r'_B a_{RT} e^{-j\phi_{RT}}}{1 - r'_A r'_B a_{RT} e^{-j\phi_{RT}}}\right] = A_{in}\frac{r_A + (t_A t'_A - r_A r'_A) r'_B a_{RT} e^{-j\phi_{RT}}}{1 - r'_A r'_B a_{RT} e^{-j\phi_{RT}}} \quad (2.12)$$

Analogously, the complex amplitudes of the transmitted waves are given by:

$$\begin{aligned} A_{1t} &= t_A t'_B \sqrt{a_{RT}} A_{in} e^{-j\phi_{RT}/2} \\ A_{2t} &= t_A t'_B r'_A r'_B \sqrt{a_{RT}} a_{RT} A_{in} e^{-j\phi_{RT}} e^{-j\phi_{RT}/2} \\ A_{3t} &= t_A t'_B r'^2_A r'^2_B \sqrt{a_{RT}} a^2_{RT} A_{in} e^{-j2\phi_{RT}} e^{-j\phi_{RT}/2} \\ &\vdots \\ A_{Nt} &= t_A t'_B (r'_A r'_B a_{RT})^{(N-1)} \sqrt{a_{RT}} A_{in} e^{-j(N-1)\phi_{RT}} e^{-j\phi_{RT}/2} \end{aligned} \quad (2.13)$$

and the sum of all the contributions gives the complex amplitude of the overall transmitted wave:

$$A_t = t_A t'_B \sqrt{a_{RT}} A_{in} e^{-j\phi_{RT}/2}[1 + (r'_A r'_B a_{RT} e^{-j\phi_{RT}}) + (r'_A r'_B a_{RT} e^{-j\phi_{RT}})^2 + \cdots \\ \cdots + (r'_A r'_B a_{RT} e^{-j\phi_{RT}})^{(N-1)}]\} \quad (2.14)$$

which can be rewritten as:

$$A_t = A_{in}\frac{t_A t'_B \sqrt{a_{RT}} e^{-j\phi_{RT}/2}}{1 - r'_A r'_B a_{RT} e^{-j\phi_{RT}}} \quad (2.15)$$

In this introductory section we will assume that both mirrors are lossless and reciprocal. Later on, in the next chapters, we will encounter other situations in which one or both of these assumptions no longer hold. For lossless mirrors made of dielectric materials, the scattering parameters are related by the Stokes relationships [77], which dictate that $r'_A = -r_A$, $r'_B = -r_B$ and $t_A t'_A - r_A r'_A = 1$. Based on these considerations and imposing the conditions in Eq. 2.5, equations 2.12 and 2.15 become:

$$A_r = A_{in}\frac{r_A - r_B a_{RT} e^{-j\phi_{RT}}}{1 - r_A r_B a_{RT} e^{-j\phi_{RT}}} \qquad A_t = A_{in}\frac{t_A t_B \sqrt{a_{RT}} e^{-j\phi_{RT}/2}}{1 - r_A r_B a_{RT} e^{-j\phi_{RT}}} \quad (2.16)$$

Assuming that A_{in}, A_r and A_t are normalized such that the corresponding optical

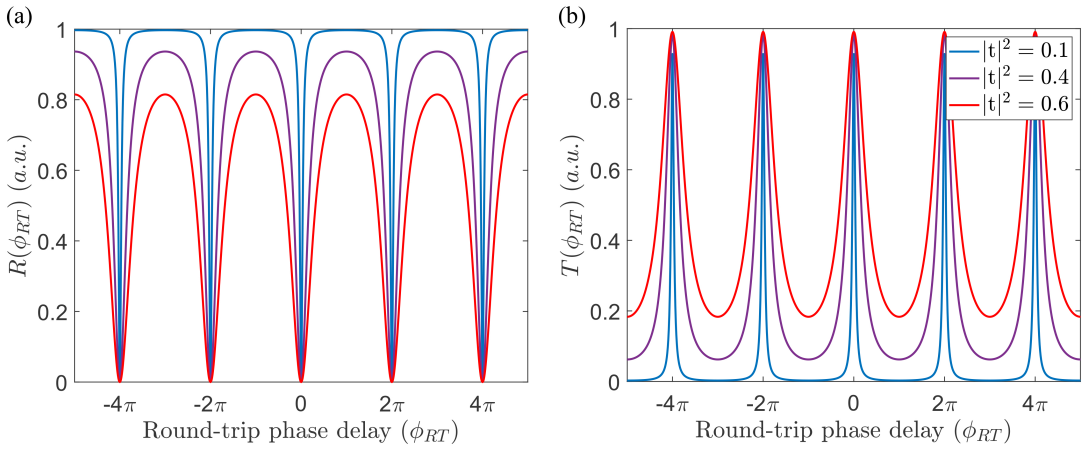

Figure 2.3 – Power spectral distribution of a symmetric Fabry-Perot resonator. (a) Reflectance and (b) transmittance as a function of the round-trip phase delay for different values of the power transmission coefficient of the two mirrors and with $a_{\mathrm{RT}} = 0.996$.

powers are given by the square modulus of their electric field amplitude, we can obtain the reflectance R and transmittance T of the FP resonator by multiplying equations 2.12 and 2.15 with their complex conjugates and dividing by the input power. After some simple algebraic passages the following expressions are obtained:

$$R = \left|\frac{A_{\mathrm{r}}}{A_{\mathrm{in}}}\right|^2 = \frac{(|\mathrm{r_A}| - |\mathrm{r_B}|a_{\mathrm{RT}})^2 + 4|\mathrm{r_A}||\mathrm{r_B}|a_{\mathrm{RT}}\sin^2\psi}{(1 - |\mathrm{r_A}||\mathrm{r_B}|a_{\mathrm{RT}})^2 + 4|\mathrm{r_A}||\mathrm{r_B}|a_{\mathrm{RT}}\sin^2\psi} \tag{2.17}$$

$$T = \left|\frac{A_{\mathrm{t}}}{A_{\mathrm{in}}}\right|^2 = \frac{(\mathrm{t_A t_B})^2 a_{\mathrm{RT}}}{(1 - |\mathrm{r_A}||\mathrm{r_B}|a_{\mathrm{RT}})^2 + 4|\mathrm{r_A}||\mathrm{r_B}|a_{\mathrm{RT}}\sin^2\psi} \tag{2.18}$$

In the above equations the phase ψ is given by:

$$2\psi = \phi_{\mathrm{RT}} + \psi_{\mathrm{r_A}} + \psi_{\mathrm{r_B}} \tag{2.19}$$

where $\psi_{\mathrm{r_A}}$ and $\psi_{\mathrm{r_B}}$ are the phase shifts experienced by the wave in reflection from the front and rear mirror respectively.

Assuming that $\psi_{\mathrm{r_A}} + \psi_{\mathrm{r_B}} = 0$, the harmonic term in equations 2.17 and 2.18 depends only on the round-trip phase delay ϕ_{RT}. In Fig. 2.3, R and T are plotted as a function of ϕ_{RT}, imposing $\psi_{\mathrm{r_A}} + \psi_{\mathrm{r_B}} = 0$. The plots are related to a symmetric FP resonator (where $\mathrm{t_A} = \mathrm{t_B} = \mathrm{t}$ and $|\mathrm{t}|^2 + |\mathrm{r}|^2 = 1$) with different values of $|\mathrm{t}|^2$ and with $a_{\mathrm{RT}} = 0.996$. We note that the spectral distribution at the transmission port takes the form of an Airy function, i.e. a series of equally-spaced transmission peaks, called *cavity resonance modes*, centered at specific values of the phase ϕ_{RT} for which $\phi_{\mathrm{RT}} = 2m\pi$, while the spectral response in reflection shows corresponding dips. This is due to the fact that the total

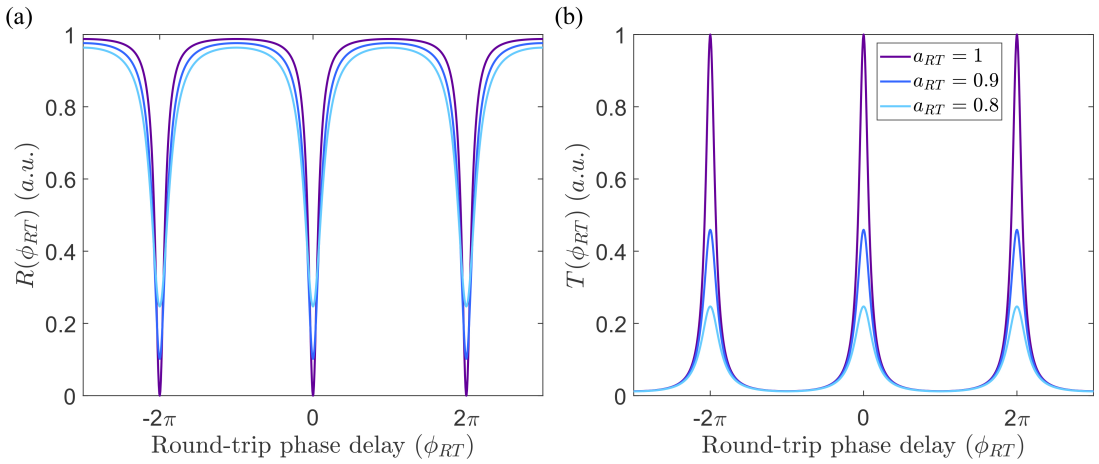

Figure 2.4 – (a) Reflectance and (b) transmittance of a symmetric Fabry-Perot resonator as a function of the round-trip phase delay for different values of the intra-cavity attenuation factor and with $|t|^2 = 0.2$.

power reflected R is the result of the superposition of the wave directly reflected by the front mirror and the portion of the wave circulating inside the cavity that is transmitted through the same mirror. Contrarily, the total transmitted power T is given by the portion of the intra-cavity power that is transmitted through the rear mirror, which is the result of the superposition between the intra-cavity circulating wave and the portion of the input wave transmitted through the front mirror. At resonance, the phases of the intra-cavity circulating wave and the incoming wave transmitted by the front mirror are such that the two waves constructively interfere and the transmittance is maximized, while in reflection, they interfere destructively. The opposite scenario occurs at anti-resonance where the transmittance is minimum because the two waves destructively interfere while the reflectance takes its maximum value. For a lossless ($a_{\mathrm{RT}} = 1$) symmetric FP resonator at resonance, the transmittance is equal to 1, meaning that the whole input power is transmitted at the output port through the resonator, while the reflectance is null given that the intra-cavity circulating wave and the portion of the input wave transmitted through the front mirror totally cancel each other. This can be seen in Fig. 2.4, where the power spectral response of a symmetric FP resonator with $|t|^2 = 0.2$ is plotted for different values of a_{RT}. It should be noted that a zero reflection can be achieved even in presence of loss if $r_A = r_B a_{\mathrm{RT}}$, a condition denoted as *critical coupling*.

The same spectral response described in equations 2.17 and 2.18 would be obtained considering an add-drop micro-ring resonator (ADMR) having the two directional couplers with cross- and straight-coupling coefficients equal to t_A, t_B and r_A, r_B, respectively. The two resonant structures can therefore be considered equivalent from the point of view of the frequency response, with the obvious difference that the transmitted wave at the through port of the ADMR is physically isolated from the input wave,

while in the FP resonator it is reflected back into the input port.

Resonant condition and free spectral range

The corresponding wavelengths for which the relation $\phi_{\mathrm{RT}} = 2m\pi$ is satisfied are called *resonance wavelengths*. They can be easily determined by considering that $\phi_{\mathrm{RT}} = n_{\mathrm{c}}(2\pi/\lambda)L_{\mathrm{RT}}$. In fact, we can write the following resonance condition:

$$2m\pi = n_{\mathrm{c}}(2\pi/\lambda)L_{\mathrm{RT}} \Rightarrow \lambda_m = \frac{n_{\mathrm{c}}}{m}L_{\mathrm{RT}} \tag{2.20}$$

or in terms of frequency:

$$\nu_m = m\frac{c}{n_{\mathrm{c}}L_{\mathrm{RT}}} \tag{2.21}$$

with m being an integer indicating the mode number and c is the speed of light in vacuum. The spacing between two consecutive resonant modes is called *free spectral range* (FSR). Its expression can be derived by computing the wavelength variation required to obtain a round-trip phase change equal to 2π. This can be done by taking the derivative of the round-trip phase delay with respect to the wavelength, which is:

$$\frac{d\phi_{\mathrm{RT}}}{d\lambda} = \left(\frac{dn_{\mathrm{c}}}{d\lambda} - \frac{n_{\mathrm{c}}}{\lambda}\right)\frac{2\pi}{\lambda}L_{\mathrm{RT}} = \frac{d\phi_{\mathrm{RT}}}{d\lambda} = -n_{\mathrm{g}}\frac{2\pi}{\lambda^2}L_{\mathrm{RT}} \tag{2.22}$$

where $n_{\mathrm{g}} = n_{\mathrm{c}} - \lambda(dn_{\mathrm{c}}/d\lambda)$ is the group index of the intra-cavity medium. Imposing the condition $\Delta\phi_{\mathrm{RT}} = 2\pi$ we finally get the expression of the FSR:

$$\Delta\lambda_{\mathrm{FSR}} = \frac{2\pi}{d\phi_{\mathrm{RT}}/d\lambda} = -\frac{\lambda^2}{n_{\mathrm{g}}L_{\mathrm{RT}}} \tag{2.23}$$

which in terms of frequency becomes:

$$\Delta\nu_{\mathrm{FSR}} = -\frac{c}{\lambda^2}\Delta\lambda_{\mathrm{FSR}} = \frac{c}{n_{\mathrm{g}}L_{\mathrm{RT}}} = \frac{1}{T_{\mathrm{RT}}} \tag{2.24}$$

Where T_{RT} is the cavity round-trip time, i.e. the time the wave takes to travel the whole cavity length L_{RT}. It should be noted that, in general, the intra-cavity medium exhibits frequency dispersion. In such a case, the FSR will be frequency-dependent resulting in a corresponding shift of resonance frequencies.

2.1.3 Intra-cavity field and power enhancement

Using the circulating field approach, as we did for the derivation of equations 2.12 and 2.15, we can also find the complex amplitude of the total electric field circulating inside the cavity. It is simply given by the interference between the wave circulating

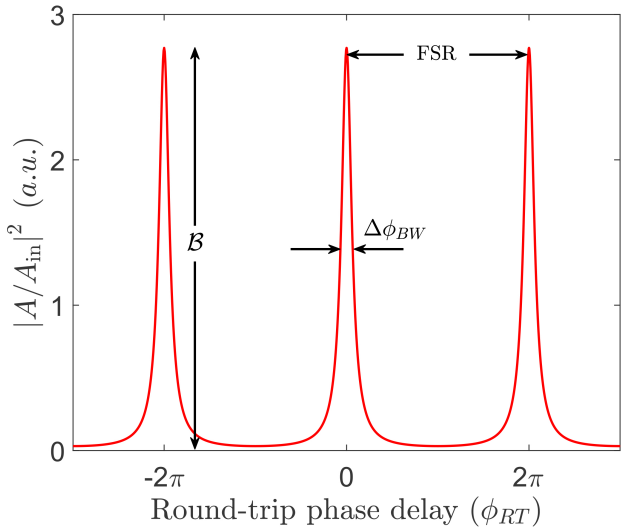

Figure 2.5 – Intra-cavity power enhancement of a symmetric Fabry-Perot resonator as a function of the round-trip phase delay with $|\mathrm{t}|^2 = 0.1$ and $a_{\mathrm{RT}} = 0.9$.

within the cavity after the first round-trip and the new incoming wave transmitted from the front mirror:

$$A = \mathrm{t_A} A_{\mathrm{in}} + \mathrm{r_A r_B} a_{\mathrm{RT}} e^{-j\phi_{\mathrm{RT}}} A \Rightarrow A = A_{\mathrm{in}} \frac{\mathrm{t_A}}{1 - \mathrm{r_A r_B} a_{\mathrm{RT}} e^{-j\phi_{\mathrm{RT}}}} \tag{2.25}$$

The corresponding intra-cavity power is then:

$$|A|^2 = |A_{\mathrm{in}}|^2 \frac{|\mathrm{t_A}|^2}{1 + |\mathrm{r_A}|^2 |\mathrm{r_B}|^2 a_{\mathrm{RT}}^2 - 2|\mathrm{r_A}||\mathrm{r_B}| a_{\mathrm{RT}} \cos 2\psi} \tag{2.26}$$

where the phase ψ is given by Eq. 2.19. Dividing Eq. 2.26 for the total input power, the intra-cavity power enhancement is obtained:

$$\left| \frac{A}{A_{\mathrm{in}}} \right|^2 = \frac{|\mathrm{t_A}|^2}{1 + |\mathrm{r_A}|^2 |\mathrm{r_B}|^2 a_{\mathrm{RT}}^2 - 2|\mathrm{r_A}||\mathrm{r_B}| a_{\mathrm{RT}} \cos 2\psi} \tag{2.27}$$

which, at resonance, gives the *intra-cavity power enhancement factor* or *build-up factor* of the resonator:

$$\mathcal{B} = \left| \frac{A}{A_{\mathrm{in}}} \right|^2_{\psi = m\pi} = \frac{|\mathrm{t_A}|^2}{(1 - |\mathrm{r_A}||\mathrm{r_B}| a_{\mathrm{RT}})^2} \tag{2.28}$$

The corresponding plot of Eq. 2.27 as a function of ϕ_{RT} and for $|\mathrm{t_A}|^2 = |\mathrm{t_B}|^2 = |\mathrm{t}|^2 = 0.1$ and $a_{\mathrm{RT}} = 0.9$, is shown in Fig. 2.5. We note that the intra-cavity power enhancement exhibits the same spectral distribution as the transmitted power, with equally-spaced resonance peaks centered at $\psi = m\pi$. Eq. 2.28 is a measure of the build-up of optical

power within the cavity due to the constructive interference at resonance between the intra-cavity circulating wave and the input wave at the front mirror. To give an idea of how much this factor is impactful, we can note that, in a symmetric resonator with small internal loss ($a_{\mathrm{RT}} \approx 1$), $\mathcal{B}$ is inversely proportional to the transmissivity of the mirrors, i.e. $\mathcal{B} \approx 1/|\mathrm{t}|^2$. For cavities with highly reflective mirrors ($|\mathrm{t}|^2 \approx 0.1\text{–}0.01$) this leads to an intra-cavity power amplified by $1\text{–}2$ orders of magnitude. This intrinsic feature, characteristic of every resonant system, is widely used in many applications and specially in nonlinear optics, where the build-up factor significantly contributes to reducing the threshold power for triggering the nonlinear effects.

Spectral bandwidth and cavity finesse

To derive an expression of the bandwidth of the resonance modes we can start rewriting Eq. 2.27 as following:

$$\left|\frac{A}{A_{\mathrm{in}}}\right|^2 = \frac{|\mathrm{t_A}|^2}{(1-|\mathrm{r_A}||\mathrm{r_B}|a_{\mathrm{RT}})^2 + 4|\mathrm{r_A}||\mathrm{r_B}|a_{\mathrm{RT}}\sin^2\psi} \tag{2.29}$$

By substituting Eq. 2.28 into Eq. 2.29 we obtain:

$$\left|\frac{A}{A_{\mathrm{in}}}\right|^2 = \frac{\mathcal{B}}{1+F\sin^2\psi} \tag{2.30}$$

where F is given by the following expression:

$$F = \frac{4|\mathrm{r_A}||\mathrm{r_B}|a_{\mathrm{RT}}}{(1-|\mathrm{r_A}||\mathrm{r_B}|a_{\mathrm{RT}})^2} \tag{2.31}$$

F is called the contrast of the resonator since it represents a measure of the sharpness of the resonance peak. Since the bandwidth of the resonator is defined as the full width at half maximum (FWHM) of the cavity resonance mode we have to find the specific value of the phase difference $\Delta\psi_{\mathrm{3dB}}$ for which Eq. 2.30 drops to half of its maximum value, i.e. $\mathcal{B}/2$:

$$\left|\frac{A}{A_{\mathrm{in}}}\right|^2_{\Delta\psi_{\mathrm{3dB}}} = \frac{\mathcal{B}}{1+F\sin^2\Delta\psi_{\mathrm{3dB}}} = \frac{\mathcal{B}}{2} \tag{2.32}$$

Imposing again the condition $\psi_{\mathrm{r_A}} + \psi_{\mathrm{r_B}} = 0$ on Eq. 2.19 we obtain:

$$\Delta\phi_{\mathrm{RT}}\Big|_{\mathrm{3dB}} = 2\arcsin\frac{1}{\sqrt{F}} \tag{2.33}$$

and therefore the bandwidth of the resonance mode is:

$$\Delta\phi_{\mathrm{BW}} = 4\arcsin\frac{1}{\sqrt{F}} \tag{2.34}$$

For resonators with highly reflective mirrors and small intra-cavity absorption loss, the small-angle approximation can be applied to Eq. 2.34, which therefore becomes:

$$\Delta\phi_{\mathrm{BW}} \approx 4\frac{1}{\sqrt{F}} = \frac{2(1-|\mathrm{r_A}||\mathrm{r_B}|a_{\mathrm{RT}})}{\sqrt{|\mathrm{r_A}||\mathrm{r_B}|a_{\mathrm{RT}}}} \tag{2.35}$$

The corresponding formula in terms of angular frequency ω can be obtained by taking the derivative of ϕ_{RT} with respect to ω:

$$\frac{d\phi_{\mathrm{RT}}}{d\omega} = \left(\frac{n_{\mathrm{c}}}{c} + \frac{\omega}{c}\frac{dn_{\mathrm{c}}}{d\omega}\right) L_{\mathrm{RT}} = \left(n_{\mathrm{c}} + \omega\frac{dn_{\mathrm{c}}}{d\omega}\right)\frac{L_{\mathrm{RT}}}{c} = \frac{cL_{\mathrm{RT}}}{n_{\mathrm{g}}} = T_{\mathrm{RT}} \tag{2.36}$$

where $n_{\mathrm{g}} = n_{\mathrm{c}} + \omega(dn_{\mathrm{c}}/d\omega)$ is the group index of the intra-cavity medium. Equation 2.36 tells us that the bandwidth in terms of phase is related to a corresponding frequency bandwidth by $\Delta\phi_{\mathrm{BW}} = \Delta\omega_{\mathrm{BW}}T_{\mathrm{RT}}$. It follows that we can write the bandwidth of the resonance mode in terms of angular frequency as:

$$\Delta\omega_{\mathrm{BW}} = \frac{\Delta\phi_{\mathrm{BW}}}{T_{\mathrm{RT}}} = \frac{n_{\mathrm{g}}}{cL_{\mathrm{RT}}}\frac{2(1-|\mathrm{r_A}||\mathrm{r_B}|a_{\mathrm{RT}})}{\sqrt{|\mathrm{r_A}||\mathrm{r_B}|a_{\mathrm{RT}}}} \tag{2.37}$$

Another important parameter that contributes to characterize the spectral response and the intra-cavity power enhancement of a resonator is the *cavity finesse* $\mathcal{F}$ which is defined as the ratio of the FSR with the resonance mode bandwidth:

$$\mathcal{F} = \frac{\Delta\omega_{\mathrm{FSR}}}{\Delta\omega_{\mathrm{BW}}} = \frac{\pi}{2}\sqrt{F} = \frac{\pi\sqrt{|\mathrm{r_A}||\mathrm{r_B}|a_{\mathrm{RT}}}}{1-|\mathrm{r_A}||\mathrm{r_B}|a_{\mathrm{RT}}} \tag{2.38}$$

The cavity finesse can be related to the build-up factor simply by considering that for low loss and symmetric resonators with highly reflective mirrors the above expression simplifies to $\mathcal{F} \approx \pi/|\mathrm{t}|^2$. Therefore, recalling that in this scenario $\mathcal{B} \approx 1/|\mathrm{t}|^2$, the cavity finesse can be written as:

$$\mathcal{F} = \pi\mathcal{B} \tag{2.39}$$

2.2 Temporal coupled-mode theory for optical resonators - Energy coupling formalism

Temporal coupled-mode theory (TCMT) is a powerful theoretical framework used to describe the coupling of energy between a resonant system and an external waveguide, where the former is identified by *localized modes*, while the latter by *propagating modes*. It relies on an abstract formulation of few parameters characteristic of the resonant system, such as the resonance frequency and the energy coupling coefficients, which depend on the specific geometry of the cavity. The TCMT is widely used to describe the behavior of resonant structures of different kinds ranging from ordinary

resonant cavities, such as Fabry-Perot or ring resonators, to photonic crystal cavities or even atomic oscillators. As we already mentioned at the beginning of the previous section, the TCMT describes the behavior of the device from the point of view of energy exchange between the resonator and the external waveguide. Unlike the power coupling formalism, which is more rigorous since no assumption is made about the coupling strengths, the TCMT is valid only under the assumption of weak coupling, so that the spatial distribution of the energy within the cavity can be considered uniform.

2.2.1 Temporal coupled-mode equations

We will now review the basic principles of TCMT by considering the simple resonant structure schematically illustrated in Fig. 2.6. The cavity has a resonance frequency ω_0 and is connected to the outside world through two single-mode waveguides with coupling coefficients κ_1 and κ_2 respectively. For the sake of simplicity, let us first consider the cavity without any input signals but which is already charged with an initial energy $|a(0)|^2$.

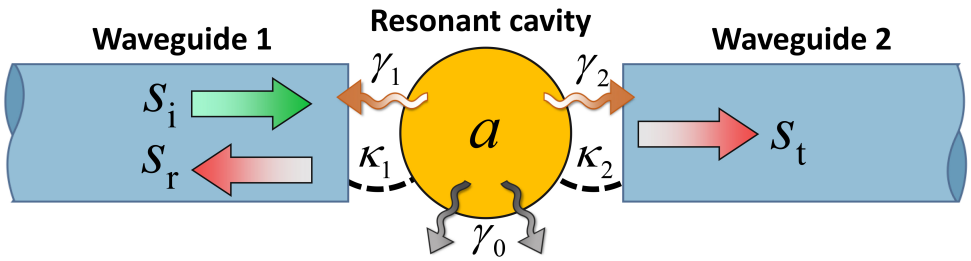

Figure 2.6 – Illustrative drawing of a resonant structure coupled to two external waveguides through the coupling coefficients κ_1 and κ_2 and characterized by a resonance frequency ω_0.

The evolution of the amplitude a of the optical field inside the resonator can be described using the well known equation of motion [71, 78, 79]:

$$\frac{da}{dt} = (j\omega_0 - \gamma_0 - \gamma_1 - \gamma_2)a \tag{2.40}$$

where γ_1, γ_2 and γ_0 are the decay rates of the intra-cavity field amplitude owing to the coupling with the two waveguides and the intra-cavity absorption loss, respectively. More generally, we can classify the losses of a resonator in two categories: (i) *radiative losses*, which are caused by a loss of energy due to coupling to external waveguides, and (ii) *non-radiative* or *dissipative losses*, that take into account the absorption and scattering occurring in the intra-cavity medium or losses due to imperfection of the coupling junctions. In the case we are investigating, γ_1 and γ_2 are the radiative losses, while γ_0 represents the non-radiative component of the losses of the system. Moreover,

in Eq. 2.40, we assume that a is normalized such that $|a(t)|^2$ gives the electromagnetic energy stored within the cavity at time t. The above equation is a simple first order differential equation that can be easily solved obtaining the amplitude of the intra-cavity field as a function of time:

$$a(t) = a(0)e^{-\gamma t}e^{j\omega_0 t} \tag{2.41}$$

where $\gamma = \gamma_0 + \gamma_1 + \gamma_2$ is the total amplitude decay rate. The expression of the time-evolution of the energy stored within the cavity is then given by:

$$|a(t)|^2 = |a(0)|^2 e^{-2\gamma t} = |a(0)|^2 e^{-t/\tau} \tag{2.42}$$

where $\tau = 1/2\gamma$ is the *energy cavity lifetime*, i.e. the time after which the energy stored in the cavity drops to 1/e of its initial value $a(0)$. We can note, in fact, that the energy stored in an isolated resonator decays exponentially with time at a rate that depends on the strength of the coupling with the external waveguides and the intra-cavity absorption loss (since $\gamma = \gamma_0 + \gamma_1 + \gamma_2$).

Let us now suppose that an input wave s_i, coming from waveguide 1, is incident on the cavity. If we denote the rate of in-coupling energy from waveguide 1 with ρ_in, we have that the input wave s_i supplies energy to the cavity at a rate given by $\sqrt{\rho_\mathrm{in}}s_\mathrm{i}$. In this case, the equation of motion becomes:

$$\frac{da}{dt} = (j\omega_0 - \gamma_0 - \gamma_1 - \gamma_2)a + \sqrt{\rho_\mathrm{in}}s_\mathrm{i} \tag{2.43}$$

where s_i is normalized such that $|s_\mathrm{i}|^2$ is the power flowing in the input waveguide (waveguide 1). The solution of the above equation can be found by assuming that both s_i and $a(t)$ have the same harmonic time dependence ($s_\mathrm{i}, a(t) \propto e^{j\omega t}$). Therefore we can write:

$$j\omega a = (j\omega_0 - \gamma)a + \sqrt{\rho_\mathrm{in}}s_\mathrm{i} \tag{2.44}$$

By isolating a, we obtain:

$$a(\omega) = \frac{\sqrt{\rho_\mathrm{in}}s_\mathrm{i}}{j(\omega - \omega_0) + \gamma} \tag{2.45}$$

This expression gives the amplitude of the intra-cavity field as a function of the frequency. The expression of the energy stored within the cavity is therefore:

$$|a(\omega)|^2 = \frac{\rho_\mathrm{in}|s_\mathrm{i}|^2}{(\omega - \omega_0)^2 + \gamma^2} \tag{2.46}$$

Once we have obtained the frequency distribution of the intra-cavity field, we can derive the spectral response in transmission and reflection of any weakly-coupled

resonant system. The formula of the transmitted field s_t can be found by noting that the signal exiting the cavity from port 2 is simply $s_t = \sqrt{\rho_{out,2}}a$, where $\rho_{out,2}$ is the rate of out-coupling energy from waveguide 2. Then, substituting Eq. 2.45 we have:

$$\frac{s_t}{s_i} = \frac{\sqrt{\rho_{in}}\sqrt{\rho_{out,2}}}{j(\omega-\omega_0)+\gamma} \tag{2.47}$$

The signal s_r reflected by the resonator is the sum of two contributions: (i) the portion of the incident signal directly reflected by the cavity at port 1 and (ii) the portion of intra-cavity field lost through port 1. In mathematical terms:

$$s_r = c_s s_i + \sqrt{\rho_{out,1}}a \tag{2.48}$$

where c_s is a scattering coefficient that describes the behavior of the system in absence of resonance, while $\rho_{out,1}$ is the rate of out-coupling energy from waveguide 1. Substituting Eq. 2.45 we obtain:

$$s_r = c_s s_i + \frac{\sqrt{\rho_{in}}\sqrt{\rho_{out,1}}}{j(\omega-\omega_0)+\gamma}s_i \Rightarrow \frac{s_r}{s_i} = \frac{jc_s(\omega-\omega_0)+c_s\gamma+\sqrt{\rho_{in}}\sqrt{\rho_{out,1}}}{j(\omega-\omega_0)+\gamma} \tag{2.49}$$

Equations 2.47 and 2.49 represent the transfer functions of the resonant system in transmission and reflection respectively. The corresponding power spectral responses $T(\omega)$ and $R(\omega)$ are given by the following expressions:

$$T(\omega) = \left|\frac{s_t}{s_i}\right|^2 = \frac{\rho_{in}\rho_{out,2}}{(\omega-\omega_0)^2+\gamma^2} \tag{2.50}$$

$$R(\omega) = \left|\frac{s_r}{s_i}\right|^2 = \frac{c_s^2(\omega-\omega_0)^2+(c_s\gamma+\sqrt{\rho_{in}}\sqrt{\rho_{out,1}})^2}{(\omega-\omega_0)^2+\gamma^2} \tag{2.51}$$

Linewidth of the resonance mode and time-bandwidth limit

We note that both, the intra-cavity energy and the transmitted power have a spectral distribution that takes the form of a Lorentzian function centered around the resonance frequency ω_0. To find a mathematical expression of the linewidth of this Lorentzian function, we can equate Eq. 2.50 to half of its peak value, which occurs at $\omega = \omega_0$, thus obtaining:

$$\frac{\rho_{in}\rho_{out,2}}{(\Delta\omega_{3dB})^2+\gamma^2} = \frac{\rho_{in}\rho_{out,2}}{2\gamma^2} \Rightarrow \Delta\omega_{3dB} = \gamma \tag{2.52}$$

Finally we find that the bandwidth of the Lorentzian resonant mode is:

$$\Delta\omega_{BW} = 2\gamma = \frac{1}{\tau} \tag{2.53}$$

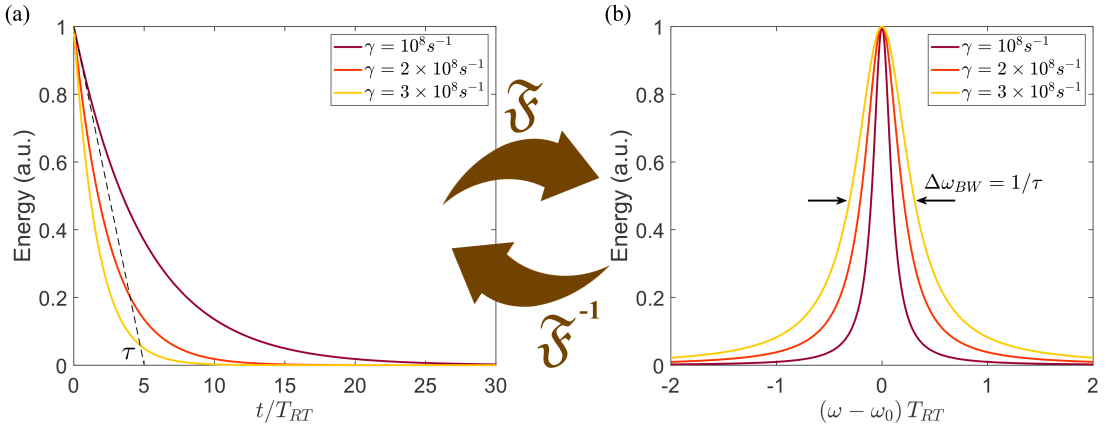

Figure 2.7 – Fourier transform relationship between (a) the exponentially decaying evolution of the energy stored inside a resonant system and (b) its corresponding Lorentzian-shaped power spectrum. The graphs, plotted for different values of γ are related to a resonant cavity with $\rho_{\text{in}} = \rho_{\text{out},2} = 10^8 s^{-1}$ and with a cavity round-trip time T_{RT} of 1 ns.

From this expression we note that the bandwidth of the resonant mode of any resonant system is strictly correlated to the losses of the system. This is graphically shown in Fig. 2.7b, where the Lorentzian resonance mode for a resonant cavity with $\rho_{\text{in}} = \rho_{\text{out},2} = 10^8 s^{-1}$ and $T_{\text{RT}} = 1$ ns, is plotted for different values of the total decay rate γ. It is clear from the graph that the bandwidth of the mode gets wider with increasing γ.

Rewriting Eq. 2.53 as:

$$\Delta\omega_{\text{BW}} \cdot \tau = 1 \tag{2.54}$$

it takes the form of a mathematical tenet known as *time-bandwidth limit* (TBL), which is the result of the Fourier transform relationship between the exponential decay of the energy stored inside the resonant system and its corresponding Lorentzian-shaped power spectrum. In fact, we could achieve the same result for the bandwidth by using Eq. 2.46, which is nothing else but the Fourier transform of Eq. 2.42. The Fourier relationship between the resonance mode of a resonant cavity and its corresponding energy decay curve, is illustrated in Fig. 2.7 through a plot of Eq. 2.42 and 2.46 for different values of γ and with $\rho_{\text{in}} = \rho_{\text{out},2} = 10^8 s^{-1}$ and $T_{\text{RT}} = 1$ ns.

The TBL simply dictates that the product between the bandwidth of a resonant mode and the corresponding decay time, i.e. the time-bandwidth product (TBP), must be equal to 1. What this simple rule means is that a larger bandwidth of the resonance mode, which can be obtained with a stronger coupling, is always correlated to a reduced cavity photon life-time, therefore limiting the interaction time between the light and the intra-cavity medium or simply the storage time of the resonant system. A

recent theoretical study [49] suggesting that the TBL can be overcome by breaking the reciprocity of the system (whose implications will be explained in the next section), opened an interesting debate [52–55] about whether or not this can be possible in linear and time-invariant resonant systems. Furthermore, the TBL finds its confirmation in the TCMT framework, which is not straightforwardly applicable to open resonant systems. In fact, although at the first glance it looks that this fundamental rule cannot be violated, its foundation relies on the assumptions of linearity and time-invariance of resonant systems whose energy exchange with the outside world concerns only the single-mode resonance. Therefore the validity of the TBL is to be considered limited to resonant systems that fulfill these conditions. In the above treatment we used the TCMT to model a resonant cavity coupled to two external waveguides. Doing so, we implicitly took for granted the linearity and time-invariance assumptions, given that no nonlinear terms have been included in the equation of motion and all energy coupling coefficients and decay rates are assumed to be independent on the time parameter. We will see in the next chapters that by breaking the time-invariance property of a resonant system and inducing a nonreciprocal coupling results in a decoupling of the bandwidth that the system can accept from the cavity life-time, thus leading to an overall TBP much greater than 1.

Quality factor

An important parameter that is used to give a measure of the sharpness of the resonance mode with respect to its central frequency is the quality factor (Q-factor). It is defined as:

$$Q = 2\pi \frac{Averaged\ stored\ energy}{Power\ loss \times Optical\ period} \tag{2.55}$$

Considering that the intra-cavity field has an harmonic dependence with time, the stored energy at time t is given by:

$$W(t) = W_0 \cos^2(\omega t) e^{-2\gamma t} \tag{2.56}$$

where W_0 is the initial stored energy. Assuming that the rate of energy decay is much smaller than the angular frequency of the optical field ($2\gamma \ll \omega$), we have that the time-averaged energy stored in the resonator over one optical cycle is:

$$\langle W(t) \rangle = \frac{1}{2} W_0 e^{-2\gamma t} \tag{2.57}$$

while the power loss is nothing else but the rate of change of the energy:

$$-\frac{d\langle W(t) \rangle}{dt} = 2\gamma \langle W(t) \rangle \tag{2.58}$$

Substituting equations 2.57 and 2.58 into 2.55 we finally get the expression of the Q-factor as the ratio of the angular frequency to the cavity bandwidth:

$$Q = 2\pi \frac{\langle W(t) \rangle}{-\frac{d\langle W(t) \rangle}{dt} T} = \frac{\omega}{2\gamma} = \frac{\omega}{\Delta\omega_{\text{BW}}} \tag{2.59}$$

Energy coupling coefficients

From Eq. 2.42 we can derive a relationship between the energy coupling rate coefficients $\rho_{\text{out,1}}, \rho_{\text{out,2}}$ and the decay rates γ_1, γ_2. We first assume that the cavity, charged with an initial energy $|a(0)|^2$, exhibits no dissipative loss ($\gamma_0 = 0$) and is coupled only to waveguide 2. By taking the derivative of Eq. 2.42, we obtain the rate of change of energy stored in the resonator:

$$\frac{d|a(t)|^2}{dt} = -2\gamma_2 |a(t)|^2 \tag{2.60}$$

Then, recalling that the signal exiting the cavity from port 2 is expressed by $s_{\text{t}} = \sqrt{\rho_{\text{out,2}}} a$, the corresponding power leaving the cavity is $|s_{\text{t}}|^2 = \rho_{\text{out,2}} |a(t)|^2$. Based on these considerations we can deduce the following:

$$\rho_{\text{out,2}} = 2\gamma_2 \tag{2.61}$$

Following an identical procedure we can find the same relation between $\rho_{\text{out,1}}$ and γ_1. Also, by denoting with ρ_0 the rate of energy dissipated within the cavity due to non-radiative losses and assuming the cavity perfectly isolated from the external waveguides, a similar relation exists for ρ_0 and γ_0.

2.2.2 Time-reversal symmetry and conservation of energy

Most of the scientific material found in literature that uses the TCMT for the modeling of resonant structures, usually assumes the simultaneous presence of three main constraints: time-reversal symmetry, Lorentz reciprocity and energy conservation. Applying these constraints, the TCMT equations take a simpler form, as we will discover soon. However, there are several optical systems that do not fulfill all these three conditions and, therefore, need to be treated using the more generic TCMT equations that we have previously obtained. Within the framework of the TCMT these three constraints act mainly on the in-coupling and out-coupling energy rates, and the scattering coefficient of the system in absence of resonance.

Time-reversal symmetry and Lorentz reciprocity

For the resonant system depicted in Fig. 2.6, the time-reversal symmetry and Lorentz reciprocity are strictly correlated to each other since the breaking of the time-reversal symmetry of the system requires a nonreciprocity of the coupling junctions. In fact the time reversal operation consists of assuming the set of mathematical functions that describe the system as running backwards in time [80]. In mathematical terms, this results in changing the sign of the time parameter in Eq. 2.42 obtaining that the stored energy builds up in the cavity, instead of decaying, since its evolution in time is described by an exponentially growing function:

$$|a(t)|^2 = |a(0)|^2 e^{2\gamma t} \tag{2.62}$$

However, during the *loading* process, i.e. the time-reversed version of the decay process, the energy is being transfer from outside towards inside the cavity at a rate $+2\gamma$ that now takes the role of an energy *loading* rate ρ_{L}.

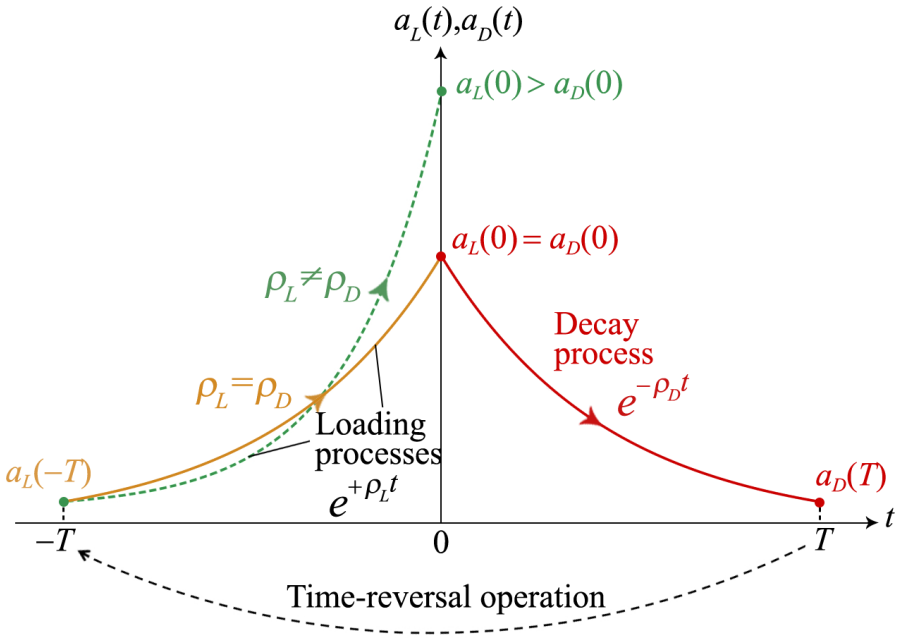

Figure 2.8 – Illustration representing the time-reversal operation applied to the time evolution of the energy stored in a resonant system in case of reciprocal and nonreciprocal coupling. The orange and the dashed-green curves represent the loading processes in case of a time-reversal symmetric and asymmetric system respectively, while the red curve represents the decay process.

Now, assuming for simplicity that the cavity is connected only to waveguide 2, if the coupling junction at port 2 is characterized by a symmetric scattering matrix ($\mathbf{S} = \mathbf{S}^T$) the loading and decay energy rate coefficients are identical $\rho_{\mathrm{L}} = \rho_{\mathrm{D}}$ and the resonant system is said time-reversal symmetric. Conversely if the coupling element is

a nonreciprocal optical component, $\rho_{\mathrm{L}} \neq \rho_{\mathrm{D}}$, meaning that the system changes during the time-reversal operation and therefore, the time-reversal symmetry property no longer holds [50].

This concept is schematically illustrated in Fig. 2.8, where the evolution of the energy stored inside the resonant system is illustrated for both scenarios. In particular, the intra-cavity energy is monitored from its initial value until time $t = T$. Then, under time-reversal operation, the sign of the time variable is flipped and the system evolves from $t = -T$ until $t = 0$. We note that $\rho_{\mathrm{L}} = \rho_{\mathrm{D}}$ implies that the decay and loading curves (red and orange curves) are identical, meaning that the system remains the same after the time-reversal operation and, therefore it is said time-reversal symmetric. Conversely, if $\rho_{\mathrm{L}} \neq \rho_{\mathrm{D}}$, the time-reverse (loading) process (green-dashed curve) is different (i.e. the time-reversal symmetry is broken) and leads the intra-cavity energy to reach a value at $t = 0$ that does not match its initial value, a condition that is not physically admittable. In such a case the system is said time-reversal asymmetric. I want to stress here that the nonreciprocity condition on the coupling element requires the infringement of one of the two assumptions: the linearity or the time-invariance of the system. As we will see in Chapter 3, this is an important concept that must be taken into account when designing the coupling element. Also, it should be noted that the loading process does not represent how the energy of the input wave is effectively coupled into the cavity. The evolution in time of the energy coupling within the cavity is related to the time dependence of the input signal. Nevertheless, the exponentially growing time evolution is proved to be the optimum coupling of any linear resonant system [81, 82].

Conservation of energy

The condition of the conservation of energy is useful to derive an expression for the scattering coefficient c_{s} in Eq. 2.48. In fact, if we consider the net power flowing into the resonator, $|s_{\mathrm{i}}|^2 - |s_{\mathrm{out}}|^2$, this is given by the sum of the total energy build up in the cavity with the total power dissipated through non-radiative loss:

$$|s_{\mathrm{i}}|^2 - |s_{\mathrm{out}}|^2 = \frac{d|a|^2}{dt} + \rho_0 |a|^2 \tag{2.63}$$

where $s_{\mathrm{out}} = s_{\mathrm{r}} + s_{\mathrm{t}} = c_{\mathrm{s}} s_{\mathrm{i}} + \sqrt{\rho_{\mathrm{out}}} a$ and $\sqrt{\rho_{\mathrm{out}}} = \sqrt{\rho_{\mathrm{out,1}}} + \sqrt{\rho_{\mathrm{out,2}}}$. The total energy build up in the cavity can be calculated from Eq.2.43 as following [79]:

$$\frac{d|a|^2}{dt} = -(\rho_0 + \rho_{\mathrm{out}})|a|^2 + \sqrt{\rho_{\mathrm{in}}}(a^* s_{\mathrm{i}} + a s_{\mathrm{i}}^*) \tag{2.64}$$

where the asterisk indicates the complex conjugate, while from Eq. 2.48 we get the total power leaving the cavity is:

$$|s_{\text{out}}|^2 = c_{\text{s}}^2|s_{\text{i}}|^2 + \rho_{\text{out}}|a|^2 + 2\,\text{Re}\,[c_{\text{s}}s_{\text{i}}\rho_{\text{out}}a^*] \tag{2.65}$$

Substituting Eq. 2.64 and 2.65 into 2.63 and recalling that $a, s_{\text{i}} \propto e^{j\omega t}$ we obtain:

$$c_{\text{s}} = -1 \tag{2.66}$$

and thus $s_{\text{out}} = -s_{\text{i}}$. The physical meaning of this result can be understood by considering that in absence of resonance $a = 0$, therefore no energy is present inside the cavity. As a result, the incoming power must be fully reflected back by the resonator.

2.3 Characteristics of fiber lasers

In this last section we examine the fundamental concepts of fiber lasers that will be useful for a complete understanding of the operating principles of the figure-9 laser described in the next chapter.

The laser is fundamentally different from the other conventional light sources since it is based on the stimulated emission rather than spontaneous emission. The fundamental ingredient of the laser is the optical amplifier, an optical device capable of amplifying an optical signal. However, to make a laser, an internal intensity and wavelength selection mechanism is also needed, known as *positive feedback*. Owing to this mechanism the optical amplifier turns into an optical oscillator, i.e. a resonant system that provides an optical signal characterized by a high level of monochromaticity, brightness and directionality that distinguish it from the other ordinary light sources.

2.3.1 Basic scheme of an optical oscillator

The laser can be considered as the analogous of the electronic oscillator extended at the optical frequencies. A simple scheme of an oscillator includes an amplifier inserted in a positive feedback loop as illustrated in Fig. 2.9a. The signals S_{in} and S_{out} represent, in the case of optical oscillator, the input and output electric fields respectively. The input signal, while propagating through the gain medium, is amplified by a factor G. At the output of the amplifier a portion β of the amplified signal is transferred back to the input port of the system and added to the input signal. The output signal S_{out} is thus given by the sum of the infinite feedback contributions:

$$S_{\text{out}} = GS_{\text{in}} + \beta G^2 S_{\text{in}} + \beta^2 G^3 S_{\text{in}} + \cdots = GS_{\text{in}}(1 + \beta G + \beta^2 G^2 + \cdots) \tag{2.67}$$

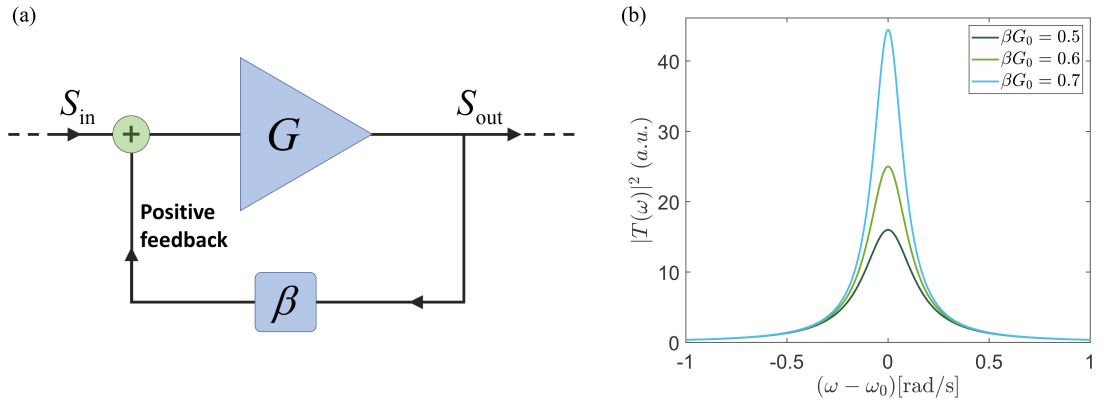

Figure 2.9 – (a) Basic layout of an oscillator consisting of an amplifier with a positive feedback and (b) its corresponding power transfer function plotted for different values of the loop gain βG_0 imposing $G_0 = 2$ and $\tau = 3$ ns.

where G and β are in general complex function of the angular frequency ω. Assuming that $|\beta G| < 1$, the geometrical series in Eq. 2.67 converges to $1/(1-\beta G)$. Therefore we obtain:

$$S_{\text{out}} = S_{\text{in}} \frac{G}{1-\beta G} \tag{2.68}$$

In this expression the term βG is called loop gain. The transfer function T of the oscillator is easily obtained:

$$T = \frac{S_{\text{out}}}{S_{\text{in}}} = \frac{G}{1-\beta G} \tag{2.69}$$

Now let us suppose that the gain medium exhibits a power spectral distribution of a Lorentzian shape, as it occurs in most practical cases, while β does not depend on ω. Then, the expression of G as a function of ω is given by:

$$G(\omega) = \frac{G_0}{1 + j(\omega - \omega_0)\tau} \tag{2.70}$$

and the power spectral response:

$$|G(\omega)|^2 = \frac{|G_0|^2}{1 + (\omega - \omega_0)^2 \tau^2} \tag{2.71}$$

where G_0 is the peak value of the gain, while τ^{-1} is the FWHM of the Lorentzian function. By substituting Eq. 2.70 into 2.69 we obtain the spectral response of the oscillator:

$$T(\omega) = \frac{G_0}{1 - \beta G_0 + j(\omega - \omega_0)\tau} = \frac{G_f}{1 + j(\omega - \omega_0)\tau_f} \tag{2.72}$$

where $G_f = G_0/(1-\beta G_0)$ and $\tau_f = \tau/(1-\beta G_0)$. From the above expression we note that the effect of the positive feedback is duplex: (i) on the one hand it increases the peak value of the gain, while (ii) on the other hand the bandwidth of the gain is proportionally reduced. Particularly, this twofold effect is a result of the gain-bandwidth product for which an increase of the amplifier gain for a certain frequency range follows a bandwidth narrowing in the same frequency range [83]. In Fig. 2.9b a plot of $|T(\omega)|^2$ is shown for different values of the loop gain in the range $0 < \beta G_0 < 1$. The condition $\beta G_0 = 1$, where G_f becomes infinite, is called threshold condition for the system to work as oscillator. At this value of the loop gain the system gives a finite output signal for an infinitely small input signal. After a first inspection of Eq. 2.72, it looks that for values above the threshold condition, the output signal can take an infinite value. However, this is not the case simply for considerations on the energy conservation, which dictates that the energy provided by the oscillator must be equal to the energy provided by the pumping mechanism acting on the gain medium. What ensures the conservation of energy is the gain saturation. Specifically, when the system goes above the threshold, the output power start decreasing until it reaches the saturation value S_s, pulling the loop gain down to the threshold value.

2.3.2 Optical amplification

Without entering into the details of the quantum mechanical treatment of the light-matter interaction, we will now briefly review the main conditions for optical amplification.
The operation of a laser require that energy provided by a pump source is stored in the atoms of the gain medium. This occurs through a transfer of the electrons from a lower to a higher energy level, which are identified as ground state and excited state respectively. An electromagnetic wave, incident on the gain medium, can be amplified only in case of *population inversion*, i.e. if the number of atoms N_2 in the excited state is larger than the number of atoms N_1 in the ground state. In fact, thanks to the stimulated emission process, the energy stored in the atoms is released through the interaction with the electromagnetic wave and it is transferred to its radiation field. In addition the frequency of the wave must be equal to that corresponding to the energy levels difference for the amplification to occur.

To describe the concept of population inversion, we have implicitly assumed an atomic system consisting of only two energy levels. However, it is impossible to produce population inversion with such a system, since once the transparency condition is reached ($N_2 = N_1$) the absorption and stimulated emission processes would compensate each other. Real laser materials are usually composed at atomic level by a very large number of levels, each of them with their excitation and relaxation processes. Therefore a more appropriate representation of an optical amplification process must involve more than two energy levels. Typical gain material can be however modeled using a three- or

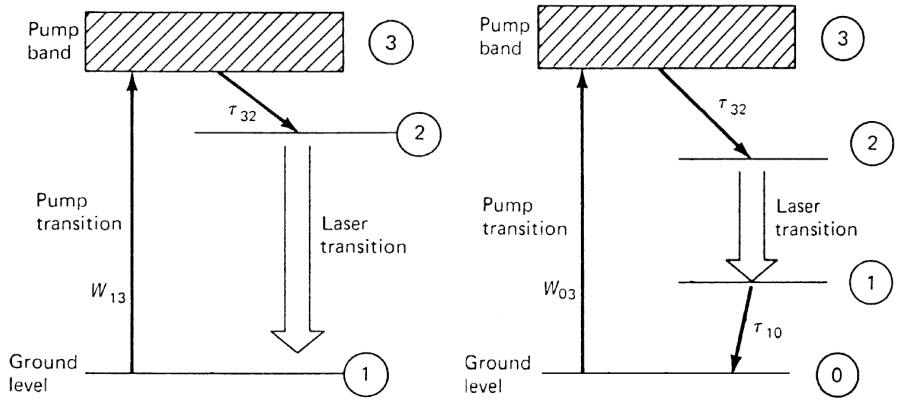

Figure 2.10 – Schematic representation of the energy level diagram of (a) a three-level and (b) a four-level laser system. Adapted from ref. [84].

four-level system. A schematic illustration of such system is shown in Fig. 2.10.

In a three-level system, after an atom is excited to level 3 (the pump band), it rapidly decays to level 2, through a non-radiative process characterized by a relaxation time τ_{32}. After a time τ_{21}, which represents the fluorescent lifetime of level 2, the atoms return to the ground state by emitting a photon. This photon emission is spontaneous or stimulated (and thus coherent) depending on whether the pump intensity is below or above threshold. The general condition for population inversion is that the non-radiative process is faster than the radiative one, i.e. $\tau_{21} \gg \tau_{32}$. In the three-level system, given that the ground state coincides with the lower laser transition level, this condition is fulfilled only if the number of atoms in level 2 is such that:

$$N_2 > \frac{N_{\text{tot}}}{2} \tag{2.73}$$

where N_{tot} is the total number of atoms. Therefore the pump rate must be strong enough to satisfy this condition.

The four-level system is characterized by the presence of another energy state below the lower level of the laser transition. This allows to reach population inversion much more easily than what happen in the three-level system. In fact, the lower energy level of the laser transition can be considered relatively empty and, therefore, the condition $N_2 > N_1$ is reached almost immediately, provided that $\tau_{10} \ll \tau_{21}$, where τ_{10} is the relaxation time of the $1 \rightarrow 0$ transition.

2.3.3 Gain of a generic optical amplifier

Let us now examine how a small optical signal is amplified by an optical amplifier by using the main parameters involved in this process. In Fig. 2.11 a basic scheme of an

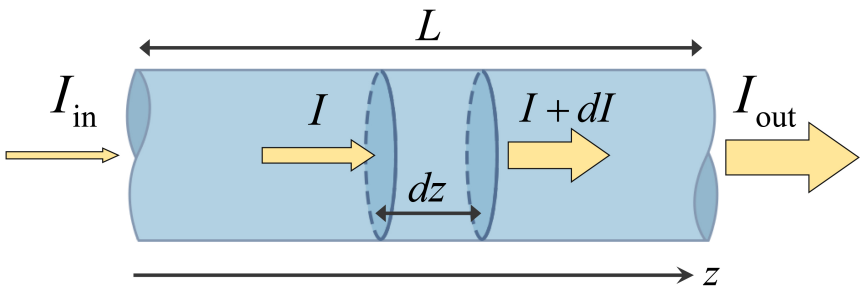

Figure 2.11 – Basic scheme of an optical amplifier of length L showing how the optical intensity increases in a thin slice of gain medium dz.

optical amplifier of length L is depicted, where I_{in} and I_{out} are the intensities entering and leaving the amplifier respectively.

We define the amplification factor G of the amplifier as $G \equiv I_{\text{out}}/I_{\text{in}}$, while the gain coefficient g is related to the fractional increase in intensity dI/I of the wave propagating through a small slab of thickness dz as following:

$$dI(z) = I(z)g(z)dz \tag{2.74}$$

The solution of the above equation gives the total single-pass gain G of the amplifier:

$$\frac{I(L)}{I(0)} = G = \exp\left[\int_0^L g(z)dz\right] \tag{2.75}$$

In general the gain coefficient depends on the coordinate z. For sufficiently high pumping level of the gain medium, the gain $g(z)$ at position z of the gain medium is given by [84]:

$$g(z) = \frac{g_0}{(1+\frac{I(z)}{I_s})^x} \tag{2.76}$$

where g_0 is the small-signal gain coefficient, characteristic of the gain medium, $I(z)$ is the intensity of the signal at position z and I_s is the saturation intensity defined as the signal power for which the small-signal gain is reduced by one half of its initial value. Specifically, the saturation intensity is given, depending on the type of the atomic system of the gain medium, by [85, 86]:

$$I_s = \frac{h\nu_s}{\sigma_{es}\tau_2} \quad \textit{(for a four-level system)} \tag{2.77}$$

$$I_s = \frac{h\nu_s}{2\sigma_{es}\tau_2} \quad \textit{(for a three-level system)} \tag{2.78}$$

where h is the Planck constant, ν_s is the frequency of the signal, τ_2 is the upper-state

lifetime, while σ_{es} is the emission cross-section of the quantum transition at the signal wavelength. In the case of fiber amplifier, the saturation intensity can be expressed with the following general formula [87]:

$$I_{\text{s}} = \frac{h\nu_{\text{s}}}{(\sigma_{\text{es}} + \sigma_{\text{as}})\tau_2} \tag{2.79}$$

where σ_{as} is the absorption cross-section of the quantum transition at the signal wavelength.
In Eq. 2.76, the parameter x indicates the nature of the spectral broadening of the lineshape function that characterizes the gain medium. Specifically, $x = 1$ for homogeneously broadened lineshape functions, while $x = 0.5$ holds for inhomogeneous broadening. Assuming, for simplicity, an homogeneous broadening, the integration of Eq. 2.74 over the length of the gain medium yields the following result:

$$\int_{I_{\text{in}}}^{I_{\text{out}}} \left(\frac{1}{I(z)} + \frac{1}{I_{\text{s}}}\right) dI(z) = \int_0^L g_0 dz$$

$$\ln\left(\frac{I_{\text{out}}}{I_{\text{in}}}\right) + \frac{I_{\text{out}} - I_{\text{in}}}{I_{\text{s}}} = g_0 L$$

$$\ln G + \frac{I_{\text{in}}(G-1)}{I_{\text{s}}} = g_0 L$$

$$\frac{I_{\text{in}}}{I_{\text{s}}} = \frac{\ln(G_0/G)}{G-1} \tag{2.80}$$

where $G_0 = \exp(g_0 L)$ is the small-signal single-pass gain for the whole length of the amplifier.

A plot of the above equation is shown in Fig. 2.12 for different values of G_0. We note that from this expression, the steady-state gain at any level of the input signal can be retrieved by knowing the small-signal gain coefficient of the gain medium.

Small signal approximation

In the case where the intensity of the signal is small enough such that $I \ll I_{\text{s}}$, $g \approx g_0$, and Eq. 2.74 can be written in the following simple form:

$$\frac{dI(z)}{I(z)} = g_0 dz \tag{2.81}$$

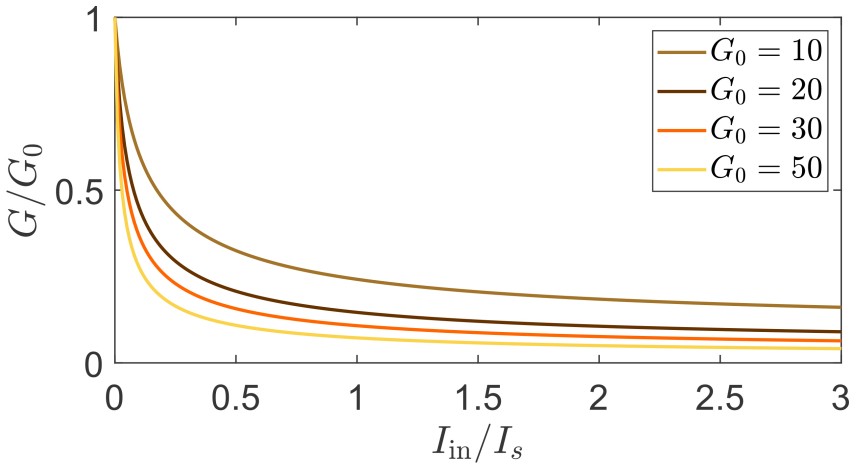

Figure 2.12 – Single-pass gain of an optical amplifier as a function of the the optical intensity of the input signal plotted for different values of the small-signal single-pass gain G_0.

which can directly integrated to give:

$$I(z) = I(0)e^{g_0 z} \tag{2.82}$$

The total gain in this case is given by:

$$G = e^{g_0 L} = e^{G_0} \tag{2.83}$$

where G_0, in the case of fiber amplifier, is given by [87]:

$$G_0 = g_0 L = \frac{\phi_{\text{p}}(\sigma_{\text{es}} + \sigma_{\text{as}})\tau_2 P_{\text{a}}}{Ah\nu_{\text{p}}} - a_{\text{l}} \tag{2.84}$$

where:
ϕ_{p} = quantum pumping efficiency
P_{a} = absorbed pump power
A = core area cross section
a_{l} = total absorption loss in the amplifier
ν_{p} = frequency of the pump

Large signal approximation

For signal intensities that fulfill the condition $I \gg I_{\text{s}}$, Eq. 2.74 simplifies to:

$$\frac{dI(z)}{dz} \simeq g_0 I_{\text{s}} \tag{2.85}$$

and, integrating over z, we obtain:

$$I_{\text{out}} - I_{\text{in}} \simeq g_0 I_{\text{s}} L \tag{2.86}$$

We note that, unlike the small-signal case, the output intensity of the amplifier increases linearly with the length of the gain medium rather than exponentially. Similarly, the total gain, which can be found by dividing the above equation by I_{in}, is also linear with L:

$$G \simeq 1 + \frac{I_{\text{s}}}{I_{\text{in}}} g_0 L \tag{2.87}$$

2.3.4 Gain of a fiber amplifier

So far, we have assumed that the excitation rate is uniform over the length of the gain medium, meaning that the number of atoms excited state is constant over the z coordinate. Although this assumption represents a good approximation for most practical cases, it loses its validity when dealing with fiber lasers and amplifiers, where the intensity of the pump decreases while propagating through the doped fiber. In such cases we have to solve Eq. 2.74 taking into account the dependence of the gain on the z coordinate.

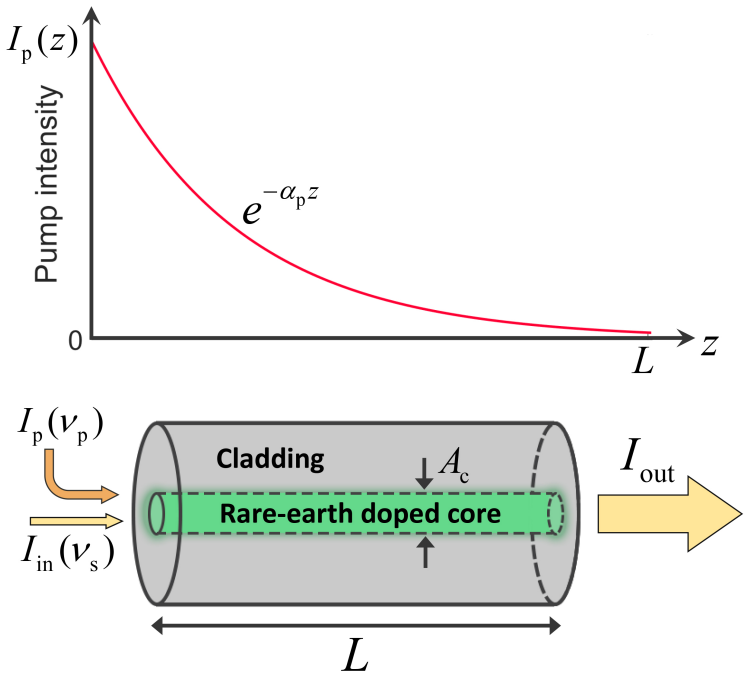

Figure 2.13 – Section of a rare-earth doped fiber amplifier with an illustrative graph of the pump intensity evolution along the doped fiber.

Let us consider a fiber of length L doped with a certain concentration N of rare-earth ions, and let suppose that the pump light at frequency ν_p is coupled into the core with cross-sectional area A_c, as schematically illustrated in Fig. 2.13. Assuming for simplicity that most of the rare-earth ions remains in the ground state ($N_0 \approx N$), we can consider the absorption coefficient α_p approximately independent on the position z along the fiber. Therefore, the pump light exponentially decreases with z according to the Beer's law [88]:

$$I_\mathrm{p}(z) = I_\mathrm{p0} e^{-\alpha_\mathrm{p} z} \tag{2.88}$$

where $\alpha_\mathrm{p} \approx N_0 \sigma_\mathrm{p}$, with N_0 the number of ions per unit volume in the ground state and σ_ap the pump absorption cross-section. To correlate the gain coefficient of the amplifier to the pump light evolution along the fiber, we first express it in terms of level populations. Without entering into the detail of every rare-earth material and its spectroscopic characteristics, we will assume here that the gain medium can be modeled with a four-level atomic system. In such a case, the gain coefficient can be expressed as [89]:

$$g(z) \simeq N_2(z)\sigma_\mathrm{es} = \mathcal{R}(z)\tau_2\sigma_\mathrm{es} \tag{2.89}$$

where N_2 is the population of the excited-state level of the laser transition, and $\mathcal{R}(z)$ is the excitation rate, which can be expressed as [32]:

$$\mathcal{R} = N W_\mathrm{p}(z) = N \frac{I_\mathrm{p}(z)\sigma_\mathrm{p}}{h\nu_\mathrm{p}} \tag{2.90}$$

where W_p is the transition probability per unit time for the single rare-earth ion. Inserting Eq. 2.90 into 2.89, we obtain the gain coefficient in the doped-fiber as a function of the z coordinate:

$$g(z) = N \frac{I_\mathrm{p}(z)\sigma_\mathrm{p}\sigma_\mathrm{es}\tau_2}{h\nu_\mathrm{p}} = \frac{\alpha_\mathrm{p}\sigma_\mathrm{es}\tau_2}{h\nu_\mathrm{p}} I_\mathrm{p}(z) \tag{2.91}$$

To find the expression of the total (single-pass) gain of the amplifier we solve Eq. 2.74 using the formula we just derived for $g(z)$, obtaining:

$$\int_{I_\mathrm{in}}^{I_\mathrm{out}} \frac{dI}{I} = \int_0^L g_(z) dz$$

$$\ln\left(\frac{I_\mathrm{out}}{I_\mathrm{in}}\right) = \frac{I_\mathrm{p0}\sigma_\mathrm{es}\tau_2}{h\nu_\mathrm{p}} \left(1 - e^{-\alpha_\mathrm{p} L}\right)$$

$$\ln G = \frac{I_\mathrm{p0}\sigma_\mathrm{es}\tau_2}{h\nu_\mathrm{p}} \tag{2.92}$$

where, in the last step, we have assumed that the pump light is completely absorbed by the doped fiber ($\alpha_p L \gg 1$). We note that, in such a case, the total gain depends neither on the ion concentration nor on the length of the doped fiber.

2.3.5 Threshold condition for fiber laser oscillation and laser output efficiency

The positive feedback in a fiber laser can be realized in different ways. Cavity configurations based on Fabry-Perot cavity are usually designed with fiber Bragg gratings (FBGs) or fiber loop mirrors as reflective elements. Layouts that include external dielectric mirrors are also common, although this solution may lead to a significant loss of power if the alignment between the lens and the mirror is not perfect. A cost effective solution is represented by the ring configuration, which can be made by simply connecting together one input and one output port of a directional coupler to the two ends of a doped-fiber. This type of laser, used in unidirectional configuration (e.g. inserting an isolator to block one of the two counter-propagating waves), does not suffer of spatial-hole burning given that there is no standing-wave interference pattern along the gain medium.

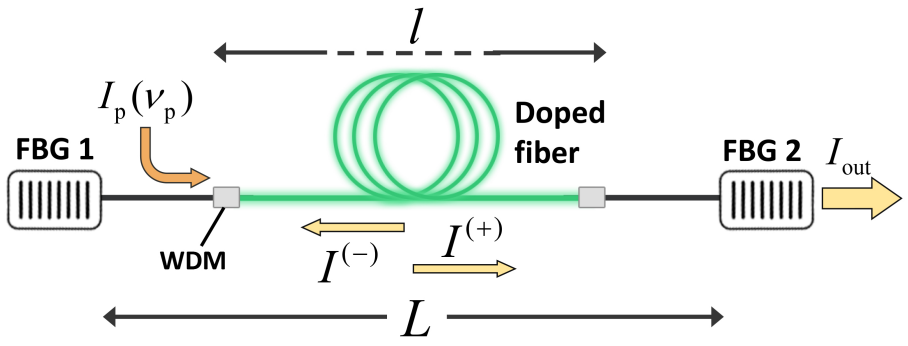

Figure 2.14 – Basic scheme of a fiber laser in a Fabry-Perot configuration in which two FBGs act as reflective elements. WDM: wavelength division multiplexer.

To derive the threshold condition for laser oscillation, we will consider (without loss of generality) a fiber cavity in the Fabry-Perot configuration with two FBGs as reflective elements, as the one depicted in Fig. 2.14. Let be $E(t) = E_0 \exp(j\omega t)$ the electric field of the wave at the FBG 1 ($z = 0$), and $r_1 = \sqrt{R_1}\exp(j\psi_1)$ and $r_2 = \sqrt{R_2}\exp(j\psi_2)$ the field reflective coefficients of the FBG 1 and 2 respectively. The doped-fiber provides a total gain $G = I_{out}/I_{in}$ for the intensity and is characterized by a length l, a cross section core area A and a refractive index n_d. Taking into account the attenuation and the phase delay experienced by the wave within the cavity, which are given respectively by $\exp(-\alpha L)$ and $\phi_{RT} = 2\omega/cL'$, the electric field $E'(t)$ at the FBG 1 after one cavity

round-trip will be:

$$E'(t) = E_0 r_1 r_2 G \exp\{j[\omega t - (2\omega/c)L'] - \alpha L\} \tag{2.93}$$

where $L' = L_c + n_d l$ is the optical path in the cavity, with $L_c = L - l$, and c is the speed of light in vacuum. To fulfill the threshold condition for lasing oscillation, for which the loop gain must be equal to 1, we impose that $E' = E$, obtaining:

$$r_1 r_2 G \exp\{j[(2\omega/c)L'] - \alpha L\} = 1 \tag{2.94}$$

From this equation we note that the loop gain is a complex quantity. Therefore the threshold condition breaks down into two conditions: one for the modulus, which must be equal to 1, and one for the phase, which, as we have already seen in paragraph 2.1.2, must be equal to $2m\pi$, with m positive integer. The corresponding equations are:

$$\sqrt{R_1 R_2} G_{th} e^{-\alpha L} = 1 \tag{2.95}$$

$$2(\omega/c)L' + \psi_1 + \psi_2 = 2m\pi \tag{2.96}$$

From the condition on the phase we obtain the longitudinal modes of the laser:

$$\nu_m = \frac{c}{2L'}\left(m + \frac{\psi_1 + \psi_2}{2\pi}\right) \tag{2.97}$$

which, likewise the resonance modes of a passive resonator, are equally spaced over the frequency at discrete intervals $\Delta\nu = \nu_{m+1} - \nu_m$.
The condition on the modulus gives, instead, the threshold value G_{th} of the total gain of the doped-fiber and, therefore, the threshold value g_{th} of the gain coefficient per unit length:

$$\ln G_{th} = \alpha L + \frac{1}{2}\ln\left(\frac{1}{R_1 R_2}\right) \Rightarrow \; g_{th} = \alpha + \frac{1}{2L}\ln\left(\frac{1}{R_1 R_2}\right) \tag{2.98}$$

By comparing the above equation with Eq. 2.92 and using the relation $I_{p0} = P_{th}/A$, we can derive the threshold value of the pump power to achieve laser oscillation:

$$P_{th} = \frac{Ah\nu_p \ln G_{th}}{\sigma_{es}\tau_2} = \frac{Ah\nu_p}{\sigma_{es}\tau_2}\left[\alpha L + \frac{1}{2}\ln\left(\frac{1}{R_1 R_2}\right)\right] \tag{2.99}$$

Laser output in continuous-wave (cw) regime

The discussion made in section 2.3.1 showed that the behavior above threshold of an oscillator depends on the saturation effect of the gain medium. Below threshold, the pump power is used to perform the population inversion required to bring the loop gain to 1. Part of the pump energy absorbed by the gain medium is converted into

light spontaneously emitted by the atoms (*fluorescence*). During this time any increase of pump power leads to an increased fluorescence since the threshold has not been yet reached. When the system reaches the threshold value, the spontaneous emission acts as "seed" light and the intra-cavity intensity exponentially increases until it gets to the saturation value and saturates the gain. At this point the gain gets clamped to its threshold value since the population of the excited state becomes constant and, therefore, any increase in pump power results in an increase of the laser output. From the saturated gain formula in Eq. 2.76 we can derive the expression of the intra-cavity intensity at threshold:

$$I = I_{\mathrm{s}} \left(\frac{g_0}{g_{th}} - 1 \right) \tag{2.100}$$

The intra-cavity intensity is the result of the superposition of the two counter-propagating waves inside the cavity. Each of them carries one half of the intra-cavity intensity, so that $I^{(-)} = I^{(+)} = I/2$, where $I^{(-)}$ ($I^{(+)}$) is the intensity of the left (right) propagating wave within the cavity, as depicted in Fig. 2.14. The total output intensity of the laser is then given by:

$$I_{\mathrm{out}} = T_1 I^{(-)} + T_2 I^{(+)} \tag{2.101}$$

Where T_1 and T_2 are the power transmission coefficients of mirror 1 and 2 respectively. In most laser systems, however, only one of the two mirrors is partially transmitting, e.g. $T_2 = T$, in which case we can write:

$$I_{\mathrm{out}} = T I^{(+)} = \frac{1}{2} T I = \frac{1}{2} T I_{\mathrm{s}} \left(\frac{g_0}{g_{th}} - 1 \right) \tag{2.102}$$

Now, considering that the pump power absorbed by the laser material can be expressed as [32]:

$$P_{\mathrm{p}} = \left[\frac{atoms\ excited}{time \times volume} \right] \left[\frac{absorbed\ energy}{excited\ atom} \right] [Volume] = \mathcal{R} h \nu_{\mathrm{p}} V \tag{2.103}$$

with $V = lA$ the volume of the doped fiber, and given the relation between g_0 and the excitation rate $\mathcal{R}$, which is: $g_0(\nu) = \mathcal{R}\tau_2 \sigma_{\mathrm{es}}(\nu)$, we can write the laser output power as:

$$P_{\mathrm{out}} = \frac{1}{2} A T I_{\mathrm{s}} \left(\frac{\mathcal{R}}{\mathcal{R}_{th}} - 1 \right) = \frac{1}{2} A T I_{\mathrm{s}} \left(\frac{P_{\mathrm{p}}}{P_{th}} - 1 \right) \tag{2.104}$$

where $P_{th} = \mathcal{R}_{th} h \nu_{\mathrm{p}} V$ is the threshold pump power. A more intuitive formula can be obtaining rearranging Eq. 2.104 as following:

$$P_{\mathrm{out}} = \eta_s (P_{\mathrm{p}} - P_{th}) \tag{2.105}$$

where

$$\eta_s = \frac{1}{2} AT \frac{I_\mathrm{s}}{P_{th}} \tag{2.106}$$

is the *slope efficiency* which is defined as the corresponding change in output power to an incremental variation in the pump power, i.e. $\eta_s = dP_\mathrm{out}/dP_\mathrm{p}$. Substituting Eq. 2.99 and 2.77 into the above equation we obtain an expression of the slope efficiency that is a function of two terms: (i) the ratio of the coupling loss to the total loss and (ii) the ratio between the photon energies at the laser and pump frequency:

$$\eta_s = T \frac{h\nu_\mathrm{s}}{h\nu_\mathrm{p}} \left(\frac{1}{2 \ln G_{th}} \right) = \frac{h\nu_\mathrm{s}}{h\nu_\mathrm{p}} \left[\frac{T}{2\alpha L + \ln (1/R_2)} \right] \tag{2.107}$$

A more general formula of the slope efficiency is the following [87]:

$$\eta_s = \eta_a \eta_c \frac{h\nu_\mathrm{s}}{h\nu_\mathrm{p}} \left[\frac{T}{2\alpha L + \ln (1/R_2)} \right] \tag{2.108}$$

which takes into account also the efficiency η_a with which the pump photons are absorbed by the gain material and the efficiency η_c with which absorbed pump photons are converted to photons at laser frequency.

2.4 Summary

In this chapter, we developed analytical models for passive optical resonators and explored the main characteristics of fiber lasers. Two alternative approaches for the analysis of optical resonators have been presented: a rigorous model also known as power coupling formalism, and the more abstract model of the temporal coupled-mode theory, which is based on energy coupling. Using these two theories we derived the equations of the transfer functions of a generic resonator that will be used in the subsequent chapters. Also the expressions of the main parameters that characterize the performance of optical resonators have been determined. In the second part of the chapter, the discussion moved towards the review of the basic principles of fiber laser. This topic started with a brief introduction on the main characteristics of an optical oscillator. We first derived the threshold condition for achieving laser oscillation. Then, we discussed the basic equations that govern the gain in a generic optical amplifier and, specifically, those for the fiber amplifier. Finally, the chapter ended with the description of the scheme of a fiber laser in a Fabry-Perot configuration and the derivation of its most important parameters.

3 Experimental and theoretical study on the Figure-9 laser

In the last twenty years, lasers incorporating NALM have been paid much attention owing to their capability to perform self-switching, pedestal suppression and pulse duration shortening by exploiting the fast nonlinear Kerr effect [90–92]. Specifically, when a short pulse at the input of the NALM is split in two by the coupler, the asymmetric position of the active fiber inside the loop causes an unequal intensity-dependent phase shift, which results in a different effective nonlinear length for the two counter-propagating pulses. This effect is also more pronounced for unbalanced splitting ratio of the coupler. The overall result is that the high-intensity portions of the pulse are transmitted and amplified, while the low-intensity portions are reflected back. This feature has been exploited to obtain mode-locking operation [58]. The figure-9 cavity is the most basic resonant structure for NALM-based fiber laser but can also be a sub-unit of more complex laser systems such as the figure-of-eight [93] and the theta cavity laser [94].

In this chapter I will present a theoretical model, describing the dependence of the figure-9 laser output power on the coupling ratio of the output coupler. Such theoretical model was developed considering all the relevant parameters of the laser cavity (loss coefficients, length, coupling coefficient of the coupler, reflectivity of the reflective element) and the characteristics of the gain unit (signal and pump wavelength, length of the doped fiber, doping material etc.) operating in the steady-state regime. The validity of the model will be demonstrated by comparing the theoretical curves with the experimental measurements performed using a home-made figure-9 Erbium-doped fiber laser having a fiber Bragg grating (FBG) as a reflective element. The model and results show that the laser output power is strongly dependent on the coupling coefficient of the coupler and the phase difference between the two waves traveling within the fiber loop. Also, we will see that an asymmetric behavior of the laser output, over the values of the coupling coefficient, occurs when the losses are not distributed uniformly within the loop.

3.1 Basic layout and theoretical models of the figure-9 laser

Among the numerous types of passive and active devices used in optical fiber communication systems, fiber loops and rings have been capable of fulfilling several critical functions such as those of optical filters, resonators, interferometers and delay lines [95–98]. Sagnac interferometers, nonlinear optical loop mirrors (NOLM) and the nonlinear amplifying loop mirror (NALM), are all devices based on the fiber loop structure, which consists of a directional coupler with the two output ports connected together [97, 99–101]. Moreover, many configurations of ring resonators containing one or more directional couplers in different positions within the cavity have been studied and investigated from the point of view of resonance condition, transmitted and reflected output and finesse [102–105]. Relying on these works, it did not take long to realize that these fiber layouts could represent ideal cavities for efficient and cost-effective fiber lasers. A fiber laser based on the Sagnac geometry, also called figure-9 (said figure-of-nine) laser, was first proposed by Cowle et al. in 1991 [57] and is basically a modified fiber loop reflector with a doped fiber placed inside the loop, i.e. a NALM, with a FBG connected to one of the remaining ports of the output coupler. A schematic illustration of such a fiber laser is shown in Fig. 3.1a. Its operating principle is based on two counter propagating waves undergoing amplification within the loop and interfering at the coupler. The resulting reflected and transmitted fields depend on the coupling ratio of the coupler and the phase shift acquired across the loop.

In order to explain the operating principles of the figure-9 laser, we can recall the expressions of the transmitted and the reflected fields of the geometrical core of this system, i.e. the fiber loop reflector [99]. The power amplification provided by the gain unit is represented by the block GU, while all the losses given by the passive components (WDMs, polarization controller, connectors...) placed in the path between the 2^{nd} and the 3^{rd} port of the coupler, are concentrated in the block labeled l, which is the power loss coefficient experienced by the two counter-propagating fields. For the moment, we will assume that these losses are uniformly distributed on both sides of the loop and that there is no birefringence in the fiber. The FBG serves both as wavelength selective element and highly reflective mirror of the cavity.

3.1.1 Theoretical scalar model

Let us consider the complex amplitudes of the electric field E_{in} of a light beam coming into the loop from port 1 of the coupler. Light incident on the coupler is split in two portions traveling in the loop in opposite directions (clockwise - CW and counter-clockwise - CCW) with respective electric field complex amplitudes E_{cw} and E_{ccw}. Recalling that for a coupler, there is a $\pi/2$ phase lag on the cross term with respect to the bar (or through) term, we can write the reflected and the transmitted fields, E_{R}

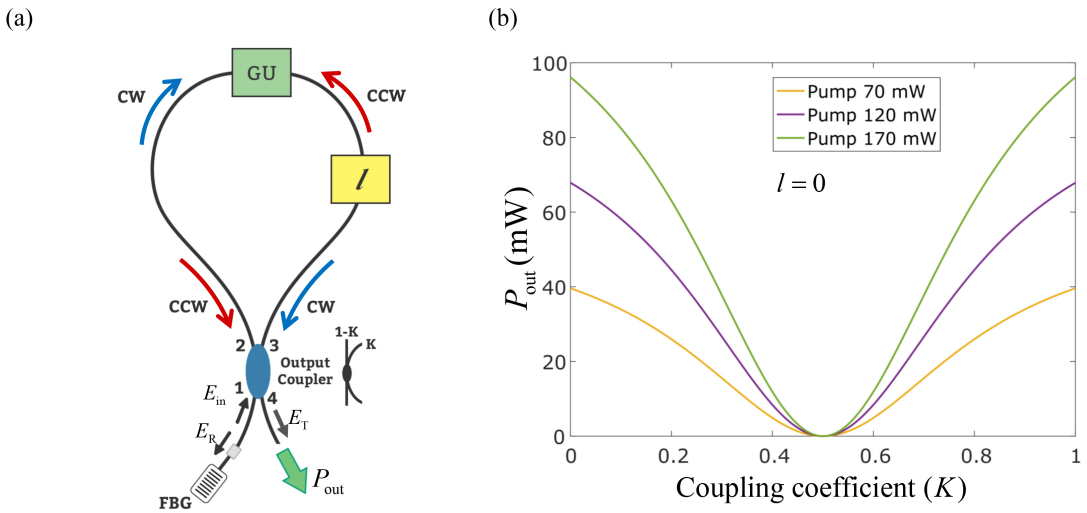

Figure 3.1 – (a) Basic scheme of the figure-9 laser with an FBG as a reflective element. (b) Plot of the output power of the figure-9 laser as a function of the coupling coefficient of the coupler for three different pump powers and assuming no intra-cavity (absorption) losses $l = 0$. GU: gain unit; CW: clockwise; CCW: counter-clockwise.

and E_{T}, respectively, as the superposition of the counter-propagating fields multiplied by the coupling ratio they had experienced passing through the coupler:

$$E_{\mathrm{R}} = \sqrt{1-\gamma}\sqrt{1-K}E_{\mathrm{ccw}} + j\sqrt{K}\sqrt{1-\gamma}E_{\mathrm{cw}} \tag{3.1}$$

$$E_{\mathrm{T}} = \sqrt{1-\gamma}\sqrt{1-K}E_{\mathrm{cw}} + j\sqrt{K}\sqrt{1-\gamma}E_{\mathrm{ccw}} \tag{3.2}$$

In the above equations γ is the power excess loss coefficient exhibited by the coupler, while K is the power cross-coupling coefficient. Assuming for the moment that the two counter-propagating fields go through the same optical path length, which means that there is no birefringence in the fiber, the expressions for the amplitudes of the electric fields of the CW and CCW waves are simply given by:

$$E_{\mathrm{cw}} = \sqrt{1-\gamma}\sqrt{1-K}\sqrt{1-l}\sqrt{G_{\mathrm{cw}}}E_{\mathrm{in}}e^{j\beta L} \tag{3.3}$$

$$E_{\mathrm{ccw}} = j\sqrt{1-\gamma}\sqrt{K}\sqrt{1-l}\sqrt{G_{\mathrm{ccw}}}E_{\mathrm{in}}e^{j\beta L} \tag{3.4}$$

where β is the propagation constant and L is the length of the portion of fiber between the second and the third port of the coupler. At the steady state regime, the gain in one direction equalizes the gain in the other direction, i.e. $G_{\mathrm{cw}} = G_{\mathrm{ccw}}$. Applying this condition and inserting equations 3.3 and 3.4 into 3.1 and 3.2 gives:

$$E_{\mathrm{R}} = 2j(1-\gamma)\sqrt{1-l}\sqrt{K(1-K)}\sqrt{G}E_{\mathrm{in}}e^{j\beta L} \tag{3.5}$$

$$E_{\mathrm{T}} = (1-\gamma)\sqrt{1-l}(1-2K)\sqrt{G}E_{\mathrm{in}}e^{j\beta L} \tag{3.6}$$

and the corresponding reflected and transmitted powers are therefore:

$$P_{\mathrm{R}} = |E_{\mathrm{R}}|^2 = 4(1-\gamma)^2(1-l)K(1-K)GP_{\mathrm{in}} \tag{3.7}$$

$$P_{\mathrm{T}} = |E_{\mathrm{T}}|^2 = (1-\gamma)^2(1-l)(1-2K)^2GP_{\mathrm{in}} \tag{3.8}$$

Once we derived the reflected and transmitted powers, we can find the expression for the steady state gain by imposing the threshold condition for lasing oscillation, which is:

$$R_{\mathrm{FBG}}P_{\mathrm{R}} = P_{\mathrm{in}} \tag{3.9}$$

where R_{FBG} is the reflectivity of the FBG. Imposing this condition into Eq. 3.7 we find the following expression for the steady-state gain:

$$G = \frac{1}{4}\frac{1}{R_{\mathrm{FBG}}(1-\gamma)^2(1-l)K(1-K)} \tag{3.10}$$

and, substituting into Eq. 3.8 we obtain the output power of the figure-9 laser as a function of the intra-cavity power:

$$P_{\mathrm{out}} = \frac{(1-2K)^2}{4R_{\mathrm{FBG}}K(1-K)}P_{\mathrm{in}} \tag{3.11}$$

In order to apply this analytical expression to our case, we need to include the equation of the gain of the amplifier which, in the saturation regime, can be expressed as following [106]:

$$G_{\mathrm{AMP}} = 1 + \frac{\lambda_{\mathrm{p}}}{\lambda_{\mathrm{s}}}\frac{P_{\mathrm{p}}}{P_{\mathrm{s}}^{\mathrm{in}}} \tag{3.12}$$

where $P_{\mathrm{s}}^{\mathrm{in}}$ is the total signal power entering the amplifier. In this case, since we have assumed that the losses are uniformly distributed on both sides of the fiber loop, $P_{\mathrm{s}}^{\mathrm{in}}$ is given by $P_{\mathrm{s}}^{\mathrm{in}} = (1-\gamma)\sqrt{1-l}P_{\mathrm{in}}$.
Finally, by imposing that $G = G_{\mathrm{AMP}}$ we can express the intra-cavity power as a function of the pump power and the parameters of the laser cavity:

$$P_{\mathrm{in}} = \frac{4R_{\mathrm{FBG}}K(1-K)(1-\gamma)\sqrt{1-l}}{1-4R_{\mathrm{FBG}}(1-\gamma)^2(1-l)K(1-K)}\frac{\lambda_{\mathrm{p}}}{\lambda_{\mathrm{s}}}P_{\mathrm{p}} \tag{3.13}$$

Therefore, if the loss coefficients γ and l, and the reflectivity of the FBG are known, by including the above equation into 3.8 we can write the output power of the figure-9 laser as a function of the pump power injected into the doped fiber:

$$P_{\mathrm{out}} = \frac{(1-\gamma)\sqrt{1-l}\,(1-2K)^2}{1-4R_{\mathrm{FBG}}(1-\gamma)^2(1-l)K(1-K)}\frac{\lambda_{\mathrm{p}}}{\lambda_{\mathrm{s}}}P_{\mathrm{p}} \tag{3.14}$$

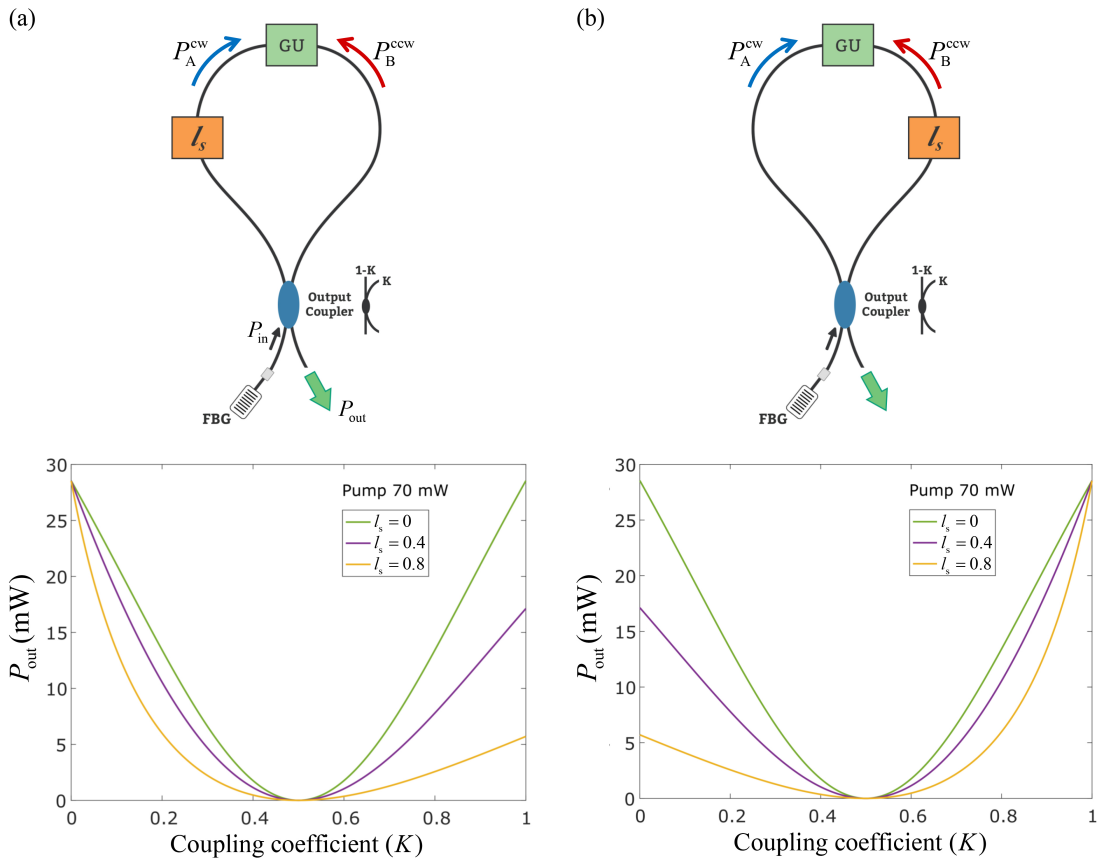

Figure 3.2 – On top: Basic scheme of the figure-9 laser assuming local loss placed (a) on the same side or (b) the opposite side with respect to the FBG. On the bottom: Corresponding output power of the figure-9 laser, obtained with 70 mW of pump power, plotted as a function of the coupling coefficient for three different values of the local loss factor l_s.

The corresponding plot as a function of the coupling coefficient of the coupler and, assuming no intra-cavity absorption loss ($l = 0$), is shown in Fig. 3.1b for different pump powers. As expected, the output power increases with unbalanced coupling coefficients and the minimum transmission is reached with the 50/50 coupler. This is due to the intrinsic effect of the fiber loop mirror, which, in absence of birefringence, forces the intra-cavity power to go towards the branch containing the FBG.

A less intuitive behavior is found when the losses are not uniformly distributed across the loop, in which case the two contributions to the total signal power entering the amplifier are no longer equally affected by the losses. In fact, assuming a local loss factor l_s, as shown in Fig. 3.2a and 3.2b, the total signal power entering the doped fiber depends on the position of the local loss within the loop with respect to the FBG. Specifically, denoting P_A^{cw} and P_B^{ccw} the power entering the gain unit from port 1 and port 2 respectively, their expression, as a function of the local losses and the coupling

coefficient, are listed below for the two cases:

Case 1	Case 2
$P_A^{cw} = (1-\gamma)\sqrt{1-l}\,(1-K)(1-l_\mathrm{s})P_\mathrm{in}$	$P_A^{cw} = (1-\gamma)\sqrt{1-l}\,(1-K)P_\mathrm{in}$
$P_B^{ccw} = (1-\gamma)\sqrt{1-l}\,KP_\mathrm{in}$	$P_B^{ccw} = (1-\gamma)\sqrt{1-l}\,K(1-l_\mathrm{s})P_\mathrm{in}$

where case 1 refers to the layout in Fig. 3.2a, while case 2 corresponds to the layout in Fig. 3.2b. From the total signal power entering the amplifier $P_\mathrm{s}^\mathrm{in} = P_A^{cw} + P_B^{ccw}$, we obtain the total intra-cavity power for the two cases, which is given by:

Case 1

$$P_\mathrm{in} = \frac{4R_\mathrm{FBG}K(1-K)(1-\gamma)\sqrt{1-l}(1-l_\mathrm{s})}{[K+(1-K)(1-l_\mathrm{s})][1-4R_\mathrm{FBG}(1-\gamma)^2(1-l)(1-l_\mathrm{s})K(1-K)]}\frac{\lambda_\mathrm{p}}{\lambda_\mathrm{s}}P_\mathrm{p} \tag{3.15}$$

Case 2

$$P_\mathrm{in} = \frac{4R_\mathrm{FBG}K(1-K)(1-\gamma)\sqrt{1-l}(1-l_\mathrm{s})}{[K(1-l_\mathrm{s})+(1-K)][1-4R_\mathrm{FBG}(1-\gamma)^2(1-l)(1-l_\mathrm{s})K(1-K)]}\frac{\lambda_\mathrm{p}}{\lambda_\mathrm{s}}P_\mathrm{p} \tag{3.16}$$

We note that in Case 1 the local losses term in the expression of P_in is multiplied by K, while in Case 2 by $1-K$. This results in an asymmetry of the output power of the laser with respect to the coupling coefficient when $K \neq 0.5$, as clearly shown in Fig. 3.2a and 3.2b (on the bottom), in which P_out is plotted as a function of K for different values of the local loss factor. We can see that the higher the losses the more asymmetric the behavior, as one could expect. It should be noticed that this asymmetry is not given by the effect of the NALM as it is not caused by any nonlinear phase difference.

3.1.2 Theoretical vectorial model

In developing the theoretical scalar model, we have assumed that there is no birefringence in the fiber, which means that apart from the phase lag of $\pi/2$ given by the coupler, the light does not suffer any other phase delay and its state of polarization remains unchanged across the loop. In practice, there is always a small birefringence in the fiber that leads to a non-perfect superposition between the waves at the coupler. Therefore we built a vectorial model considering the two counter propagating waves with their respective orthogonal polarization components and propagation constants

along the two axis. The expressions of their electric fields are listed below:

$$\mathbf{E}_{\mathrm{cw}} = \sqrt{1-\gamma}\sqrt{1-K}\sqrt{G}E_{in}\begin{bmatrix}\hat{x}\, X_{\mathrm{cw}} e^{j\beta^{x}_{\mathrm{cw}}L} \\ \hat{y}\, Y_{\mathrm{cw}} e^{j\beta^{y}_{\mathrm{cw}}L}\end{bmatrix} \tag{3.17}$$

$$\mathbf{E}_{\mathrm{ccw}} = j\sqrt{1-\gamma}\sqrt{K}\sqrt{G}E_{in}\begin{bmatrix}\hat{x}\, X_{\mathrm{ccw}} e^{j\beta^{x}_{\mathrm{ccw}}L} \\ \hat{y}\, Y_{\mathrm{ccw}} e^{j\beta^{y}_{\mathrm{ccw}}L}\end{bmatrix} \tag{3.18}$$

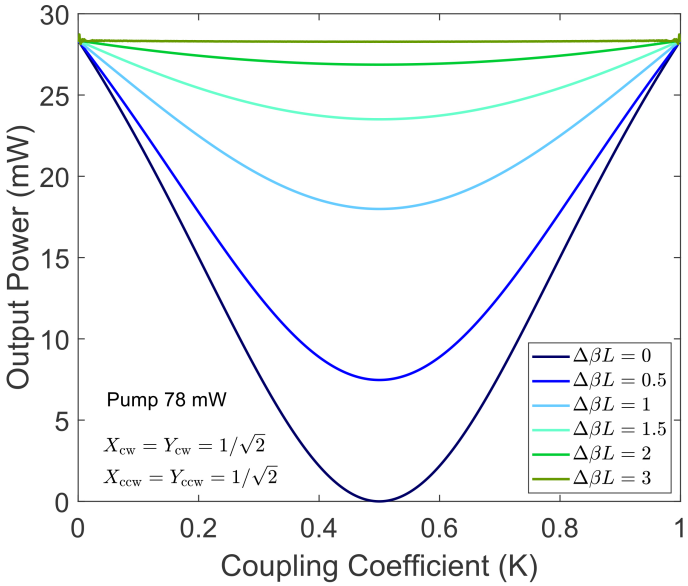

Figure 3.3 – Output power of the figure-9 laser as a function of the coupling coefficient of the coupler for different values of $\Delta\beta L$ obtained from the theoretical vectorial model (Eq. 3.21).

where X_{cw} (X_{ccw}) and Y_{cw} (Y_{ccw}) are the attenuation factors respectively for the x and y components of the electric field of the CW (CCW) wave, while β^{x}_{cw} (β^{x}_{ccw}) and β^{y}_{cw} (β^{y}_{ccw}) are the respective propagation constants. Substituting the above equations into 3.1 and 3.2 we obtain the vectorial form of the reflected and transmitted field from the fiber loop:

$$\begin{aligned}\mathbf{E}_{\mathrm{R}} = {} & j(1-\gamma)\sqrt{K}\sqrt{1-K}\sqrt{G}E_{\mathrm{in}}\begin{bmatrix}\hat{x}\, X_{\mathrm{ccw}} e^{j\beta^{x}_{\mathrm{ccw}}L} \\ \hat{y}\, Y_{\mathrm{ccw}} e^{j\beta^{y}_{\mathrm{ccw}}L}\end{bmatrix} + \\ & + j(1-\gamma)\sqrt{K}\sqrt{1-K}\sqrt{G}E_{\mathrm{in}}\begin{bmatrix}\hat{x}\, X_{\mathrm{cw}} e^{j\beta^{x}_{\mathrm{cw}}L} \\ \hat{y}\, Y_{\mathrm{cw}} e^{j\beta^{y}_{\mathrm{cw}}L}\end{bmatrix}\end{aligned} \tag{3.19}$$

$$\mathbf{E}_{\mathrm{T}} = (1-\gamma)(1-K)\sqrt{G}E_{\mathrm{in}} \begin{bmatrix} \hat{x}\, X_{\mathrm{cw}} e^{j\beta^{x}_{\mathrm{cw}}L} \\ \hat{y}\, Y_{\mathrm{cw}} e^{j\beta^{y}_{\mathrm{cw}}L} \end{bmatrix} - \\ - (1-\gamma)K\sqrt{G}E_{\mathrm{in}} \begin{bmatrix} \hat{x}\, X_{\mathrm{ccw}} e^{j\beta^{x}_{\mathrm{ccw}}L} \\ \hat{y}\, Y_{\mathrm{ccw}} e^{j\beta^{y}_{\mathrm{ccw}}L} \end{bmatrix} \quad (3.20)$$

By following the same procedure as for the scalar model, we can derive the output power of the laser, which is now also dependent on the birefringence of the CW and CCW waves:

$$P_{\mathrm{out}} = \frac{[(1-K)^2 a^2_{\mathrm{cw}} + K^2 a^2_{\mathrm{ccw}}] - 2K(1-K)(X_{\mathrm{cw}}X_{\mathrm{ccw}}cos(\Delta\beta_{\mathrm{cw}}L) + Y_{\mathrm{cw}}Y_{\mathrm{ccw}}cos(\Delta\beta_{\mathrm{ccw}}L))}{K(1-K)R_{\mathrm{FBG}}[(a^2_{\mathrm{cw}} + a^2_{\mathrm{cw}}) + 2(X_{\mathrm{cw}}X_{\mathrm{ccw}}cos(\Delta\beta_{\mathrm{cw}}L) + Y_{\mathrm{cw}}Y_{\mathrm{ccw}}cos(\Delta\beta_{\mathrm{ccw}}L))]} P_{\mathrm{in}} \quad (3.21)$$

where:

$$a^2_{\mathrm{cw}} = X^2_{\mathrm{cw}} + Y^2_{\mathrm{cw}} \qquad a^2_{\mathrm{ccw}} = X^2_{\mathrm{ccw}} + Y^2_{\mathrm{ccw}} \qquad \Delta\beta_{\mathrm{cw}} = \beta^{x}_{\mathrm{cw}} - \beta^{y}_{\mathrm{cw}} \qquad \Delta\beta_{\mathrm{ccw}} = \beta^{y}_{\mathrm{ccw}} - \beta^{x}_{\mathrm{ccw}} \quad (3.22)$$

This dependence is clearly shown in Fig. 3.3, where the output power curves, obtained with a pump power of $78\,\mathrm{mW}$, are plotted for different values of $\Delta\beta_{\mathrm{cw}}L = \Delta\beta_{\mathrm{ccw}}L = \Delta\beta L$ ranging from 0 to 3 radians and imposing $X_{\mathrm{cw}} = X_{\mathrm{ccw}} = Y_{\mathrm{cw}} = Y_{\mathrm{ccw}} = 1/\sqrt{2}$ and $R_{\mathrm{FBG}} = 0.9$. Interestingly, with values of $\Delta\beta L$ approaching to π, that is equivalent to have a π phase difference between the two counter-propagating waves, the output power is no longer dependent on the coupling coefficient of the coupler.

We also investigated the case in which the attenuation is not the same for the two counter-propagating waves, i.e. in presence of nonreciprocal losses ($a^2_{\mathrm{cw}} \neq a^2_{\mathrm{ccw}}$). To simplify the study, yet obtaining an overall understanding of the laser output power in such scenario, we conducted the study under the assumption of no birefringence ($\Delta\beta_{\mathrm{cw}}L = \Delta\beta_{\mathrm{ccw}}L = 0$). Also, we assumed an horizontal linear polarization for the electric field ($Y_{\mathrm{cw}} = Y_{\mathrm{ccw}} = 0$), thus varying the attenuation factor of the x component of only one of the two counter-propagating waves while leaving the other one unaltered. Figure 3.4 shows the result of this study where the output power was plotted as a function of K varying X_{cw} in Fig. 3.4a and X_{ccw} in Fig. 3.4b and imposing $X_{\mathrm{ccw}} = 1$ and $X_{\mathrm{cw}} = 1$, respectively, in Eq. 3.3.

We note that the symmetry between the two branches of the model is broken when the horizontal components of the two counter-propagating waves are not equal and the minimum value is shifted towards unbalanced coupling coefficients with increasing the difference $|X_{\mathrm{cw}} - X_{\mathrm{ccw}}|$. An interesting insight of this result can be found considering that, such symmetry breaking with respect of the coupling coefficient, provide one more degree of freedom on the laser output power. In fact, by inserting an optical

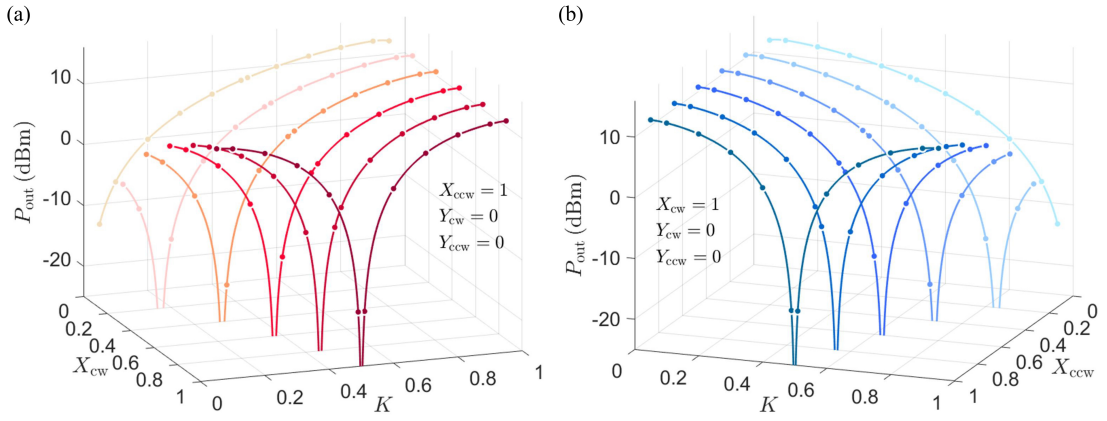

Figure 3.4 – 3-d plot of the output power of the figure-9 laser as a function of the coupling coefficient of the coupler obtained from the theoretical vectorial model varying (a) X_{cw} and (b) X_{ccw} and imposing $X_{\mathrm{ccw}} = 1$ and $X_{\mathrm{cw}} = 1$, respectively. The curves were obtained assuming no birefringence and an horizontal linear polarization of the electric field.

element capable to provide nonreciprocal attenuation, one can control the output transmission of the laser without the need of replacing the coupler or acting on the polarization controller.

3.2 Experimental investigation on the output power as a function of the coupling coefficient

To validate the theoretical model we built this fiber laser and tested it in laboratory. The experimental setup is illustrated in Fig. 3.5a. The laser cavity consists of a fiber loop reflector, formed between the input ports of a directional coupler, and a FBG plugged to one output port of the coupler. The gain unit, composed of 4 m of Erbium doped fiber (EDF) bi-directionally pumped by two 980 nm laser diodes through two 1x2 wavelength division multiplexers (WDMs), was placed at the center of the loop, while the output of the laser is taken from the other output port of the directional coupler.

Before evaluating the performance of the laser in terms of output power, the characterizations of the FBG and gain unit were performed. The reflection spectrum of the FBG, shown in Fig. 3.5b, was acquired using an high resolution (0.04 pm) optical spectrum analyzer (OSA). The spectral bandwidth, centered at 1551.35 nm, was found to be 40 pm, while the reflectivity, measured by taking as a reference a high reflectivity fiber reflector, was about 87%. The single-pass gain as a function of the input and output signal powers is shown in Fig. 3.6a and 3.6b respectively. The measurements were taken for five values of the total pump power at 21, 31, 78, 124 and 170 mW. From the

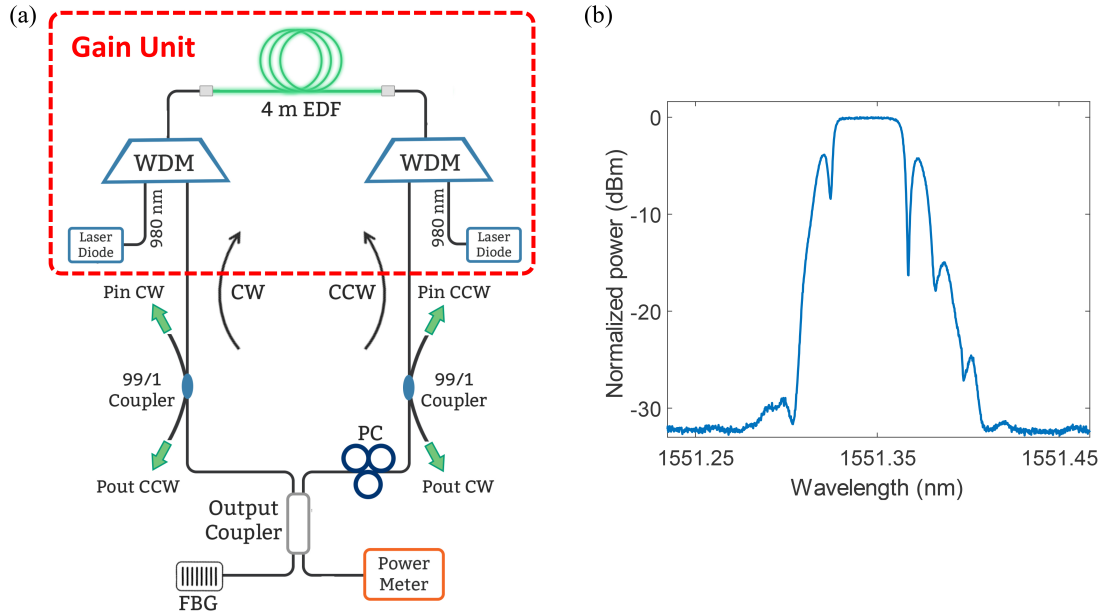

Figure 3.5 – (a) Experimental setup of the figure-9 laser. (b) Reflection spectrum of the FBG used as reflective element.

graphs we note that the saturation effect occurs at different values of the input and output powers. The insets, where the saturation powers are plotted as a function of the pump powers, show more clearly this behavior. We can see a linear dependence of the saturation powers with the pump powers as predicted by the theory [89].

After the characterization of the gain unit and the FBG, the measurements of the output power were performed for five pump powers above the threshold. Six directional couplers were used in the experiments with coupling ratios of 50/50, 60/40, 70/30, 80/20, 90/10 and 95/05. From the characterization of the couplers, a value of excess loss of about 0.2 dB was found for each of them. During the experiment the intra-cavity power was monitored using two 99/1 couplers connected to power meters, which measured the incoming and outgoing powers from the gain unit. In this way, we were able to evaluate the variation with the pump of the gain and the extinction ratio between the two counter propagating powers. Also, a polarization controller (PC) was placed inside the loop in order to change the phase difference between the two waves from 0 to π corresponding to the states in which the laser transmittance is minimized or maximized respectively.

The experiments were conducted in two separated steps. Firstly, the values of the output power were taken adjusting the PC to have the minimum transmission from the laser. Secondly, the values were taken for the opposite case, i.e. maximum laser transmission. The measurements of the output power as a function of the pump power collected minimizing and maximizing the laser transmission are shown in Fig. 3.7a and 3.7b respectively. These measurements were performed for all the configurations

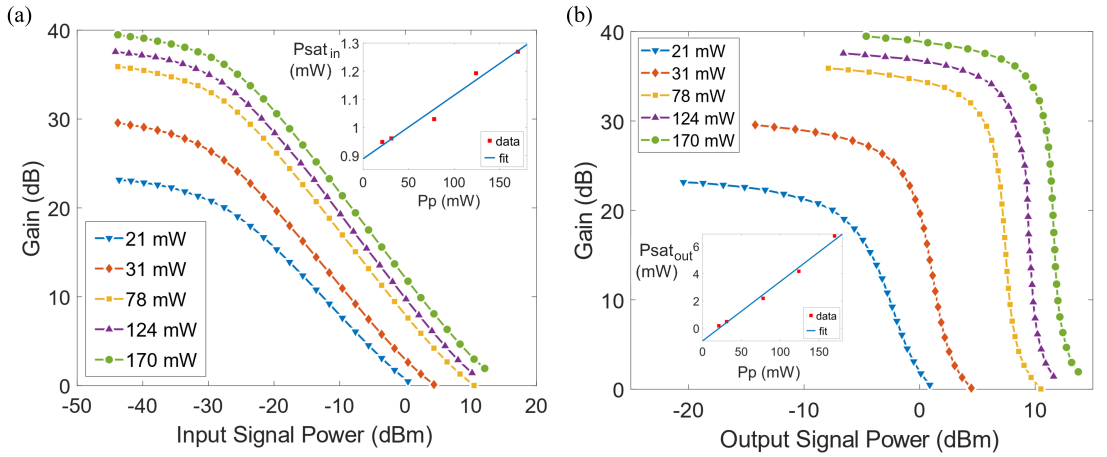

Figure 3.6 – Experimentally measured single-pass gain of the GU as a function of (a) the input signal power and (b) the output signal power; insets show (a) the saturation power and (b) the saturation output power as a function of the pump power.

of the laser, one for each coupling ratio of the couplers. From Fig. 3.7a, we note that the slope efficiency (values shown in the inset) increases with increasing the coupling ratio of the coupler used. The configuration with the 95/05 coupler shows the best slope efficiency, resulting in a good trade off with a greater value of the threshold pump power, which was about 18 mW. The measurements in Fig. 3.7b, relative to the maximized laser transmission, were taken adjusting the PC in order to have a π phase difference between the two counter-propagating waves. This was achieved, by setting the polarization controller as a half wave plate with its fast axis at 45°, so that when the waves re-entered the coupler, their field vectors pointed in opposite directions leading to a full output transmission [99]. In this case, we can see that the slope efficiencies show less variations, ranging from 25.3% to 33.4% and symmetrical configurations behave with better efficiencies. The output power is also plotted as a function of the coupling coefficient of the couplers in Fig. 3.8a, for the highest values of the pump power, and compared with the curves resulting from the theoretical model presented in the previous section. The theoretical curves in the case of minimized laser transmission, were plotted assuming there was not any birefringence in the cavity, i.e. imposing $X_{\mathrm{cw}} = X_{\mathrm{ccw}} = Y_{\mathrm{cw}} = Y_{\mathrm{ccw}} = 1/\sqrt{2}$ and $\Delta\beta_{\mathrm{cw}}L = \Delta\beta_{\mathrm{ccw}}L = 0$ in Eq. 3.21, while the theoretical curves relative to the case of maximized laser transmission were plotted setting $\Delta\beta_{\mathrm{cw}}L$ and $\Delta\beta_{\mathrm{ccw}}L$ to π. The good agreement of the theoretical curves with the experiments demonstrates that the model describes rather well the behavior of the laser when the gain is saturated. The measured values of 0.44 and 0.32 were used in the expression of the intra-cavity power for the total loss coefficient l and the local loss coefficient l_{s} respectively. The presence of a local loss factor was due to the slightly higher insertion loss exhibited by one of the two 99/1 monitoring couplers and the PC. The effect of the local loss is visible in the inclination of the curves that slightly increases with increasing the coupling coefficient. Interestingly, by maximizing the

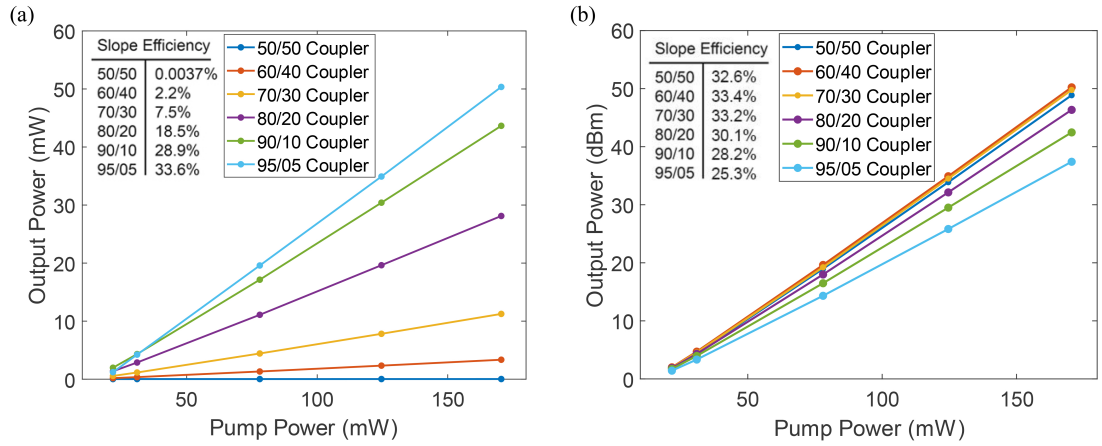

Figure 3.7 – Experimentally measured output power of the figure-9 laser as a function of the pump power (a) minimizing and (b) maximizing the laser transmission. Insets show the slope efficiency for each figure-9 configuration, one for each coupler used.

laser transmission the output power is no longer dependent on the coupling coefficient of the coupler. This is due to the complete destructive interference at the coupler when the PC is set as a half wave plate.

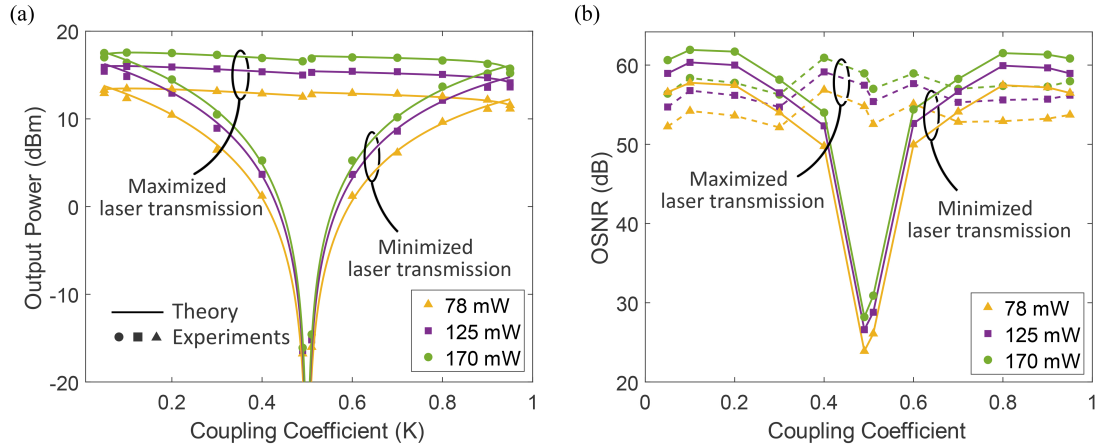

Figure 3.8 – (a) Comparison of the curves extracted from the theoretical models with the measured experimental values of the output power of the figure-9 laser as a function of the coupling coefficient of the coupler and for different pump powers in the case of minimized and maximized laser transmission. (b) Plot of the OSNR, measured using the optical spectrum analyzer, as a function of the coupling coefficient of the coupler in the case of minimized and maximized laser transmission.

The optical signal-to-noise ratio (OSNR) was also measured as a function of the coupling coefficient of the coupler for three different pump powers and plotted in Fig. 3.8b. The graph shows that the OSNR increases with increasing pump power for all the laser configurations, and the maximum value corresponds to 61.5 dB, which is reached

at a pump power of 170 mW using the 80/20 coupler. Moreover, we note that almost the same trend of the output power is obtained in both minimizing and maximizing the laser transmission.

3.3 Summary

The Figure-9 laser has recently attracted significant attention owing to its ultra-simple configuration that requires only one reflective element and because it can provide pulse shaping and pulse pedestal reduction in mode-locking operation, thanks to the nonlinear amplifying loop mirror (NALM) incorporated in its structure.

In this chapter a theoretical vectorial model of the Figure-9 laser, accompanied by experimental measurements, was described. The model aimed at investigating the performance and the characteristics of the laser in continuous wave operation, representing an initial foundation for a further understanding of the laser behavior in the pulsed regime. The results of the experimental measurements, well predicted by the model, showed a strong dependence of the Figure-9 laser output power on the coupling ratio of the directional coupler and the phase difference between the two counter-propagating waves within the fiber loop. In particular, we found that the laser exhibits a duplex behavior: when there is no phase difference between the two waves, the output power increases with unbalanced coupler and the minimum laser transmission is reached with the 50/50 coupler; however, when the phases of the two counter-propagating waves reach a difference of π, the laser transmission becomes independent on the coupling coefficient of the coupler. We have also seen that the presence of a nonreciprocal attenuation within the loop, offers the capability to control the laser transmission with any coupling ratio without acting on the polarization controller. However, to be implemented, this feature requires an optical nonreciprocal element, which contributes to increase the complexity and cost of the whole laser system. The noise performance of the laser was evaluated measuring the OSNR for all the different coupling coefficients. The results demonstrated that the best OSNR is obtained using the 80/20 coupler.

4 Time-bandwidth performance of resonant cavities with nonreciprocal coupling

The time-bandwidth limit (TBL) is a mathematical tenet, affecting all the reciprocal resonators, stating that the product between the bandwidth that can be coupled in a resonant system and its characteristic energy decay time is always equal to 1. Any attempt to reduce the losses of the resonant system, and hence store a wave for more time, will inevitably also reduce the bandwidth of the system. Photonics is particularly affected by the time-bandwidth limit. On the one hand, long interaction times are required for storage of optical pulses and efficient light-matter interaction (such as absorption, emission and nonlinear optical effects). On the other hand, broadband or rapidly varying, e.g. ultra-fast, signals are desirable since they are normally associated with larger amount of information and higher peak power.

In this chapter I will present an analytical and numerical model showing that the TBL can be overcome by implementing a nonreciprocal coupling in a generic resonant system. First, we will see how the spectral distribution and power balance of the reflected and intra-cavity fields are affected by the nonreciprocal coupling in such modeled resonant system. Then, by performing a full evaluation of the time-bandwidth product (TBP) of the modeled system, I will show that it represents a measure of the increased delay imparted to a light wave, with respect to what the bandwidth of the resonant structure would allow, in the reciprocal case, to the same amount of in-coupled power. Moreover, we will see that the TBP can be used as a figure of merit to indicate the increase in intra-cavity power enhancement, due to the nonreciprocal coupling, with respect to a reciprocal resonator.

4.1 General definition of the time-bandwidth product for a resonant system

The time-bandwidth product (TBP) is a relational property characterizing all individual resonators, whether they are of mechanical, acoustic, electrical or optical nature. It is usually defined as the product between the cavity linewidth ($\Delta\omega_{\mathrm{cav}}$) of a resonant system, and its characteristic decay time (τ_{D}) [31–33]. However this is a specific definition related to the particular case of a *reciprocal*, *linear* and *time-invariant* resonant system. A general definition of the TBP can be formulated in terms of the system's loading (ρ_{L}) and decay (ρ_{D}) energy rates as:

$$TBP = \Delta\omega_{\mathrm{acc}} \cdot \tau_{\mathrm{D}} = \frac{\Delta\omega_{\mathrm{acc}}}{\Delta\omega_{\mathrm{cav}}} = \frac{\rho_{\mathrm{L}}}{\rho_{\mathrm{D}}} \tag{4.1}$$

where $\Delta\omega_{\mathrm{acc}}$ and $\Delta\omega_{\mathrm{cav}}$ are the full width at half maximum of the Lorentzian functions associated, through the Fourier transform, respectively to the loading and decay curves of the intra-cavity energy.

As we already mentioned in chapter 2, the decay of the energy stored within a cavity is caused by the loss of power through radiative (transmission through coupling elements such as mirrors, couplers etc.) and non-radiative processes (absorption losses), which are taken into account by the out-coupling ρ_{out} and intrinsic ρ_0 energy decay rates, respectively. The total decay rate can therefore be expressed as: $\rho_{\mathrm{D}} = \rho_{\mathrm{out}} + \rho_0$. The Fourier transform relates ρ_{D} to $\Delta\omega_{\mathrm{cav}}$ by:

$$\Delta\omega_{\mathrm{cav}} = \rho_{\mathrm{out}} + \rho_0 = \frac{1}{\tau_{\mathrm{out}}} + \frac{1}{\tau_0} = \frac{1}{\tau_{\mathrm{D}}} \tag{4.2}$$

where τ_{out} and τ_0 are the decay times associated with the decay of the energy due to the radiative and non-radiative losses, respectively. Similarly, the loading curve depicts how fast the intra-cavity energy would exponentially grow if the resonator was 'fed' through the same processes but reversed in time. As a result, the loading rate can be expressed as $\rho_{\mathrm{L}} = \rho_{\mathrm{in}} + \rho_0$, with ρ_{in} and ρ_0 that now are the in-coupling rate and intrinsic loading rate of energy, respectively. In the same way as for the decay process, we can then relate the loading rate to the acceptance bandwidth of the resonator through the Fourier transform by:

$$\Delta\omega_{\mathrm{acc}} = \rho_{\mathrm{in}} + \rho_0 = \frac{1}{\tau_{\mathrm{in}}} + \frac{1}{\tau_0} = \frac{1}{\tau_{\mathrm{L}}} \tag{4.3}$$

(see Appendix A). In this case, ρ_{in} and ρ_0 play the role of energy sources instead of energy sinks like in the decay process. This concept is schematically illustrated in Fig. 4.1. In resonators with reciprocal coupling, the loading and decay processes are characterized by the same energy rate ($\rho_{\mathrm{L}} = \rho_{\mathrm{D}}$) and the system is said time-reversal symmetric. This translates in frequency to two identical Lorentzian distributions where, therefore,

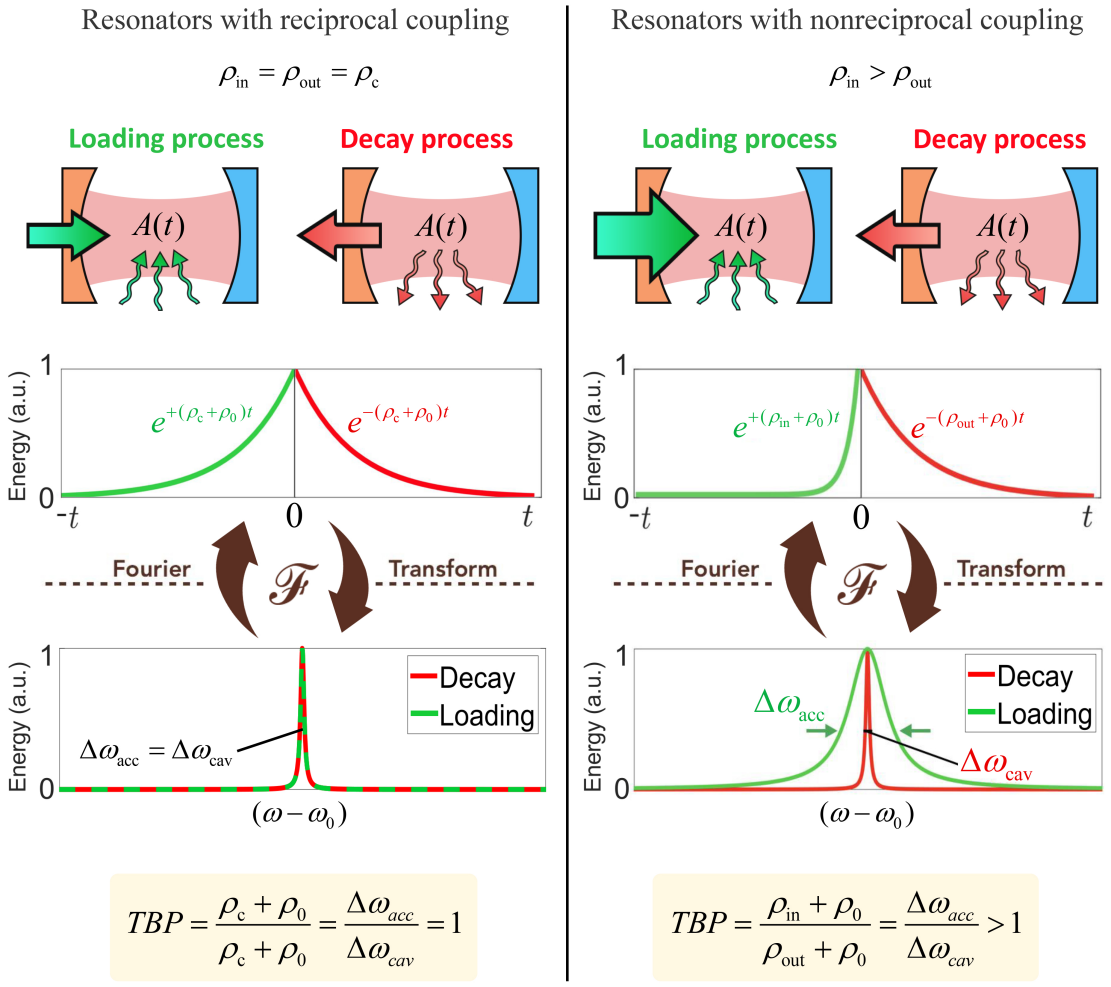

Figure 4.1 – Illustration of the energy loading and decay processes in resonators with reciprocal (left panel) and nonreciprocal (right panel) coupling and their associated resonance mode profiles. The TBP is given by the ratio between the acceptance and the cavity bandwidth which are the FWHM of the Lorentzian functions associated, through the Fourier transform, to the loading and decay curve respectively.

$\Delta\omega_{\mathrm{acc}} = \Delta\omega_{\mathrm{cav}}$. From Eq. 4.1 this results in a TBP = 1, a value referred to as the time-bandwidth limit (TBL). For such a system, the bandwidth of an incoming pulse must be equal to or smaller than the measured resonance linewidth in order to be entirely coupled in the reciprocal cavity. This means that long storage times automatically require narrow input bandwidths, while large bandwidths can be retained only for short periods of time. Conversely, in case of nonreciprocal coupling the time-reversal symmetry no longer holds since $\rho_{\mathrm{L}} \neq \rho_{\mathrm{D}}$, and the time-reversal operation leads to a loading process and its corresponding mode profile that are different from the decay process. In this case, the acceptance bandwidth does not coincide with the measured cavity linewidth and if the loading process can be made faster than the decay process, meaning that $\rho_{\mathrm{L}} > \rho_{\mathrm{D}}$, the system can show an arbitrary large TBP. Such scenario,

however, implies that the input energy rate must be decoupled from the cavity decay time, an operation that, in closed resonators, is achievable only through nonlinearity or breaking of time-invariance property of the system.

It should be noted that, even if the incident light is an arbitrary waveform, the optimum coupling in a resonator is the time reversed version of the decay curve, which corresponds to an exponentially increasing waveform [81, 82]. Therefore, the acceptance bandwidth should not be confused with the bandwidth of the actual injected signal as it represents the maximum input Lorentzian linewidth allowed by the resonator in one free spectral range (FSR). As a matter of fact, in practice, the energy within the resonator does not grow exponentially as light is being injected through the coupling element (usually a mirror or a coupler), but it rather depends on the time evolution of the input signal.

Based on these considerations, a nonreciprocal coupling is the necessary requirement to overcome the TBL. However, such condition can be achieved only through the breaking of the reciprocity property of the coupling junctions, through which the energy exchange of the resonant system with the outside world occurs. But why overcoming the TBL is so important? The answer to this question can be found looking beyond the purely mathematical aspect. We have explained so far that the TBL imposes a trade off between the bandwidth and the decay time of a resonant system. In practical terms, this trade off has a twofold effects: (i) the maximum amount of energy that can be stored within a time interval is dictated by the bandwidth of the Lorentzian resonance mode of the system; (ii) the time during which this energy is trapped is always the inverse of the resonance mode bandwidth. This means that if one wants to store a higher amount of energy, which then requires a larger bandwidth, the storage time will be inevitably reduced. On the other hand, any attempt to reduce the losses of the resonant system, and hence store energy for more time, will inevitably also reduce the bandwidth of the system. A TBP larger than 1 offers the possibility of decoupling the resonance mode (cavity) bandwidth from the *input* bandwidth of the system allowing to arbitrarily control the storage time without suffering from the restriction dictated by the cavity bandwidth. A further confirmation of this possibility can be obtained by rewriting the expression of the TBP as a ratio between the finesse related to $\Delta\omega_{\mathrm{cav}}$ and $\Delta\omega_{\mathrm{acc}}$ which we name *cavity* and *acceptance Lorentzian finesse*, $\mathcal{F}_{\mathrm{cav}}$ and $\mathcal{F}_{\mathrm{acc}}$ respectively:

$$TBP = \frac{\Delta\omega_{\mathrm{acc}}}{\Delta\omega_{\mathrm{FSR}}}\frac{\Delta\omega_{\mathrm{FSR}}}{\Delta\omega_{\mathrm{cav}}} = \frac{\mathcal{F}_{\mathrm{cav}}}{\mathcal{F}_{\mathrm{acc}}} \tag{4.4}$$

The physical meaning of this expression can be found by recalling that the cavity finesse calculated using the Lorentzian linewidth represents the number of round-trips (times 2π) before the energy stored in the resonator decays to $1/e$ of its original value [31]. Applying this definition also to the loading process, we can say that $\mathcal{F}_{\mathrm{acc}}$ is

the number of round-trips the intra-cavity energy takes to reach its final value, starting from $1/e$ of this value. Therefore, considering a certain amount of energy stored inside a resonator with $\rho_{\text{in}} > \rho_{\text{out}}$, a TBP > 1 implies that the decay time $\tau_{\text{D}} = 1/\rho_{\text{out}} + 1/\rho_0$ experienced by this energy is longer than that provided by a reciprocal resonator (TBP = 1) by an amount equal to the ratio $\mathcal{F}_{\text{cav}}/\mathcal{F}_{\text{acc}}$. It is thus obvious that overcoming the TBL would bring remarkable benefits for several applications ranging from the simple delay line system to nonlinear resonant systems, where coupling an amount of energy larger than that allowed by the system, would enhance the light-matter nonlinear interaction.

Moved by this objective, we developed a generalized theoretical model of a resonant cavity having a nonreciprocal coupling element to study the implication of the decoupling of input and output energy rates on the TBP of the system. The analysis is focused on the spectral distribution and the power balance between the reflected and intra-cavity fields, showing how their associated power spectra and the TBP of the system change depending on the degree of nonreciprocity, i.e. the difference between the in-coupling and out-coupling energy rate.

4.2 Theoretical model of a resonant system with nonreciprocal coupling

To analyze a resonant system with nonreciprocal coupling, we consider a Gires-Tournois (GT) resonator, which is an asymmetric Fabry-Perot resonator having one partially reflective mirror, while the other one is fully reflective [75]. An illustration of such system is depicted in Fig. 4.2, where A, A_{in} and A_{R} represent the complex amplitudes of the intra-cavity, the incoming and the (total) reflected wave respectively, while ρ_0 is the intrinsic, or non-radiative, energy decay rate that accounts for the energy loss due to absorption and scattering occuring in the intra-cavity medium. The mirror M2 is fully reflective, while ρ_{in} and ρ_{out} are the total in- and out-coupling radiative energy rates, respectively, acting through the partially reflective mirror M1. A Gires-Tournois resonator is perfectly suitable for modeling a resonant system with nonreciprocal coupling since the partially reflective mirror constitutes the only coupling junction. Therefore, the energy exchange of the resonant system with the outside world can be assessed using one dimensional vectors for the input and output energy rates. The treatment can easily be extended to multi-port resonant systems just by summing up the contribution of the in- and out-coupling energy rates of each port.

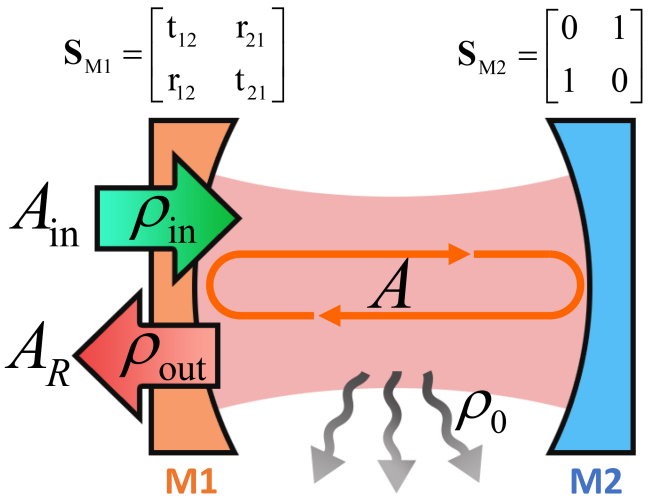

Figure 4.2 – Layout of a Gires-Tournois resonator with a nonreciprocal front mirror, whose transmission coefficients depend on the direction of wave propagation.

4.2.1 Parameters of the nonreciprocal coupling element

We can describe the transfer characteristic of the two mirrors by using the scattering matrix formalism that we have introduced in chapter 2, as shown below:

$$\mathbf{S}_{\mathrm{M1}} = \begin{bmatrix} \mathrm{t}_{12} & \mathrm{r}_{21} \\ \mathrm{r}_{12} & \mathrm{t}_{21} \end{bmatrix} \qquad \mathbf{S}_{\mathrm{M2}} = \begin{bmatrix} 0 & 1 \\ 1 & 0 \end{bmatrix} \tag{4.5}$$

where t_{12} (t_{21}) and r_{12} (r_{21}) are the complex transmission and reflection coefficients, respectively, of a wave incident from outside (inside) the resonator. The total in- and out-coupling energy rates ρ_{in} and ρ_{out}, of the system can be expressed as following:

$$\rho_{\mathrm{in}} = \frac{|\mathrm{t}_{12}|^2}{T_{\mathrm{RT}}} \qquad \rho_{\mathrm{out}} = \frac{|\mathrm{t}_{21}|^2}{T_{\mathrm{RT}}} \tag{4.6}$$

where T_{RT} is the cavity round-trip time.

A nonreciprocal coupling implies that ρ_{in} and ρ_{out} are different due to a nonreciprocal transmittance of the front mirror ($|\mathrm{t}_{12}|^2 \neq |\mathrm{t}_{21}|^2$). Consequently, the difference $|\mathrm{t}_{12}|^2 - |\mathrm{t}_{21}|^2$ can be seen as a measure of the *degree of nonreciprocity* of the system. It should be noted that this analytical model aims at studying the implication of decoupling input and output energy rates in a resonant system irrespective of the mechanism used to induce the nonreciprocal coupling, which, in any case, must ensure the conservation of energy [50, 52]. In particular, the model does not presume how the scattering matrix for the mirror M1 in Eq. 4.5 is generated, thus the origin of the nonreciprocity (e.g. external magnetic field bias, temporal variance, nonlinearity, etc.) [50, 107] does not have any impact on the TBP and the power balance of the system: as long as the

coupling junction has such scattering matrix, it can exhibit nonreciprocal coupling. In the following sections, we show that temporal variance is one way to reach this state, but other mechanisms, such as external magnetic field bias or nonlinearity, could also lead to the same outcome. One example can be found in Ref. [49], where the in-coupling and out-coupling energy rates are made unequal by exploiting the unidirectional propagation of surface magnetoplasmon in a magnetized semiconductor heterostructure.

4.2.2 Derivation of the frequency response

While the temporal coupled mode theory (TCMT), can be used to describe the spectral distribution of a resonant mode in an optical cavity, even in the context of nonreciprocity [80, 108], the equations on which it is based can approximate the spectral response of a resonator only under the assumption of weak coupling. Therefore, to derive the frequency response of the system, we use the power coupling formalism (PCF), since it allows to carry out an analysis unconstrained by coupling strength assumptions and that can also consider multiple resonant mode profiles. Another distinction is that the PCF gives, as a final result, the frequency response of the resonator, which has the shape of an Airy function, while the TCMT models the resonant system as a Lorentz oscillator, which is characterized by a single longitudinal resonant mode. This concept becomes clearer by looking at Fig. 4.3 that shows a comparison between the Airy distribution (solid lines) of the light transmitted through a FP resonator with the Lorentzian resonance mode profile (dashed lines) calculated using the TCMT at different mirrors reflectivity [109]. We note that at high mirrors reflectivity, meaning for weak couplings, there is a close to perfect agreement between the spectral shape of the Airy distribution (solid purple line) and its underlying Lorentzian lines (dashed purple line), i.e., the Airy function is rather well represented by the Lorentzian. However, with decreasing reflectivity of the mirrors, the linewidth of the Airy distribution broadens faster than that of the underlying Lorentzian lines so that the discrepancy between the two sets of spectra becomes more pronounced as we move away from the center resonance mode. This is explained by the fact that the Airy distribution is nothing else but the sum of the mode profiles of the longitudinal resonator modes and the faster broadening of the Airy linewidth ($\Delta\nu_{\mathrm{Airy}}$) simply arises from the fact that it sums up mode profiles (with the same linewidth $\Delta\nu_{\mathrm{c}}$ as the Lorentzian lines) that resonate at different frequencies. However, later on, we will see that the resonator losses are related to the linewidth of the Lorentzian lines rather than the linewidth of the Airy distribution.

The spectral distribution of the intra-cavity (A) and reflected (A_{R}) fields can be found starting from the general equations obtained for the Fabry-Perot in chapter 2, i.e. Eq. 2.12 and 2.25. Imposing $\mathrm{r_B} = \mathrm{r'_B} = 1$ and inserting the parameters for the GT resonator,

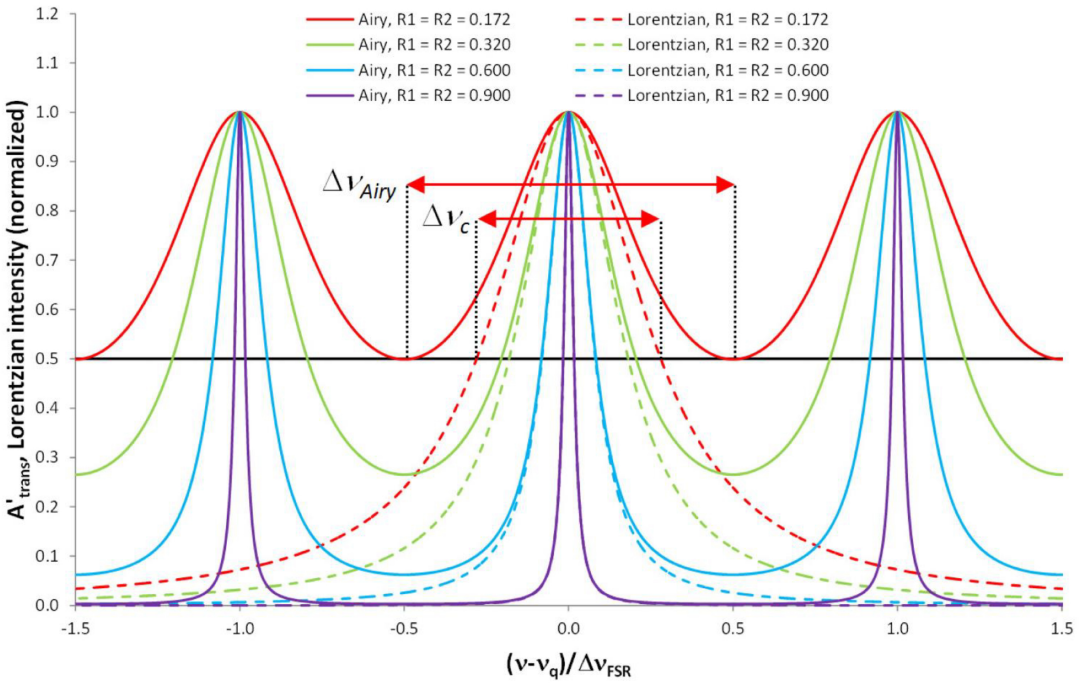

Figure 4.3 – Comparison between the Airy distribution of the light transmitted through a standard Fabry-Perot resonator (solid lines) with the Lorentzian resonance mode profile (dashed lines) calculated using the temporal coupled-mode theory at different mirrors reflectivity. (Adapted from ref. [109]).

gives:

$$A = \frac{\mathrm{t}_{12}}{1 - |\mathrm{r}_{21}| a_\mathrm{d} e^{-j\phi_\mathrm{RT}}} A_\mathrm{in} \tag{4.7}$$

$$A_\mathrm{R} = \left[\mathrm{r}_{12} + \frac{\mathrm{t}_{12}\mathrm{t}_{21} a_\mathrm{d} e^{-j(\phi_\mathrm{RT} - \phi^\mathrm{r}_{21})}}{1 - |\mathrm{r}_{21}| a_\mathrm{d} e^{-j\phi_\mathrm{RT}}} \right] A_\mathrm{in} \tag{4.8}$$

where $a_\mathrm{d} = e^{-\alpha_\mathrm{d} L_\mathrm{d}}$ is the field inner circulation factor that accounts for the non-radiative loss of the resonator, while ϕ_RT is the total round-trip phase delay, which, in this case, is given by the sum of the cavity round-trip phase delay $\phi_\mathrm{d} = \beta(2L_\mathrm{d})$ and the phase of r_{21} (ϕ^r_{21}). L_d, α_d and β are the cavity length, the intra-cavity power attenuation coefficient and the propagation constant, respectively.

Now, given that $\phi_\mathrm{RT} = 2m\pi + \Delta\phi_\mathrm{RT}$, where $\Delta\phi_\mathrm{RT}$ is the phase detuning from resonance, the exponential term in equations 4.7 and 4.8 can be rewritten as $e^{-j\Delta\omega T_\mathrm{RT}}$, in which $\Delta\omega = \omega - \omega_0$, and $T_\mathrm{RT} = 2L_\mathrm{d}/v_\mathrm{g}$ is the cavity round-trip time, with v_g the group velocity and ω_0 the resonance frequency. Also, defining the intrinsic energy decay rate as $\rho_0 = \alpha_\mathrm{d} v_\mathrm{g}$, we can rewrite the inner circulation factor in the denominator of equations 4.7 and 4.8 as $a_\mathrm{d} = e^{-(\rho_0 T_\mathrm{RT})/2}$. Using these relations and those in Eq. 4.6, we

finally obtain the spectral distribution of the intra-cavity and reflected fields of the GT resonator as a function of $\Delta\omega$, ρ_{in}, ρ_{out} and ρ_0:

$$A(\omega) = \frac{\sqrt{\rho_{\mathrm{in}}\, T_{RT}}}{1 - \exp[\ln(|\mathrm{r}_{21}|) - (\rho_0/2 + j\Delta\omega)T_{\mathrm{RT}}]} A_{\mathrm{in}}(\omega) \tag{4.9}$$

$$A_{\mathrm{R}}(\omega) = \left[\mathrm{r}_{12} + \frac{\sqrt{\rho_{\mathrm{in}}\rho_{\mathrm{out}}}T_{\mathrm{RT}} a_{\mathrm{d}} \exp\left[-j(\Delta\omega T_{\mathrm{RT}} - \phi^{\mathrm{r}}_{21})\right]}{1 - \exp[\ln(|\mathrm{r}_{21}|) - (\rho_0/2 + j\Delta\omega)T_{\mathrm{RT}}]}\right] A_{\mathrm{in}}(\omega) \tag{4.10}$$

where the field of the incident wave $A_{\mathrm{in}}(\omega)$ is assumed having a flat frequency distribution over one free spectral range (FSR $= 1/T_{\mathrm{RT}}$).

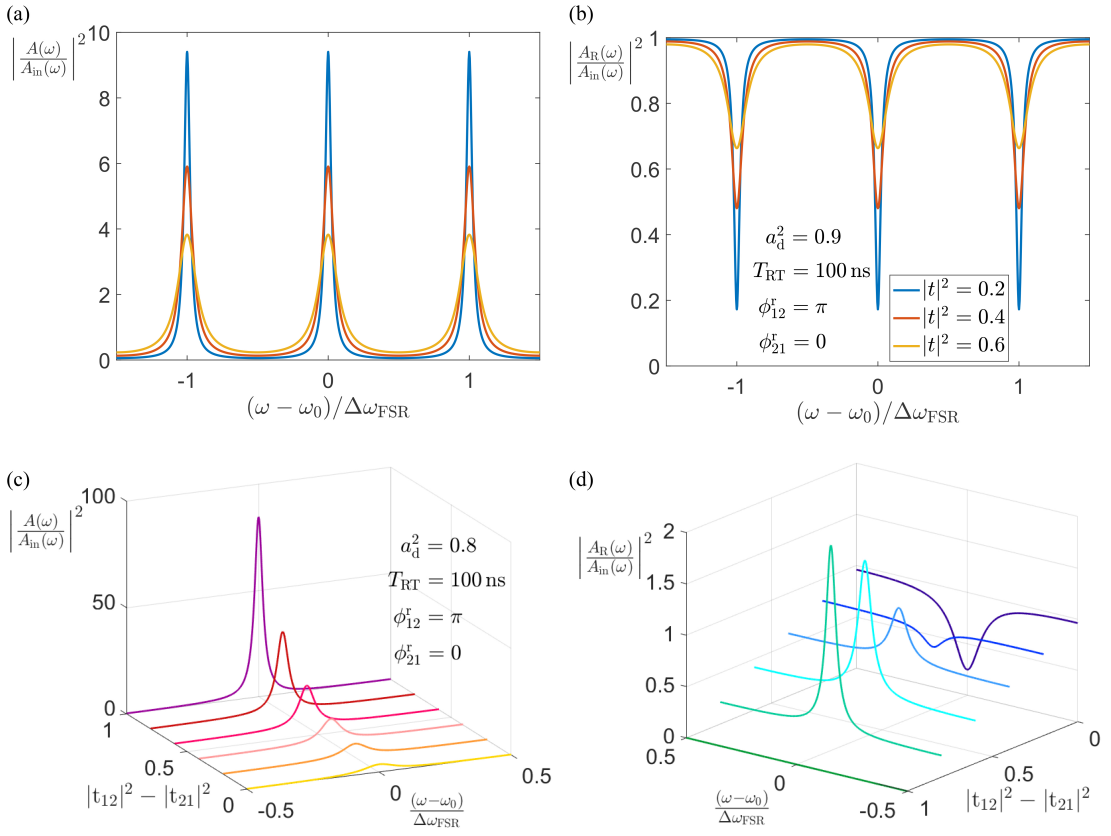

Figure 4.4 – On the top: Power spectra of (a) the intra-cavity and (b) reflected fields, normalized to the input power, of the GT resonator in case of reciprocal coupling ($|\mathrm{t}_{12}|^2 = |\mathrm{t}_{21}|^2 = |\mathrm{t}|^2$) and for different values of the power transmission coefficient of the front mirror. On the bottom: Power spectra of (c) the intra-cavity and (d) reflected fields, normalized to the input power, of the GT resonator in case of nonreciprocal coupling ($|\mathrm{t}_{12}|^2 \neq |\mathrm{t}_{21}|^2$) and for different degrees of nonreciprocity of the front mirror ($|\mathrm{t}_{12}|^2 - |\mathrm{t}_{21}|^2$).

Figures 4.4a and 4.4b show the power spectra of the intra-cavity and reflected fields, normalized to the input power, of the GT resonator in case of reciprocal coupling

($|t_{12}|^2 = |t_{21}|^2 = |t|^2$). The curves are plotted for different values of the power transmission coefficient of the front mirror imposing $a_d^2 = 0.9$, $T_{RT} = 100$ ns and setting the phases of r_{12} and r_{21} to π and 0 respectively. We note that, for both the graphs, the spectral distribution is identical to that obtained in chapter 2 for the Fabry-Perot resonator, for all the values of $|t|^2$. A different scenario is found in Fig. 4.4c and 4.4d, where the power spectra are plotted in case of nonreciprocal coupling for different degrees of nonreciprocity of the front mirror ($|t_{12}|^2 - |t_{21}|^2$) imposing that $|t_{12}|^2 + |t_{21}|^2 = 1$ with $|t_{12}|^2 \geq |t_{21}|^2$. Here a slightly lower value (0.8) of a_d^2 has been used to better show the curves in the 3-D plot. The more evident difference can be seen in the power spectrum of the reflected field (Fig. 4.4d), in which the classical transmission dips turn into peaks with increasing the degree of nonreciprocity, meaning that more light is coupled in the cavity than what is reflected by the front mirror. We also note that the reflected power vanishes at the highest degree of nonreciprocity ($|t_{12}|^2 = 1, |t_{21}|^2 = 0$), since the light is completely trapped inside the resonator.

4.2.3 Theoretical analysis of the power balance

To study the effect of the nonreciprocal coupling on the energy trapping capability, an investigation on the power balance of the resonator is required. To do so, we calculated the total intra-cavity and reflected powers encased in one FSR. When normalized to the input power and the FSR, expressed in angular frequency ($\Delta\omega_{FSR} = 2\pi/T_{RT}$), they are given by the following expressions respectively:

$$G_{cav} = \frac{1}{\Delta\omega_{FSR}} \int_{FSR} \left| \frac{A(\omega)}{A_{in}(\omega)} \right|^2 d\omega \qquad G_R = \frac{1}{\Delta\omega_{FSR}} \int_{FSR} \left| \frac{A_R(\omega)}{A_{in}(\omega)} \right|^2 d\omega \qquad (4.11)$$

where the argument of the integral of G_{cav} is nothing else but the intra-cavity power enhancement. Therefore, G_{cav} represents the total power enhancement attained over one FSR.

First, we studied the problem focusing on a purely theoretical analysis, plotting the values of G_{cav} and G_R as a function of the in- and out-coupling transmittance. Figure 4.5a shows the case with $a_d^2 = 0.1$dB, $T_{RT} = 100$ns and the phases of r_{12} and r_{21} both set to 0. The red lines indicate the states where coupling is reciprocal ($|t_{12}|^2 = |t_{21}|^2$). The maximum value of G_{cav} occurs when $|t_{12}|^2 = 1$ and $|t_{21}|^2 = 0$ (top left corner of the plot), i.e. when there is total inwards transmission and zero outwards transmission through the front mirror. Conversely, when $|t_{12}|^2 = 0$, nothing enters the resonators and, as expected, $G_{cav} = 0$. More importantly, we note that, owing to the nonreciprocal coupling, the intra-cavity power can be enhanced by more than a factor of 40 with respect to the reciprocal case (red line). The graph of G_R shows an inverse behavior, with a peak value occurring at $|t_{12}|^2 = 0$, where the incoming power is totally reflected by the front mirror, while the minimum value is reached when $|t_{12}|^2 = 1$ and $|t_{21}|^2 = 0$

(top left corner of the plot), where the incoming power is fully coupled and totally dissipated within the resonator. The graphs in figures 4.5b and 4.5c show the result for 1 and 2 dB of internal (round-trip) loss, respectively. We can see that G_{cav} decreases with increasing internal loss for all combinations of $|t_{12}|^2$ and $|t_{21}|^2$, while the maximum value of G_{R} does not change because, in this case, the contribution of the out-coupled power, that is affected by the internal loss, is missing. We also note that G_{R} exhibits smoother variations as a function of $|t_{21}|^2$ when the contribution of the internal loss increases.

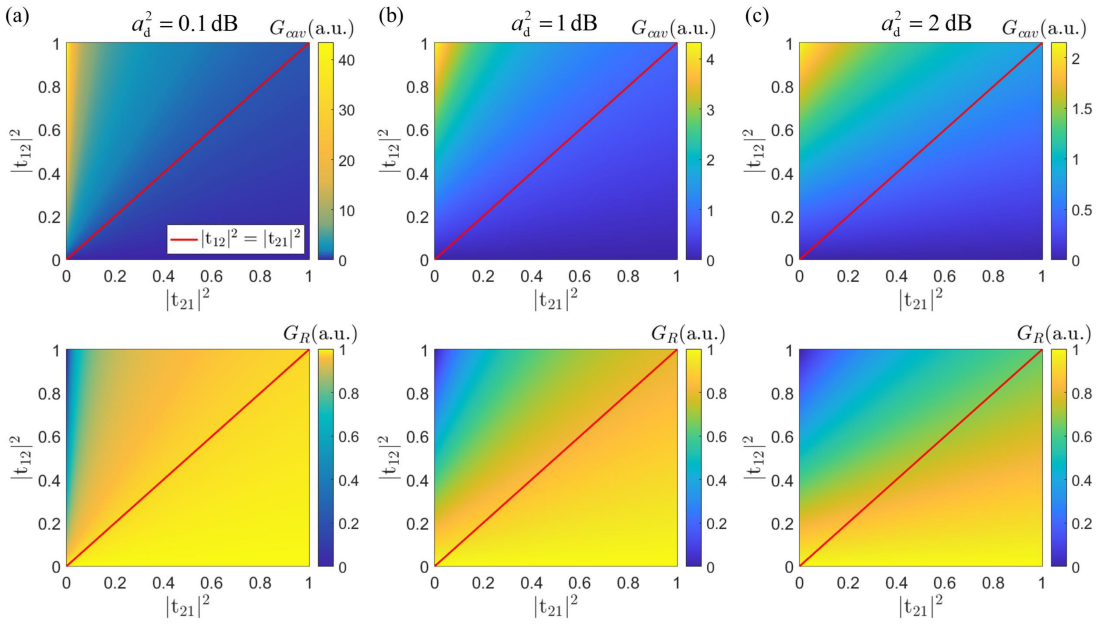

Figure 4.5 – Graphs in color scale of the total intra-cavity power enhancement (top row) and reflected (bottom row) power encased in one FSR, normalized to the input power and to $\Delta\omega_{\mathrm{FSR}}$, plotted as a function of the in- and out-coupling transmittance $|t_{12}|^2$ and $|t_{21}|^2$ respectively. The values are related to a resonator with (a) 0.1 dB, (b) 1 dB and (c) 2 dB of internal loss, while the red line indicates the points relative to the reciprocal coupling.

Overall this theoretical model shows a remarkable enhancement of the intra-cavity power in resonators with nonreciprocal coupling where $\rho_{\mathrm{in}} > \rho_{\mathrm{out}}$. The impact of this power enhancement, we will see in the next sections, can be quantified by the TBP, which then plays the role of a figure of merit for the energy coupling efficiency in all kind of resonant systems.

4.3 Validation of the theoretical model

To validate the theoretical analysis, we compared these results with those obtained from simulations based on a full-wave analysis conducted using the software VPIpho-

tonics (https://www.vpiphotonics.com). To induce the nonreciprocal coupling, we implemented the Gires-Tournois resonator in the form of a figure-9 cavity where the nonreciprocal front mirror is simulated by a time-modulated Sagnac interferometer.

4.3.1 Simulation setup

The setup used in the simulations is schematically shown in Fig. 4.6. As illustrated in the picture, such a particular configuration of the figure-9 resonator, can be seen as a GT resonator, in which the Sagnac interferometer represents the partially reflecting mirror whose reflection and transmission coefficients depend on the interference, occurring at the coupler, between the two counter-propagating waves in the loop. Using localized time-varying phase modulation asymmetrically positioned inside the Sagnac loop, allowed us to change in time the in-coupling/out-coupling transmission coefficients of the front mirror, which results in a dynamic control of the in- and out-coupling energy rates of the resonators. This can be explained by examining the equations that govern the wave interference at the coupler.

Let us consider an optical pulse incident on the R port of the coupler, whose pulse duration is smaller than the cavity round trip time. The nonreciprocity of the coupler imposes that the cross and straight coupling coefficients depend on the direction of the light wave. In particular, κ_{a} and τ_{a} are the cross and straight coupling coefficients respectively for the wave propagating from R or T port towards inside the loop, while κ_{b} and τ_{b} are the cross and straight coupling coefficients respectively for the wave going from inside the loop towards the R or T port. More specifically, the coupler is characterized by two distinct scattering matrices, one for each direction of propagation of the wave. We therefore can define $\mathbf{S}_{\mathrm{Ca}}$, the scattering matrix for the wave propagation towards the inside of the loop, and $\mathbf{S}_{\mathrm{Cb}}$ for the wave coming from within the loop:

$$\mathbf{S}_{\mathrm{Ca}} = \begin{bmatrix} \tau_{\mathrm{a}} & -j\kappa_{\mathrm{a}} \\ -j\kappa_{\mathrm{a}} & \tau_{\mathrm{a}} \end{bmatrix} \qquad \mathbf{S}_{\mathrm{Cb}} = \begin{bmatrix} \tau_{\mathrm{b}} & -j\kappa_{\mathrm{b}} \\ -j\kappa_{\mathrm{b}} & \tau_{\mathrm{b}} \end{bmatrix} \tag{4.12}$$

A device with such characteristic is included in the VPIphotonics software library as a generic coupler in which it is possible to arbitrarily set the scattering parameters. However, the same behavior can be performed in practice by a time-variant tunable directional coupler made of a 4-port Mach-Zehnder interferometer [27].

Passing through the coupler the incoming pulse is split in two smaller pulses whose complex amplitudes can be written as following:

$$A_{1\mathrm{a}} = \tau_{\mathrm{a}} A_{\mathrm{in}} \qquad A_{2\mathrm{a}} = -j\kappa_{\mathrm{a}} A_{\mathrm{in}} \tag{4.13}$$

where A_{in} is the original complex amplitude of the pulse. If there is no phase modulation the complex amplitudes of the two counter-propagating waves are simply:

$$A_{\mathrm{cw}} = \tau_{\mathrm{a}} A_{\mathrm{in}} e^{-j\phi_{\mathrm{p}}} \qquad A_{\mathrm{ccw}} = -j\kappa_{\mathrm{a}} A_{\mathrm{in}} e^{-j\phi_{\mathrm{p}}} \tag{4.14}$$

where ϕ_{p} is the phase delay acquired by the optical pulse through the fiber loop.

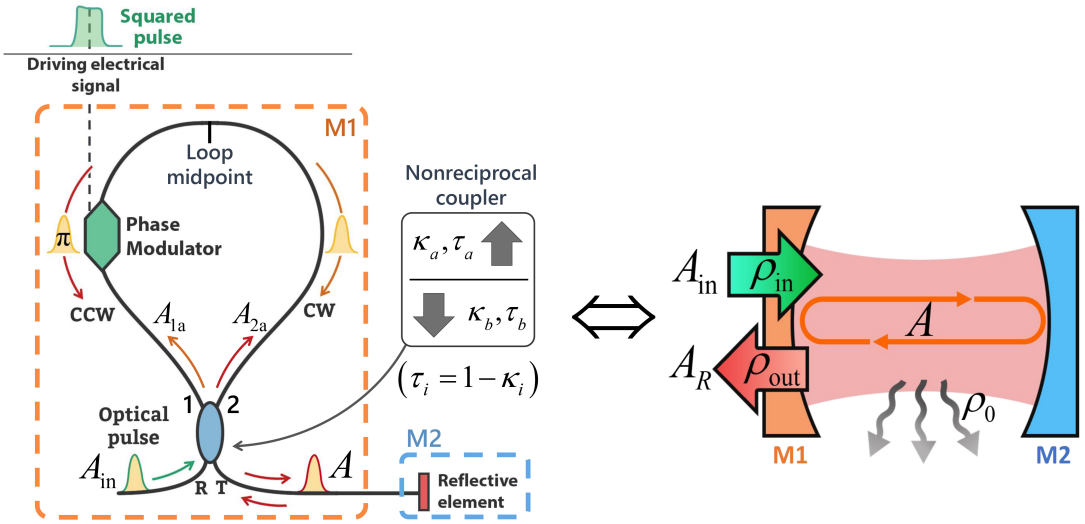

Figure 4.6 – Schematic representation of the setup used in VPIphotonics for the numerical simulations. The phase modulation in combination with the nonreciprocal coupler both integrated in a Sagnac interferometer ensures a total control of the transmission coefficient of the fiber loop, allowing to emulate the nonreciprocal front mirror of the Gires-Tournois resonator.

Then, by denoting A_{T} and A_{R} the complex amplitudes of the transmitted and reflected portions of the pulse respectively, the field transmission and reflection coefficients t_0 and r_0, respectively, are easily found:

$$A_{\mathrm{T}} = \tau_{\mathrm{b}} A_{\mathrm{cw}} - j\kappa_{\mathrm{b}} A_{\mathrm{ccw}} \Rightarrow \mathrm{t}_0 = \frac{A_{\mathrm{T}}}{A_{\mathrm{in}}} = \left(\tau_{\mathrm{a}}\tau_{\mathrm{b}} - \kappa_{\mathrm{a}}\kappa_{\mathrm{b}}\right) e^{-j\phi_{\mathrm{p}}} \tag{4.15}$$

$$A_{\mathrm{R}} = -j\kappa_{\mathrm{b}} A_{\mathrm{cw}} + \tau_{\mathrm{b}} A_{\mathrm{ccw}} \Rightarrow \mathrm{r}_0 = \frac{A_{\mathrm{R}}}{A_{\mathrm{in}}} = -j\left(\tau_{\mathrm{a}}\kappa_{\mathrm{b}} + \kappa_{\mathrm{a}}\tau_{\mathrm{b}}\right) e^{-j\phi_{\mathrm{p}}} \tag{4.16}$$

where the subscript 0 indicates the absence of the phase modulation. Conversely, if the phase modulator is electrically gated to shift by π the phase of one of the two counter-propagating pulses only, say the CCW pulse, the complex amplitude A_{ccw} in Eq. 4.14 becomes:

$$A_{\mathrm{cw}} = \tau_{\mathrm{a}} A_{\mathrm{in}} e^{-j\phi_{\mathrm{p}}} \qquad A_{\mathrm{ccw}} = -j\kappa_{\mathrm{a}} A_{\mathrm{in}} e^{-j(\phi_{\mathrm{p}}+\pi)} = j\kappa_{\mathrm{a}} A_{\mathrm{in}} e^{-j\phi_{\mathrm{p}}} \tag{4.17}$$

and therefore, the complex transmission and reflection coefficients exhibited by the

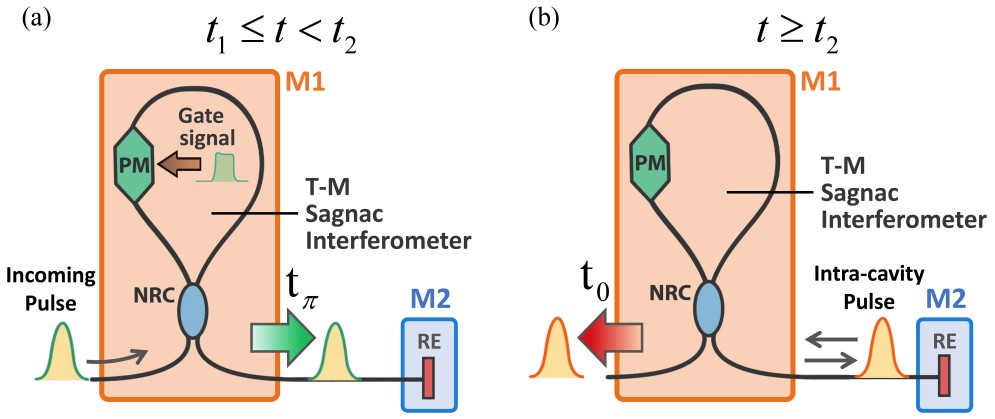

Figure 4.7 – Schematic representation of the GT resonator in the form of a figure-9 cavity during the process of (a) in-coupling $t_1 \leq t < t_2$ and (b) out-coupling of energy $t \geq t_2$. PM: phase modulator; NRC: nonreciprocal coupler; RE: reflective element.

Sagnac interferometer will be:

$$\mathrm{t}_\pi = (\tau_\mathrm{a}\tau_\mathrm{b} + \kappa_\mathrm{a}\kappa_\mathrm{b})\, e^{-j\phi_\mathrm{p}} \tag{4.18}$$

$$\mathrm{r}_\pi = -j\,(\tau_\mathrm{a}\kappa_\mathrm{b} - \kappa_\mathrm{a}\tau_\mathrm{b})\, e^{-j\phi_\mathrm{p}} \tag{4.19}$$

where the subscript π indicates the presence of the π phase shift imparted by the phase modulator. In the above expressions and in equations 4.15 and 4.16 the value of ϕ_p can be arbitrarily set to 0 without loss of generality.

When the electrical signal is applied at the phase modulator at a time t_1, and for a duration $t_1 \leq t < t_2$, the Sagnac interferometer exhibits a transmission coefficient $\mathrm{t}(t_1) = \mathrm{t}_\pi$, while for the rest of the time ($t \geq t_2$), the transmission coefficient is $\mathrm{t}(t_2) = \mathrm{t}_0$. Therefore, the localized time-varying phase modulation in combination with the non-reciprocal coupler allowed to arbitrarily vary in time the power transmission coefficient t of the Sagnac interferometer. The final result is two effective different coupling energy rates of the figure-9 resonator, one for $t_1 \leq t < t_2$ and one for $t \geq t_2$ which are given respectively by:

$$\rho(t_1) = \frac{|\mathrm{t}_\pi|^2}{T_\mathrm{RT}} \qquad \rho(t_2) = \frac{|\mathrm{t}_0|^2}{T_\mathrm{RT}} \tag{4.20}$$

If the incoming optical pulse is synchronized with the electric signal, it is coupled in the resonator through the Sagnac interferometer with a power transmission coefficient $|\mathrm{t}_\pi|^2$, as it is depicted in Fig. 4.7a. However, while it resonates within the cavity, it is coupled out with a power transmission coefficient $|\mathrm{t}_0|^2$ (Fig. 4.7b). Doing so, although the Sagnac interferometer exhibits a unique transmission coefficient at any given time, the incoming pulse experiences a transmission coefficient that is different from the

one experienced by the intra-cavity pulse ($t_\pi \neq t_0$). We can therefore identify t_π and t_0 with the transmission coefficients t_{12} and t_{21}, respectively, and $\rho(t_1)$ ($\rho(t_2)$) with the in-coupling (out-coupling) energy rate ρ_{in} (ρ_{out}) of the theoretical model of the Gires-Tournois resonator. Analogously, we identify r_π and r_0 with the reflection coefficients r_{12} and r_{21} respectively. In such a system, the acceptance bandwidth corresponds to the bandwidth that the figure-9 resonator exhibits in the time window between t_1 and t_2, that is $\Delta\omega_{\text{acc}} = \rho(t_1) + \rho_0$, while the cavity bandwidth is the bandwidth that the system exhibits when there is no signal applied to the phase modulator (i.e. for $t \geq t_2$), which is given by $\Delta\omega_{\text{cav}} = \rho(t_2) + \rho_0$.

Table 4.1 – Table summarizing the correspondences between the parameters of the VPIphotonics simulative setup and those of the GT resonator model.

VPIphotonics simulation setup	GT resonator model
$t_\pi = (\tau_a\tau_b + \kappa_a\kappa_b)\, e^{-j\phi_p}$	t_{12}
$t_0 = (\tau_a\tau_b - \kappa_a\kappa_b)\, e^{-j\phi_p}$	t_{21}
$r_\pi = -j\,(\tau_a\kappa_b - \kappa_a\tau_b)\, e^{-j\phi_p}$	r_{12}
$r_0 = -j\,(\tau_a\kappa_b + \kappa_a\tau_b)\, e^{-j\phi_p}$	r_{21}
$\rho(t_1) = \lvert t_\pi\rvert^2/T_{\text{RT}}$	ρ_{in}
$\rho(t_2) = \lvert t_0\rvert^2/T_{\text{RT}}$	ρ_{out}

Therefore, in such a system the nonreciprocity property of the coupling junction, represented by the time-modulated Sagnac interferometer, is induced by breaking its time-invariance, that is, by changing in time the transmission coefficient of the front mirror in the two directions. Nonetheless, this methods ensures the conservation of energy since, the time-variant Sagnac interferometer exhibits always the same scattering parameters at any given time, meaning that $t_{12}(t) = t_{21}(t)$ and $r_{12}(t) = r_{21}(t)$ for any t. In mathematical terms this is confirmed by the fact that the scattering matrix of the front mirror at any time fulfills the condition of unitary matrix that we have seen in Eq. 2.4.

It should be noticed that this time-variant nature of the nonreciprocal coupling prevents this method to be used for storing signals in time-invariant structures. Specifically, a linear and time-invariant system made of a closed cavity with a coupling interface, cannot exhibit a nonreciprocal behavior, due to the considerations on energy conservation described above. However, other approaches that involve *open* resonant systems, such as the one proposed in [49], can be well described by using the theory presented in the previous section.

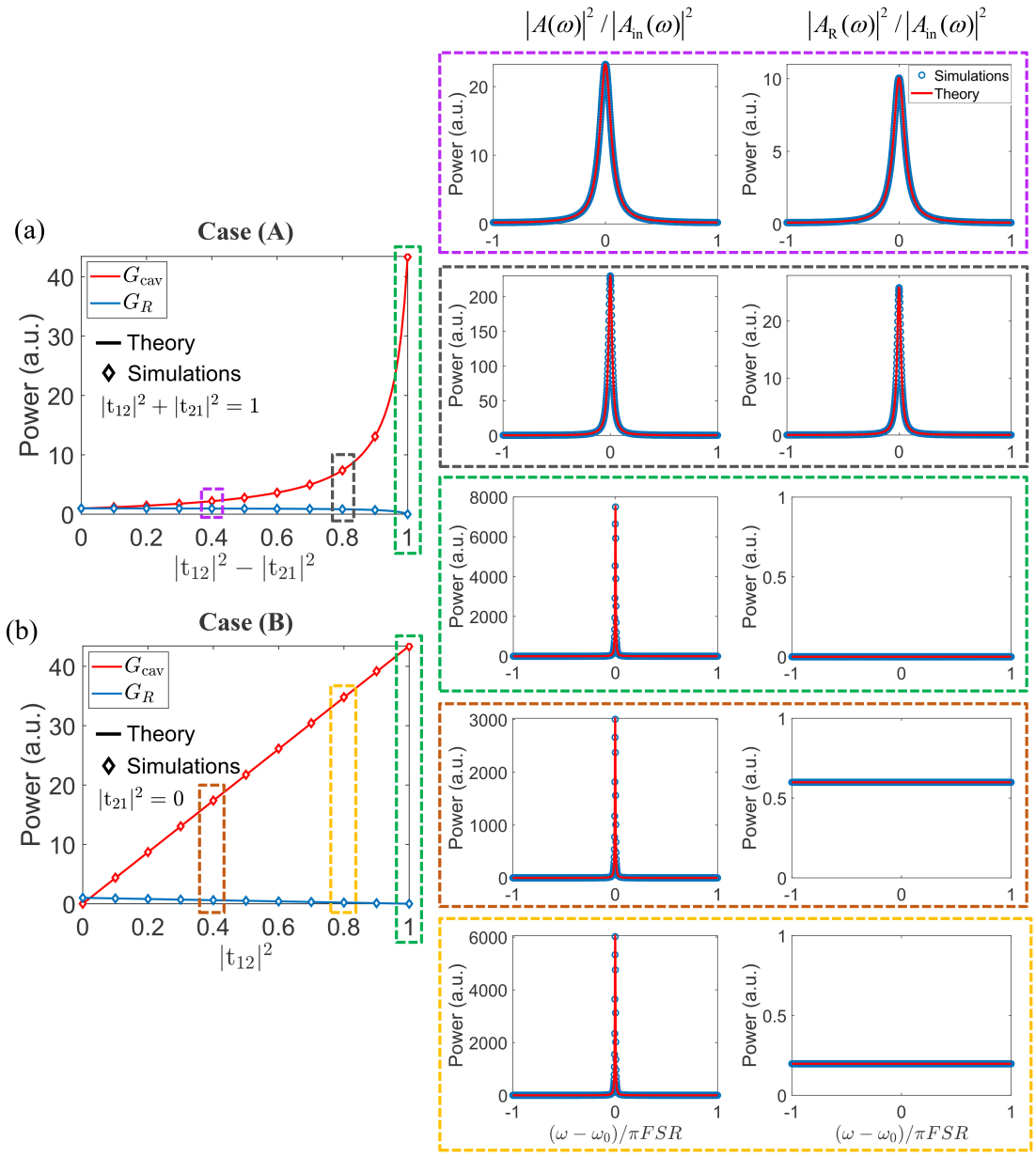

Figure 4.8 – Left-hand side: comparison of the values obtained from the simulations with those retrieved from equations 4.11 of the total power enhancement and reflected power, encased in one FSR and normalized to it. The graphs are related to (a) case (A) and (b) case (B) and plotted as a function of the degree of nonreciprocity and the in-coupling transmittance respectively. Right-hand side: spectral distribution over one FSR of the intra-cavity power enhancement and the reflected power. The curves are related to a degree of nonreciprocity equal to 0.4 (violet-dashed panel), 0.8 (black-dashed panel) and 1 (green-dashed panel) for the case (A), and to 0.4 (brown-dashed panel) and 0.8 (yellow-dashed panel) for the case (B).

4.3.2 Results of the simulations and comparison with the theoretical model

Through this numerical model, we could arbitrarily and independently vary the in- and out-coupling transmission coefficients of the front mirror. However, for the sake of clarity, we analyzed the system for two different cases. As the degree of nonreciprocity is equivalent to the minimum distance from the line of reciprocity for any point in the parameter space considered in Fig. 4.5, in case (A) we evaluate the spectral response of the system for different degrees of nonreciprocity by considering points meeting the conditions: $|t_{12}|^2 + |t_{21}|^2 = 1$ and $|t_{12}|^2 \geq |t_{21}|^2$; in case (B), aiming at investigating on the behavior of the resonator in the situation where the light is totally trapped in the cavity, we performed the analysis for $|t_{21}|^2 = 0$ while varying $|t_{12}|^2$. In both cases a_{d}^2 and T_{RT} are set to 0.1 dB and 100 ns respectively, while the phases of r_{12} and r_{21}, were retrieved by equations 4.19 and 4.16 respectively. For all the simulations performed in this theoretical work, a 500 ps-long Gaussian pulse was used.

The results for case (A) are shown in Fig. 4.8a. We can see that G_{cav} and G_{R} have roughly the same value in the reciprocal case, given that the internal loss is small. However, by decoupling $|t_{12}|^2$ from $|t_{21}|^2$, G_{cav} exponentially grows with increasing degree of nonreciprocity, taking its maximum value at the highest degree of nonreciprocity, while G_{R} decreases. A rather different scenario occurs in the case (B) described in Fig. 4.8b, where both G_{cav} and G_{R} vary linearly with $|t_{12}|^2$. In this case, since $|t_{21}|^2$ is set to 0, G_{R} is a linear function of the reflection coefficient of the front mirror and no cavity resonant mode is coupled out, while the growth of G_{cav} is due only to the in-coupling energy rate ρ_{in}, as predicted by Eq. 4.9 and Eq. 4.10 respectively. In fact, in the extreme case where also $|t_{12}|^2 = 0$, then $G_{\mathrm{cav}} = 0$, while G_{R} has a finite value since the incoming power is totally reflected by the front mirror. The right-hand side of the figure shows the spectral distribution over one FSR of the intra-cavity power enhancement and the normalized reflected power related to some values of Figs. 4.8a and 4.8b. As expected, the bandwidth of the intra-cavity spectrum, which is given by:

$$\Delta\omega = \frac{4}{T_{\mathrm{RT}}} \sin^{-1}\left[\frac{1 - |r_{21}|a_{\mathrm{d}}}{2\sqrt{(|r_{21}|a_{\mathrm{d}})}}\right] \tag{4.21}$$

gets narrower with increasing degree of nonreciprocity since $|t_{21}|^2$, (which is equal to $1 - |r_{21}|^2$), decreases. We also note that the zero out-coupling transmission ($|t_{21}|^2 = 0$, green-, brawn- and yellow-dashed panels) leads to a reflection spectrum that is no longer dependent on the frequency, since it includes only the contribution of the power reflected by the front mirror. Particularly, in the specific case of fully coupled input power ($|t_{12}|^2 = 1$, i.e. – maximum degree of nonreciprocity, green-dashed panel), the reflected power is null, meaning that the light is completely trapped inside the resonator, and dissipated via the internal loss. Importantly, in both cases, (A) and (B), the numerical results are in a good agreement with equations 4.9, 4.10 and 4.11. Therefore, the decoupling of the in- and out-coupling energy rates in a resonant system,

as a consequence of the induced nonreciprocity, can dramatically affect the balance between the reflected and intra-cavity power and significantly improve the power enhancement provided by the resonator.

4.4 Evaluation of the time-bandwidth performance

Following the above analysis, we evaluated the TBP for different degrees of nonreciprocity. We have seen in chapter 2 that the resonator losses, which include both the radiative and non-radiative out-coupling energy rates, are quantified by the linewidth of the Lorentzian profile of the single resonant mode and not by the full-width-at-half-maximum (FWHM) of the Airy function characteristic of the resonator spectral response. This is a rule that is valid regardless the strength of the coupling. Therefore, to properly derive the TBP, we used the TCMT to retrieve the Lorentzian mode profile associated to the loading and decay processes of the resonator.

We calculated the TBP of the resonator in the case of reciprocal and nonreciprocal coupling, and we plotted the values in Fig. 4.9a as a function of $|t_{12}|^2$. For the nonreciprocal case, we plotted three curves corresponding to three values of the absorption loss a_d^2: 0.1, 1 and 2 dB, while $|t_{21}|^2$ was set to 0.1. Owing to the decoupling of the in- and out-coupling energy rates, the TBP linearly increases with the increasing of $|t_{12}|^2$ in case of nonreciprocal coupling, while it is always equal to 1 in case of reciprocal coupling.

In Fig. 4.9b, 4.9c and 4.9d the TBP of a resonator with $a_d^2 = 0.1\,\text{dB}$, $1\,\text{dB}$ and $2\,\text{dB}$ is plotted for all the combinations of $|t_{12}|^2$ and $|t_{21}|^2$, with the red line indicating reciprocal coupling ($|t_{12}|^2 = |t_{21}|^2$), where the TBP turns into the TBL. We note that the highest TBP occurs at the maximum degree of nonreciprocity, while it becomes smaller than 1 when the degree of nonreciprocity is negative ($|t_{12}|^2 < |t_{21}|^2$). It is interesting to note that the values of the TBP follow those of G_{cav} in Fig. 4.5 showing a strict correlation between the TBP and the total power enhancement attained over one FSR. In fact, both show their peak at the maximum degree of nonreciprocity. However, while G_{cav} is always null when $|t_{12}|^2 = 0$, the TBP is greater than zero (and smaller than 1) because $\rho_0 \neq 0$, and decreases with increasing $|t_{21}|^2$ along the line $|t_{12}|^2 = 0$, reaching its minimum at $|t_{21}|^2 = 1$. This is also visible in Fig. 4.9b and 4.9c where the highest and lowest value of the TBP get close to each other given a larger value of the internal loss.

The benefit of the nonreciprocal coupling in a resonant system shows up more clearly by evaluating the total power enhancement in the nonreciprocal case with respect to the power enhancement achievable in the reciprocal case for the same amount of in-coupled power. This can be illustrated by plotting G_{cav}^{NR}/G_{cav}^{R}, where G_{cav}^{NR} is G_{cav} for the nonreciprocal system calculated with $\rho_{in} > \rho_{out}$, and G_{cav}^{R} for the reciprocal

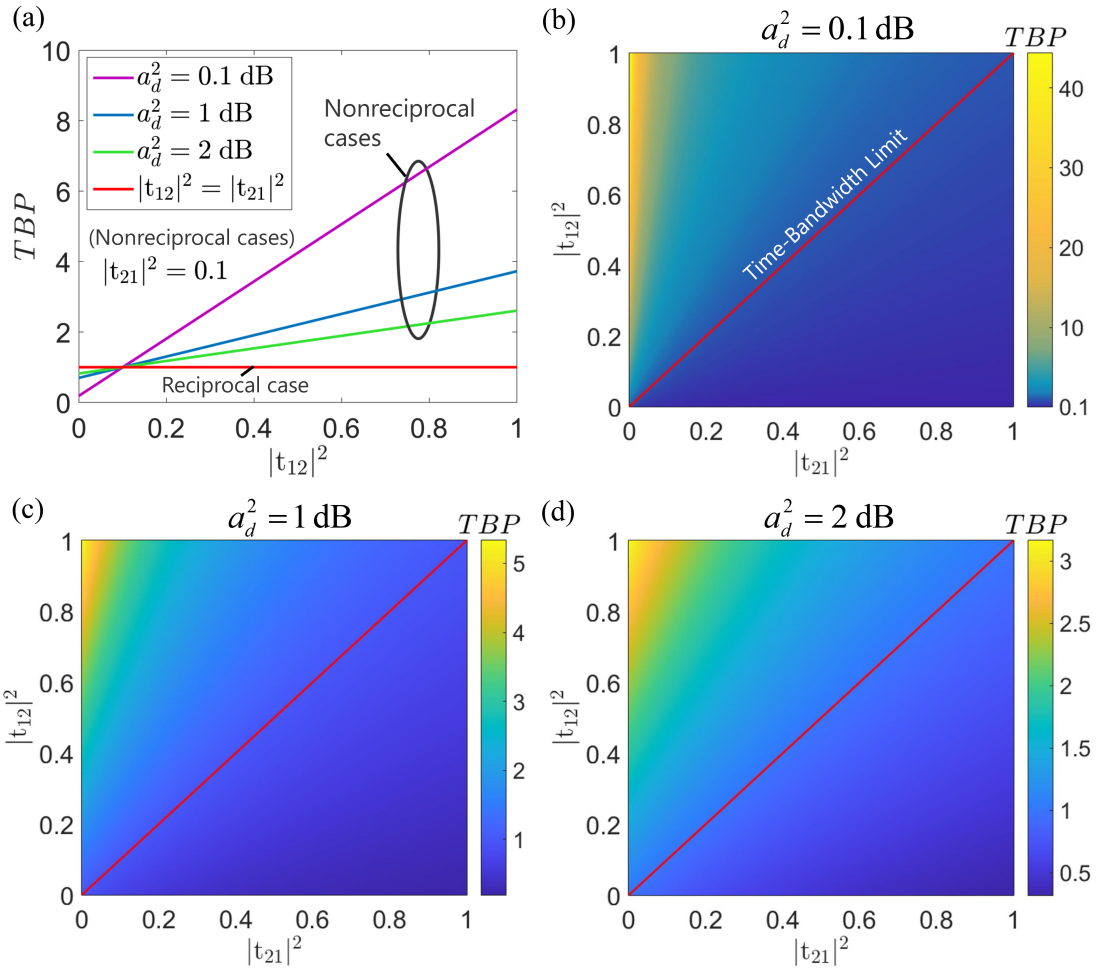

Figure 4.9 – (a) Comparison between the TBP of a reciprocal and a nonreciprocal resonator plotted as a function of the in-coupling transmittance. The curves of the nonreciprocal cases are relative to resonators with different absorption losses. (b), (c) and (d): graphs of the TBP in color scale as a function of the in- and out-coupling transmittance for a resonator with 0.1, 1 and 2 dB of internal loss respectively. The red line indicates the values relative to the reciprocal coupling (i.e. TBP = 1), which corresponds to the TBL.

system. The results, obtained from the simulations, are plotted in Fig. 4.10 as a function of the degree of nonreciprocity (with the same conditions of Case (A) in Fig. 4.8) and compared with the corresponding values of the TBP. Clearly, the ratio $G_{\mathrm{cav}}^{\mathrm{NR}}/G_{\mathrm{cav}}^{\mathrm{R}}$ increases exponentially with the degree of nonreciprocity, proving that by tailoring the decoupling of ρ_{in} and ρ_{out}, the intra-cavity power can be enhanced much more than what could be done with a reciprocal resonator. We also note that the values of the TBP are in good agreement with those of $G_{\mathrm{cav}}^{\mathrm{NR}}/G_{\mathrm{cav}}^{\mathrm{R}}$, meaning that it can be used as a figure of merit to indicate the gain of total power enhancement due to nonreciprocal coupling, with respect to a reciprocal resonator, for an equal amount

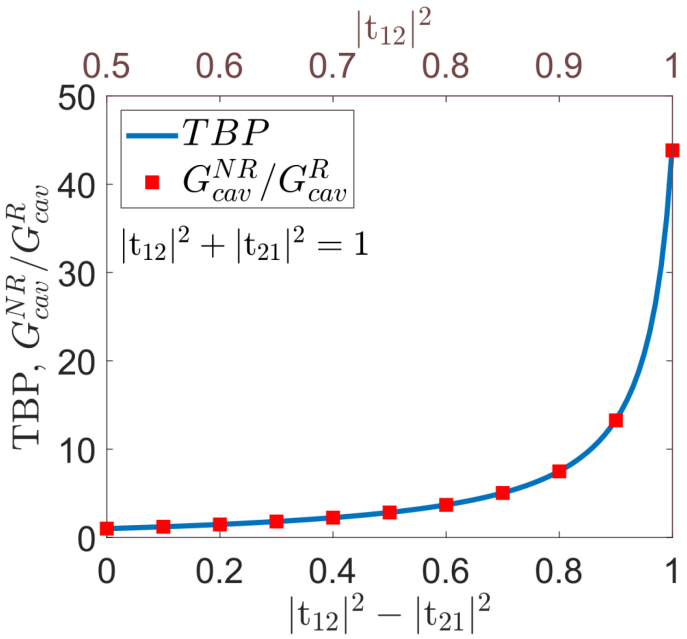

Figure 4.10 – Comparison between the values of the ratio $G^{\mathrm{NR}}_{\mathrm{cav}}/G^{\mathrm{R}}_{\mathrm{cav}}$ calculated using the values of G_{cav} obtained from the simulations, and the TBP as a function of the degree of nonreciprocity of the system (bottom horizontal axis) and the in-coupling transmittance (top horizontal axis).

of in-coupled power. Such a parameter may have a fundamental role specially in nonlinear optics applications, where the large build-up of light intensity contributes to the enhancement of the nonlinear optical effects.

4.5 Summary

In this chapter we explored the possibility to overcome the fundamental TBL that characterizes all resonant systems, by implementing a nonreciprocal interface as a coupling junction.
The chapter started by introducing the general definition of the TBP for a resonant system. Here, the concept of the acceptance bandwidth has been distinguished from the more common cavity bandwidth, which is simply the inverse of the cavity photon life-time. The acceptance bandwidth, in fact, identifies, through its association with the energy loading rate, how fast the intra-cavity energy would exponentially grow if the resonator was 'fed' through a time-reversed version of the decay process. In reciprocal resonators there is no reason to make this distinction since the two bandwidths coincide and the TBP takes the value of 1, that is referred to the TBL. In such resonators a long storage time, which can be achieved only through a reduction of the losses, inevitably implies a narrowing of the bandwidth of the Lorentzian resonance

mode of the system. On the other hand, in resonators with nonreciprocal coupling the in-coupling energy rate can be decoupled from the cavity bandwidth and can be increased at will to obtain an arbitrarily large TBP. However, this can be possible only through the breaking of one of two fundamental properties that characterizes most ordinary resonant systems: linearity or time-invariance.

To obtain a measure of the increased storage time offered by resonant systems with a TBP > 1, we expressed the TBP in terms of acceptance and cavity Lorentzian finesse. This provided us a new insight of the TBP as a measure of the increased delay/storage time imparted to a light wave, with respect to what the bandwidth of the resonant structure would allow to the same amount of in-coupled power.

We then investigated the implications of the nonreciprocal energy coupling on the TBP and the power balance of a generic resonant cavity modeled as a GT resonator. The results, obtained performing a theoretical and numerical analysis of the intra-cavity power enhancement and the total reflected power, showed that the decoupling of the in- and out-coupling energy rates, can effectively overcome the TBL, reporting a value of the TBP that is more than 40 times above this limit for the specific value of loss used. The model was based on the derivation of the frequency response of the GT resonator, using the PCF, while the evaluation of the TBP was performed based on the definition given at the beginning of the chapter. Finally, by comparing the total power enhancement in the reciprocal and nonreciprocal case, we have seen that the TBP can be used a figure of merit that characterizes the gap between the total power enhancement attained over one FSR with the nonreciprocal coupling from that achievable in the reciprocal case considering the same amount of in-coupled power.

5 Arbitrarily high time-bandwidth performance in a nonreciprocal optical resonator with broken time-invariance

The theoretical work illustrated in the previous chapter showed that, although the time-bandwidth limit (TBL) is a fundamental rule that arises from basic Fourier reciprocity, it can be overcome, under certain conditions, by decoupling the rate of in-coupling energy from the bandwidth of the cavity resonant mode. However, despite several techniques based on slow-light waveguides and temporal adiabatic tuning of resonant structures [12, 40, 43, 110, 111] have previously been investigated with the purpose of demonstrating a time-bandwidth-unlimited resonator, their inherent limitations have so far prevented them from successfully achieving this goal.

In this chapter I will show that a resonant system like the one modeled in the previous chapter can be implemented using a simple macroscopic, fiber-optic resonator where the nonreciprocity is induced by breaking its time-invariance. During the experiments the resonator is switched from a completely open to a completely closed state by means of a spatially asymmetric time-varying phase modulation. Unlike previous adiabatic cavity modulation schemes [43, 111], the measurements are conducted in a *non-adiabatic* regime, so that the retrieved pulses exiting the resonator do not exhibit detectable temporal nor spectral distortions. The experimental results I will show report a TBP 30 times above the fundamental time-bandwidth limit. However, we will see that, in general, the TBP of an individual resonator with such characteristics is ultimately limited only by the Lorentzian cavity finesse and can be increased at will above the limit, provided that internal, dissipative losses are kept sufficiently low.

5.1 The figure-9 resonator with broken time-invariance[1]

To experimentally prove that overcoming the TBL is truly possible by using a resonant system with a nonreciprocal coupling, we implemented such a system, at telecommunication wavelength (around 1550 nm), by building a figure-9 resonator similar to that used for the simulations conducted with VPIphotonics software. We performed the experiments on this simple known fiber configuration, similar in some ways to a recirculating fiber loop [112], to demonstrate for the first time a corroboration of the theory that a resonant system with a nonreciprocal coupling can exhibit an arbitrarily high TBP. The resonator was made of polarization maintaining fibers with a T_{RT} of about 48 ns, while the reflective element is a fiber Bragg grating with a center wavelength at 1551.3 nm and a stop bandwidth of about 28.2 GHz. To mimic the nonreciprocal mirror we break the time-invariance by using localized time-varying phase modulation asymmetrically positioned inside the Sagnac interferometer, as already explained in details in section 4.3. The pulse length specially chosen to be shorter than the distance between the phase modulator and the center of the Sagnac loop, allowed to apply the phase shift to only one of the two counter-propagating pulses. The Sagnac interferometer was built using a 50/50 standard directional coupler, instead of a nonreciprocal coupler. By developing the equations that govern the wave interference at the coupler as we did in section 4.3 and, imposing $\tau_{\mathrm{a}} = \tau_{\mathrm{b}}$ and $\kappa_{\mathrm{a}} = \kappa_{\mathrm{b}}$, we find that the complex transmission coefficients exhibited by the Sagnac interferometer, with and without the presence of the π phase shift, are given by the following expressions:

$$\mathrm{t}_{\pi} = \tau^2\sqrt{a_{\mathrm{p}}}e^{-j\phi_{\mathrm{p}}} - \kappa^2\sqrt{a_{\mathrm{p}}}e^{-j\phi_{\mathrm{p}}}e^{j\pi} = (\tau^2+\kappa^2)\sqrt{a_{\mathrm{p}}}e^{-j\phi_{\mathrm{p}}} = \sqrt{a_{\mathrm{p}}}e^{-j\phi_{\mathrm{p}}} \tag{5.1}$$

$$\mathrm{t}_{0} = \tau^2\sqrt{a_{\mathrm{p}}}e^{-j\phi_{\mathrm{p}}} - \kappa^2\sqrt{a_{\mathrm{p}}}e^{-j\phi_{\mathrm{p}}} = (\tau^2-\kappa^2)\sqrt{a_{\mathrm{p}}}e^{-j\phi_{\mathrm{p}}} \tag{5.2}$$

where we have assumed an ideal coupler ($\tau^2+\kappa^2=1$), while the complex reflection coefficients are:

$$\mathrm{r}_{\pi} = -j\kappa\tau\sqrt{a_{\mathrm{p}}}e^{-j\phi_{\mathrm{p}}} - j\kappa\tau\sqrt{a_{\mathrm{p}}}e^{-j\phi_{\mathrm{p}}}e^{j\pi} = 0 \tag{5.3}$$

$$\mathrm{r}_{0} = -j\kappa\tau\sqrt{a_{\mathrm{p}}}e^{-j\phi_{\mathrm{p}}} - j\kappa\tau\sqrt{a_{\mathrm{p}}}e^{-j\phi_{\mathrm{p}}} = -j2\kappa\tau\sqrt{a_{\mathrm{p}}}e^{-j\phi_{\mathrm{p}}} \tag{5.4}$$

In the above expressions a_{p} is the field attenuation factor that accounts for the losses in the Sagnac interferometer. Then, taking the modulus square and inserting the

[1] The results of this section are partially adapted from the article: I. Cardea et al., Arbitrarily high time bandwidth performance in a nonreciprocal optical resonator with broken time invariance *Sci. Rep.* 10, 15752 (2020).

coefficients values for the 50/50 coupler ($|\tau|^2 = |\kappa|^2 = 1/2$), we obtain:

$$|\mathrm{t}_\pi|^2 = a_\mathrm{p} \qquad |\mathrm{r}_\pi|^2 = 0 \tag{5.5}$$

$$|\mathrm{t}_0|^2 = 0 \qquad |\mathrm{r}_0|^2 = a_\mathrm{p} \tag{5.6}$$

Therefore, a light pulse incident to the R port of the 50/50 coupler is split in two identical (in amplitude) portion. When the phase modulator is electrically gated, through an electrical squared pulse (of appropriate amplitude and duration at least equal to the one of the optical pulse), to shift by π the phase of the CCW pulse, a perfect constructive interference at the T port occurs. This interference is independent of the coupling coefficient of the coupler, as we can see from Eq. 5.1[2], leading to a full in-coupling transmittance. As a result, during the modulator gating time, say $t_1 \leq t < t_2$, the system is a *completely open cavity* capable of fully accepting the light without any reflection, so that the incident pulse is totally transmitted (and partially attenuated) through the Sagnac interferometer, experiencing the power coefficients of the cavity given in Eq. 5.5. This case is depicted in Fig. 5.1b. The pulse switched to the port T of the Sagnac interferometer is reflected by the FBG and travels again through the fiber loop mirror. At this point, no other phase shift is applied and the pulse bounces back and forth between the fiber loop and the FBG until it is extracted after a desired number of round trips (RTs) applying a second electrical "gate". During this time ($t \geq t_2$), the system acts as a *completely closed cavity* formed by the Sagnac interferometer and the reflective element (Fig. 5.1c), and the power coefficients seen by the pulse already stored in the resonator are those of Eq. 5.6. The corresponding energy loading and decay curves, with their associated Lorentzian profiles, that the system exhibits during the open and closed state respectively, are illustrated in Fig. 5.1a. After a desired number of cavity round-trip, we can extract the pulses from the resonator by gating once again the phase modulator (for $t_3 \leq t < t_4$), leading to switch the constructive interference to the R port, as illustrated in Fig. 5.1d. In this case, the power coefficients experienced by the pulse are again those of the open cavity. The pulse train is designed such that a given pulse coupled into the cavity does not overlap, inside the phase modulator, with the subsequent pulse.

It is important to note that during each stage of operation, i.e. injection, storing and release, the system is reciprocal and therefore the acceptance bandwidth coincides with the cavity bandwidth. However, the breaking of time-invariance renders the system nonreciprocal [50], since the system exhibits two different bandwidths during the injection and the storing stages.

[2] we found the same result in the vectorial model of the figure-9 laser treated in section 3.1.2

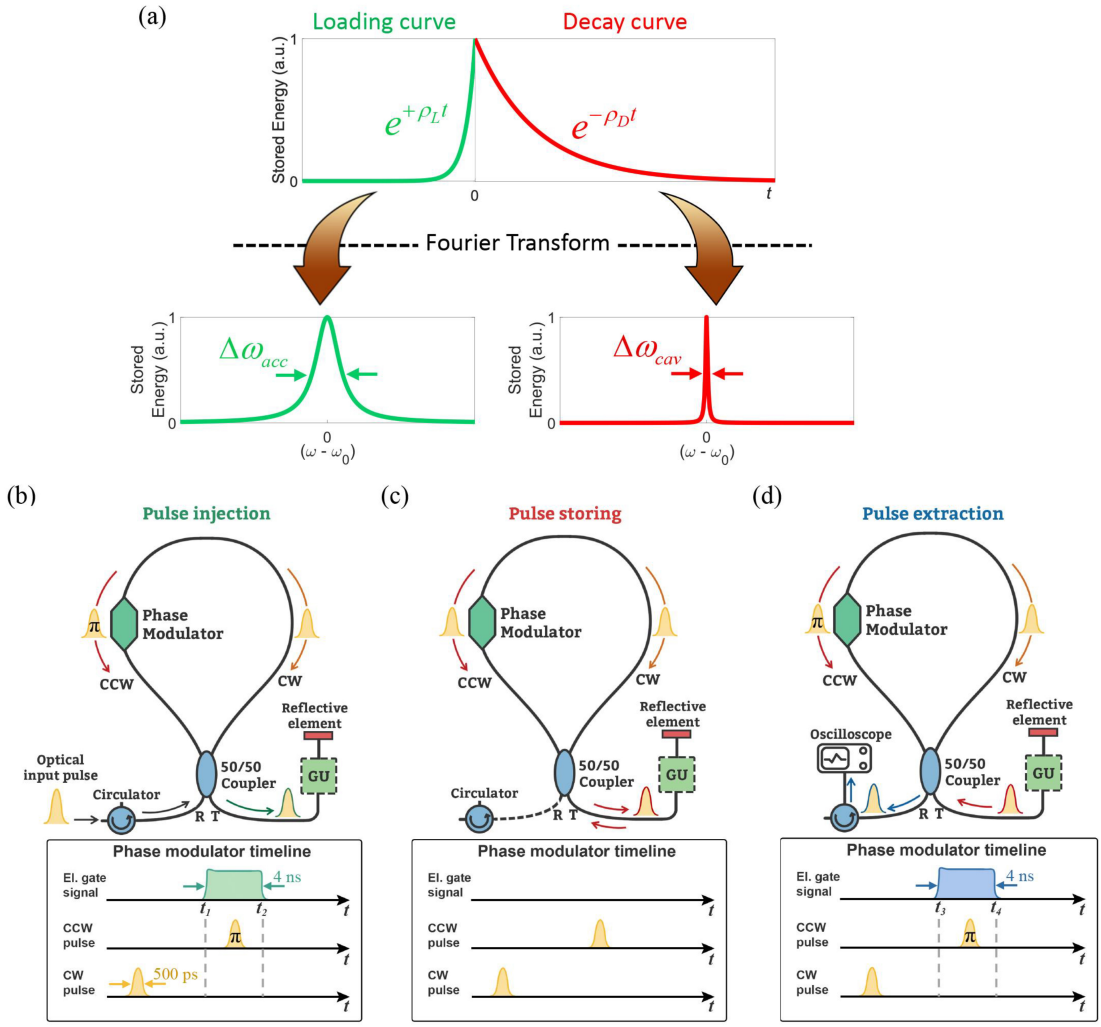

Figure 5.1 – (a) Exponential loading and decay curves of a time-variant nonreciprocal resonator. If $\rho_L > \rho_D$, the exponential energy loading process is faster than the decay process, and their associated bandwidths, $\Delta\omega_{acc}$ and $\Delta\omega_{cav}$, respectively, are different, with $\Delta\omega_{acc} > \Delta\omega_{cav}$. Implementation in a Figure-9 resonator: (b) Injection - The optical input pulse is fully coupled in the cavity owing to constructive interference of the CW and CCW pulses at the T port when a π phase shift is solely applied to the CCW pulse. (c) Storing - Once loaded, if no other gate signal is applied to the modulator, the CW and CCW pulses interfere constructively at the T port and the pulse is stored in the resonator until it is dissipated through internal loss. (d) Extraction - The pulse is extracted after a desired number of RTs by opening again the cavity, i.e. applying a second "gate" signal to the phase modulator to the CCW portion of the pulse. A gain unit (GU), can be incorporated to partially compensate for the dissipative loss.

To express the TBP as a function of the parameters that characterize the figure-9 resonator, we need to derive its in- and out-coupling energy rates in the case of fully

open and fully closed cavity state. Recalling the relations in Eq. 4.20 we can write:

$$\rho_{\text{in}} = \rho(t_1) = \frac{|\mathrm{t}_\pi|^2}{T_{\text{RT}}} = \frac{|\mathrm{t}_{12}|^2}{T_{\text{RT}}} = \frac{(\tau^2+\kappa^2)^2 a_{\text{p}}}{T_{\text{RT}}} = \frac{a_{\text{p}}}{T_{\text{RT}}} \tag{5.7}$$

$$\rho_{\text{out}} = \rho(t_2) = \frac{|\mathrm{t}_0|^2}{T_{\text{RT}}} = \frac{|\mathrm{t}_{21}|^2}{T_{\text{RT}}} = \frac{(\tau^2-\kappa^2)^2 a_{\text{p}}}{T_{\text{RT}}} = 0 \tag{5.8}$$

where we have identified t_π and t_0 with the transmission coefficients t_{12} and t_{21}, respectively, of the numerical model of the GT resonator.

In the numerical model of the GT resonator described in the previous chapter, we assumed a lossless nonreciprocal mirror. The Sagnac interferometer used in the experiments, however, exhibited some absorption loss which are taken into account by the attenuation factor a_{p}. We then decided to include this loss as a part of the attenuation experienced by the pulse in one round trip and consider the Sagnac interferometer itself part of the figure-9 resonator. The in-coupling and out-coupling energy rates of the figure-9 resonator, in this case, need to be normalized to the attenuation factor, obtaining:

$$\rho_{\text{in}} = \frac{1}{a_{\text{p}}}\frac{|\mathrm{t}_{12}|^2}{T_{\text{RT}}} = \frac{1}{T_{\text{RT}}} \tag{5.9}$$

$$\rho_{\text{out}} = \frac{1}{a_{\text{p}}}\frac{|\mathrm{t}_{21}|^2}{T_{\text{RT}}} = 0 \tag{5.10}$$

By summing the coupling energy rates of the figure-9 resonator and the energy rates due to the internal (non-radiative) losses, we obtain the loading and decay rates, ρ_{L} and ρ_{D}, associated to the loading and decay process respectively:

$$\rho_{\text{L}} = \rho_{\text{in}} + \rho_0 = \frac{1}{T_{\text{RT}}} + \frac{1}{\tau_0} \tag{5.11}$$

$$\rho_{\text{D}} = \rho_{\text{out}} + \rho_0 = \frac{1}{\tau_0} \tag{5.12}$$

where τ_0 is the internal, non-radiative decay time, associated with absorption or energy dissipation inside the cavity, which in this case, includes also the loss exhibited by the Sagnac interferometer. In the parameter τ_0 we also included the decay of energy due to the small leakage from the reflective element. From Eq. 5.11 we note that when the resonator is in the fully open state at time $t_1 \leq t < t_2$, the system is actually not a cavity, but an ordinary delay line/waveguide with a reflective termination, and the delay experienced by the pulse is simply T_{RT}. It thus seems not possible to associate a linewidth to the cavity in the open state. However, as we have already mentioned in the previous chapter, the acceptance bandwidth is by definition the FWHM of the Lorentzian profile associated to the energy loading process of the cavity. In this way, a

linewidth related to a "fictitious" loading resonant mode, which is quantified by the in-coupling energy rate, ρ_{in} and the intrinsic energy rate ρ_0, can always be associated to the cavity even in this extreme case of fully open state.
Inserting Eq. 5.11 and 5.12 into the general expression of the TBP (Eq. 4.1) we obtain the following simple relation:

$$TBP = \frac{\rho_{\text{L}}}{\rho_{\text{D}}} = \frac{\tau_0}{T_{\text{RT}}} + 1 = \frac{\mathcal{F}_{\text{closed}}}{2\pi} + 1 \tag{5.13}$$

with $\mathcal{F}_{\text{closed}}$ the finesse of the closed cavity. As a result, by decoupling in time the cavity photon lifetime τ_{D} (or equivalently the cavity bandwidth $\Delta\omega_{\text{cav}}$), from the acceptance bandwidth $\Delta\omega_{\text{acc}}$ such that $\rho_{\text{L}} > \rho_{\text{D}}$, the TBP of the system can be higher than 1. The fully open state represents an extreme situation where we can couple in all the power without observing any reflection. Nevertheless, a TBP > 1 is possible also for not completely open cavity, as we have seen in the previous chapter. We stress that, even if the actual bandwidth physically coupled inside the cavity is in practice only limited by the operating frequency region of the 50/50 coupler, the acceptance bandwidth that has to be considered in calculating the TBP is the FWHM of the Lorentzian profile associated to the energy loading process. It is thus not given by the bandwidth of the incoming pulse. As a matter of fact, the energy of an incoming pulse that is shorter than the cavity round-trip time (i.e. with a bandwidth larger than the FSR) decays over more than one cavity resonance mode and this does not change the value of the TBP of the system, which has to be always evaluated considering one single *Lorentzian* resonance mode.

It should be noticed that, as any other fiber optic resonator based on standard single mode fiber, this system is subject to the limitations dictated by dispersion and nonlinearity. Specifically, in case of storing of a data pattern made of a sequence of ultra-short pulses, the storage time would be limited by dispersion since the pulses would broaden and could cause the loss of information originally contained in the pattern. This can be dealt, to a certain amount, by dispersion management of the cavity. Besides, an excessively high peak power would induce nonlinear effects, leading to spectral broadening and distortion of the optical bit stream [113]. Another constraint is represented by the limited time-window permitted by the system for coupling the input signal. In fact, due to the time-variant nature of the front mirror, the duration of the signal that has to be stored, cannot be longer than the cavity round-trip time, since any superposition at the phase modulator, during the in-coupling process, would also couple part of the signal out of the resonator. However, this work did not aim at proposing a novel device, rather at demonstrating a theoretical principle according to which a resonant system with a nonreciprocal coupling can exhibit an arbitrarily high TBP. Besides that, a correct evaluation of the TBP requires an output signal and spectrum free of distortions, as they can affect the central frequency or the duration of the original pulse. Therefore, in the experiments, we chose the peak power and

the pulse duration in order to have negligible effect of dispersion and nonlinearity, although, in the theoretical context of the time-bandwidth performance, there is no restriction regarding the peak power and the pulse duration.

5.1.1 Experimental setup

The experimental setup used to perform the experiments is illustrated in Fig. 5.2. The input to the resonator consists of an optical input pulse train at 1551.3 nm obtained from a laser, modulated in intensity to give 500 ps-long Gaussian pulses with 894 MHz bandwidth, and a repetition rate corresponding to about 30 cavity RTs.

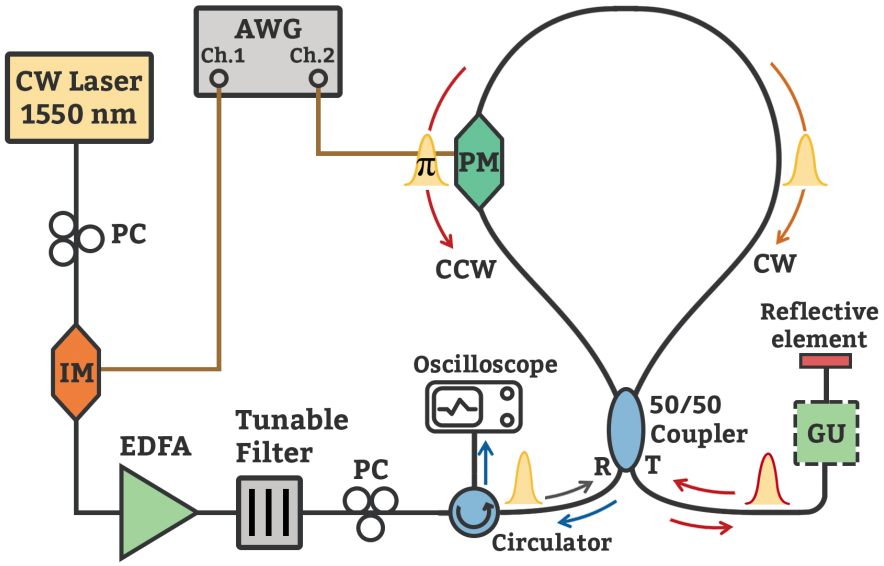

Figure 5.2 – Exponential setup used for the experiments of the catch-and-release of a 500 ps long Gaussian pulse in a time-variant figure-9 resonator. PC: polarization controller.

We synchronized an electrical pulse of 4 ns with the optical signal to activate the phase modulator when it is traversed by the CCW pulse only. The characteristics of the optical input signal and the electrical driving signal are shown in Fig. 5.3. Once extracted, the pulses are detected at the third port of a circulator, placed before the R port of the Sagnac interferometer, by using a high-speed sampling oscilloscope. Both the electrical signals used to drive the phase and the intensity modulator (IM) were generated by the same arbitrary waveform generator (AWG) (Tektronix model 7122B). The phase modulator used for the experiments was a $LiNbO_3$ electro-optic modulator (Photline model MPZ-LN-10) with an electro-optic bandwidth of 12 GHz. The synchronization between the electrical "gate" and the optical signal was performed directly from the AWG by imposing a delay on the electrical signal that drove the phase modulator.

Since according to Eq. 5.13, the cavity finesse limits the TBP, we experimentally con-

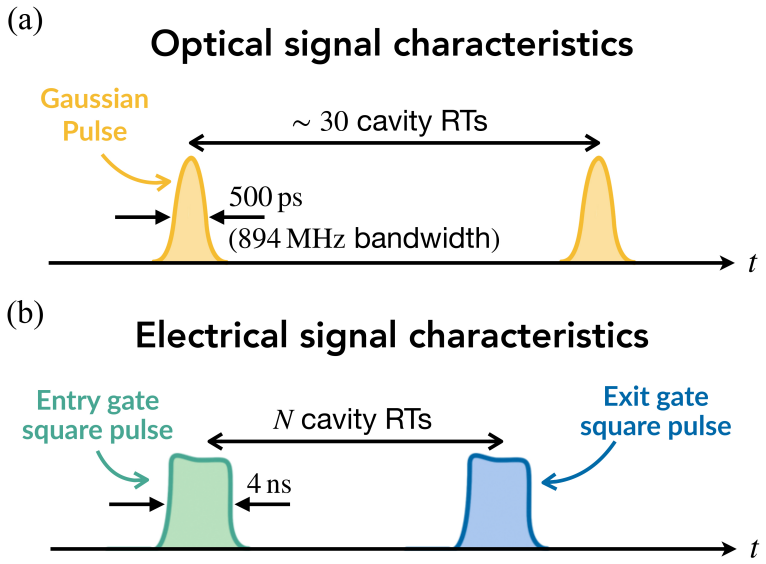

Figure 5.3 – (a) Optical signal entering the figure-9 resonator made of a train of 500 ps-long Gaussian pulses with a period of about 30 cavity RTs. (b) Electrical signal used to drive the phase modulator made of a train of 4 ns-long squared pulses with a period of an arbitrary number of cavity RTs. The entry gate pulse was synchronized with the optical input pulse to perform the pulse injection, while the exit gate pulse was used to extract the intra-cavity optical pulse at a desired number of RTs.

trolled $\mathcal{F}_{\text{closed}}$ by inserting a gain unit, which consists in a homemade bidirectional optical amplifier, inside the resonator. As such, we could tune τ_0 by varying the amplifier gain. The gain unit was made of 90 cm-long Erbium-doped fiber (EDF) connected with two fused fiber wavelength division multiplexers and pumped by a semiconductor laser diode at 980 nm. We measured the cavity round-trip time to be 48 ns and 120.3 ns, without and with the EDFA respectively. It is important to note that the addition of an EDFA was a means to overcome relatively high absorption losses, adding gain without exceeding the losses, while not affecting the general principle. In fact, an analogous amplification would never increase the TBP beyond one (1) in a reciprocal resonator, as more power would simply also leak out the system at every round trip.

5.2 Results and discussion

We assessed the performance of the system by measuring the energy of the pulse released after different numbers of RTs. Figure 5.4a shows the results for the passive cavity (no EDFA). The exponential decay fit of the experimental data corresponds to a decay time τ_0 of about 65.69 ns, which allowed us to extract a pulse above the noise level after up to 10 RTs. This corresponds to a closed cavity decay-time of about 1.37 times longer than the cavity RT time, leading to a TBP of 2.37. According to Eq. 5.13,

the maximum achievable TBP can be in principle infinite, providing an infinitely long closed-cavity decay time τ_0, i.e. a loss-less cavity. However, in our case τ_0 is limited by a technological constraint, specifically the absorption losses at the modulator measured to be $\sim$3.17 dB/RT, whereas the excess loss and the reflectivity of the FBG were 0.2 dB and 97%, respectively. We therefore used the active cavity configuration (with EDFA) to support the claim of arbitrarily large TBP by experimentally controlling the decay time of the system. We progressively adjusted the power of the EDFA to partially compensate the intra-cavity loss over three different steps resulting in a net loss of 0.4, 0.25, 0.15 dB/RT. The measurements are shown in Fig. 5.4b, where the experimental data is normalized to the energy of the pulse extracted after the first cavity RT. As the addition of the EDFA increases T_{RT}, according to Eq. 5.13, this might actually reduce the TBP of the system. However, the significant increase in τ_0 allowed sustaining the pulse for up to 120 RTs (red curve). The decay time strongly increased from 65.69 ns up to 3.57 μs, resulting in a maximum TBP of 30.7. For this measurements, the period of the input pulse train lied between 30 and 31 RTs, to avoid time overlap between the intra-cavity pulse in its 31$^{\mathrm{st}}$ round trip and the new incoming input pulse. In this way, we could couple multiple pulses in the resonator and extract an individual pulse after more than 30 RTs without affecting the others.

In principle, we could achieve an even higher TBP value by intensifying the pump power of the EDFA as to fully compensate the round-trip loss. Under these conditions the TBP is higher, but now limited by dispersion, nonlinear effects and the amplification of noise by the EDFA. However, in practice, we were limited by the gain saturation of the doped fiber. This effect can be seen in Fig. 5.4b for the configuration with 0.15 and 0.25 dB/RT of effective losses. In fact, here the pulses retrieved at the first RT have energies sufficiently high to saturate the gain of the amplifier, which cannot compensate for the cavity losses in the same way as for the pulses extracted after more RTs. This results in higher effective cavity losses at the first experimental point, which we therefore excluded from the fit. Further increasing the diode pump power would have affected even more points, misleading the estimate of the TBP. In order to confirm this concept and prove that the gain unit was necessary only to overcome a technological constraint, but without affecting the general principle behind the TBP, we conducted detailed simulations of the pulse storing operation using VPIphotonics software. The simulations were performed using the tool VPItransmissionMaker Optical Systems whose numerical solver is based on a full-wave analysis. We reproduced the setup in the graphical environment using built-in blocks with customized parameters. Our experimental resonator was numerically modeled in 4 passive configurations (without EDFA): in the first one we have reproduced the exact passive experimental cavity, while in the other three configurations we have set the total loss and T_{RT} as to mimic the three values of the experimental active setup. The normalized energy of the pulses collected at different RTs is plotted in Fig. 5.4c for the first case and in Fig. 5.4d for the other three cases. For all, the TBP value is in excellent agreement with the one calcu-

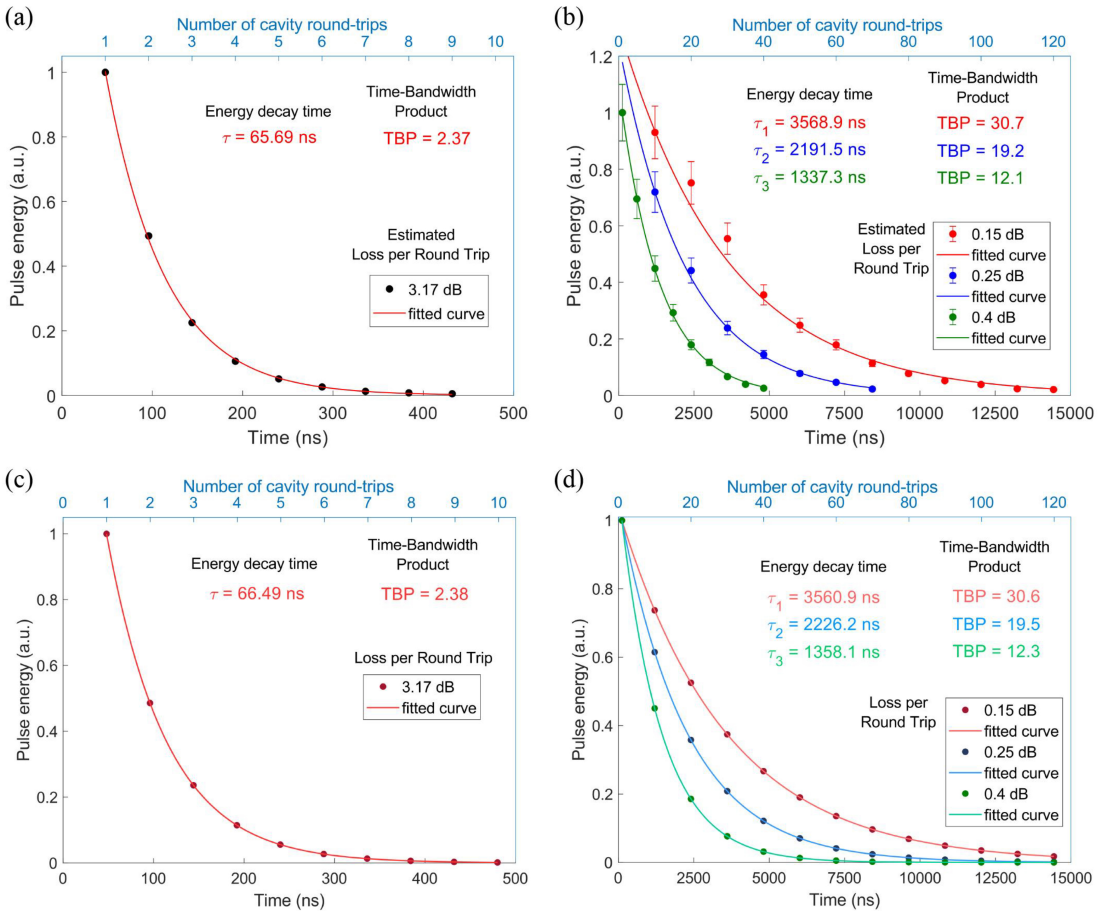

Figure 5.4 – (a) Experimentally measured energy decay curve for the 500 ps Gaussian pulse extracted from the full polarization maintaining fiber passive resonator at every round trip time ($T_{\mathrm{RT}} = 48$ ns). (b) Experimentally measured energy decay curves for the pulses extracted from the amplified resonator every ten round trips (with $T_{\mathrm{RT}} = 120.3$ ns) for different values of loss per RT. Error bars in (b) come from fast polarization rotation due to the non-polarization maintaining erbium doped fiber in the gain unit, resulting in a 20% of uncertainty. (c) Simulated energy decay curve of the passive cavity with the same actual value of loss/RT as for (a). (d) Simulated energy decay curves of a passive cavity configuration with the same actual value of loss/RT as for (b).

lated after fitting of the experimental data. In particular for Fig. 5.4d, the exponential decay fits almost perfectly the experiments, showing decay times from 1.36 to 3.56 μs as the dissipative losses progressively decrease. The simulations not only confirm the improvement in TBP but also that we can indeed treat our active cavity as a passive cavity with reduced dissipative losses.

In Fig. 5.5 we provide an example showing the temporal traces of a 4 ns squared pulse

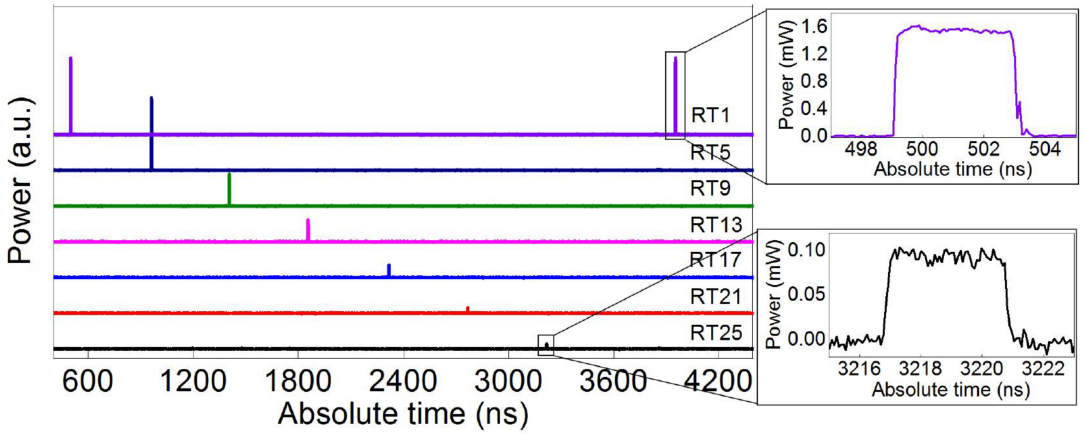

Figure 5.5 – Temporal traces over one period of the optical pulse train extracted after different RTs. The diode pump power of the gain unit was adjusted to obtain a configuration with about 0.5 dB of loss per round trip.

stored in the resonator and extracted after different RTs, with loss of about 0.5 dB/RT. The pulse can be extracted after up to 25 RTs and no leakage is observed between two subsequent extracted pulses. This confirms that we can couple the entire pulse energy ($|t_{12}|^2 \approx 1$) without any out-coupling loss ($|t_{21}|^2 \approx 0$), switching the cavity from the completely open to the completely closed state. For this specific measurement we used a longer and square-shaped pulse because the acquisition memory of our oscilloscope was not sufficient to detect the 500 ps-long Gaussian pulses over the entire time period of the pulse train (about 3.6 μs).

I want to remark here that, using this system we do not need to adiabatically compress the input pulse bandwidth to match the closed cavity resonance and avoid scattering between different resonant modes, as proposed in other works [40, 43, 110, 111]. In fact, we are in a non-adiabatic regime, as T_{RT} is longer than the tuning time, which is given by the rising time of the phase modulator. Moreover, with T_{RT} being longer than the pulse duration, the injected pulse does not interfere with itself and cannot 'see' the closed-cavity resonant modes. Therefore, the pulse does not need to adapt to the closed-cavity resonances and, once released, it exhibits a spectrum that is unaffected by the switching between the two different cavity states.

To clearly show that the characteristics of the released pulses are preserved over all the RTs, we collected temporal waveforms and radio-frequency (RF) spectra of the 500 ps Gaussian pulse after 1, 40 and 80 RTs (Figs. 5.6b, 5.6c and 5.6d) and plotted together with those of the pulse collected before entering the cavity (Fig. 5.6a). The temporal traces were registered by detecting the extracted pulses on a sampling oscilloscope with 20 GHz of optical bandwidth. Given the limited resolution of our OSA, a direct measurement of the pulse spectrum in the optical domain did not provide the suitable

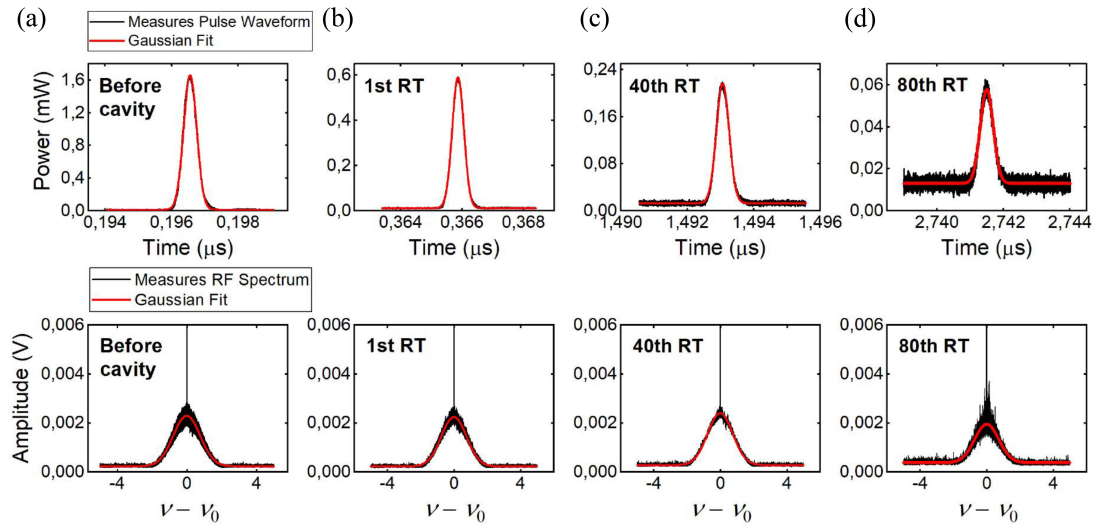

Figure 5.6 – Pulse waveforms and radio-frequency spectra acquired before the cavity (a) and after 1 RT (b), 40 RTs (c) and 80 RTs (d). The product of the pulse duration and the bandwidth (FWHM) gives values close to the transform-limited pulse for all the three cases.

resolution to detect variations in the spectrum of the order of the cavity free-spectral range (about 8 MHz). We thus implemented a zero-delay self-heterodyne technique [114], to map the optical spectrum of the pulses into the radio-frequency domain. The pulses retrieved from the resonator were modulated using a 40 GHz Mach-Zehnder modulator to create sidebands at 16 GHz from the central pulse frequency and sent to an Electrical Spectrum Analyzer (ESA). The bottom row of Fig. 5.6 reports the radio-frequency spectra, given by the convolution of the beating lines acquired with the ESA and centered at the modulation frequency. The origin of the noise seen in the spectra is the amplified spontaneous emission generated by the EDFA. This amount of noise was quite sensitive to the polarization alignment, which was always hard to achieve during the measurements mainly because the gain unit was not made of polarization maintaining fiber. From a comparison with the pulse acquired before entering the resonator, we note that the resonating pulses do not suffer any measurable distortions and their spectra are well preserved over all 80 RTs. This is also confirmed by the product of the pulse duration and bandwidth (FWHM) retrieved from the Gaussian fit, which was always about 0.44 for the investigated RTs.

5.3 Summary

In this chapter an experimental implementation of the resonant system with a non-reciprocal coupling based on the time-variant figure-9 resonator has been presented. The system was designed such that the Sagnac interferometer acted as a nonreciprocal front mirror. This was possible owing to a localized phase variation provided by an

electrically-driven phase modulator, which was placed at an offset position from the loop midpoint to ensure that the phase shift was imparted only to one of the two counter-propagating pulses. This spatial asymmetry together with the temporal modulation allowed to perform the nonreciprocal coupling. In fact, by means of an electrical squared pulse synchronized with the optical input to bias the phase modulator when it is traversed by the CCW propagating pulse, we were able to fully coupled a pulse inside the resonator and store it for an arbitrarily amount of time. In such a system we could then identify an open state and a closed state during which the resonator exhibits two different Lorentzian bandwidths: the acceptance bandwidth and the cavity bandwidth, associated respectively to the energy loading and decay process of the resonator. We have seen that the TBP of an individual resonator with such characteristics is ultimately equal to $\tau_0/T_{\mathrm{RT}} + 1$ and can be increased at will above the limit, provided that internal, dissipative losses are kept sufficiently low.

By measuring the energy of the released pulses after different numbers of RTs, we then retrieved the intrinsic decay time τ_0 and calculated the corresponding TBP. Given the significant absorption loss of the phase modulator, we could obtain a TBP value of 2.37, which is just above the fundamental limit. We therefore inserted an EDFA to partially compensate for the intra-cavity loss. By using this active configuration the decay time strongly increased up to 3.57 μs, resulting in a maximum TBP of 30.7. To demonstrate that the gain unit, used to compensate for the strong intra-cavity (non-radiative) loss, did not affect the general principle of the TBP, we conducted detailed simulations of the pulse storing operation using VPIphotonics software. The simulations were performed reproducing the system in the passive configuration imposing for the intra-cavity absorption loss the value given by the difference between the gain provided by the EDFA and the actual intra-cavity loss. The results obtained were in excellent agreement with those calculated after fitting of the experimental data, proving that it is perfecly allowble to treat the active system as the passive system with reduced dissipative losses.

The chapter ends by showing the traces of the temporal waveforms and RF spectra of the released pulse acquired after different round-trips. The results show that neither the temporal width nor the spectrum of the pulse is distorted compared to the pulse at the input of the resonator. The confirmation of the preserved characteristics of the released pulse was crucial for a correct evaluation of the TBP, which requires an output signal and spectrum free of detectable distortions, as they can affect the central frequency or the duration of the original pulse, thus leading to an unreliable estimation of the energy decay time.

6 Equalization of electro-optic frequency combs

The need for a frequency ruler as a means to measure optical frequencies has been continuously moving the interest of researchers and scientists since the realization of the first mode-locked laser (MLL) in 1964. Such laser exhibited an optical spectrum characterized by a series of coherent equally-spaced spectral lines that we now use to call *optical frequency comb* (OFC). Since then, the technology for the generation of OFCs has been significantly growing [92, 115–117] and nowadays it includes other techniques such as those based on the acousto-optic [118] and electro-optic (EO) modulation [119] or those that exploit the nonlinear Kerr effect in passive optical microresonators [120, 121]. The OFCs are used in a wide and diverse set of applications ranging from spectroscopy [122], optical metrology [123] and light detection and ranging (LIDAR) [124, 125] to optical communications [126] and microwave photonics [127]. The reasons of this success lie in the remarkable feature that such combs allows to link the photonic to the microwave frequencies.

Among the various techniques used for OFC generation, EO modulators-based combs [119] have recently attracted more attention thanks to the significant improvements of the lithium niobate waveguide technology, which enabled EO modulators with an increased bandwidth (40 GHz or more). This allows the repetition frequency of the EO comb to be easily tuned simply by changing the frequency of the radio-frequency (RF) sinusoidal source that drives the modulator. In addition, the central frequency of the comb can be tuned since the EO modulators work over a wide range of optical frequencies, e.g. 30-40 nm in the C-band. However, this technology exhibits some drawbacks. For instance, nowadays most of the commercially available EO modulators are designed to operate in a specific optical communication band, meaning that to generate an OFC at a given wavelength, the EO modulator working at the corresponding operating band must be used. Moreover, given their dependence on the Bessel functions of the first kind, the comb lines exhibit a strong variation in amplitude, even in the central region of the comb. This represents a limitation for all applications requiring a flat-topped comb, such as arbitrary waveform generation, optical

communications and sensing.

After a brief introduction, where the fundamental concepts behind the OFC generation are explained, I will present in this chapter an experimental realization of a cost-effective EO comb generation and equalization method using a single phase modulator in a Sagnac interferometer scheme.

6.1 Fundamental concepts of optical frequency comb generation

An OFC is a series of equidistant spectral lines that are mutually coherent. Their main characteristics can be easily explained by looking at their corresponding form in the time domain, which is a train of short pulses, as schematically illustrated in Fig. 6.1. As a matter of fact, one of the most common way to generate an OFC is through a train of ultra-short pulses emitted by a MLL. We will therefore start from here to analytically describe their origin.

6.1.1 Theory of frequency comb generation

Let us consider a pulse train emitted by a MLL at a carrier frequency ω_c. Let us denote with A and $\tau = 2\pi/\omega_r$ the pulse envelope and the pulse repetition rate respectively, with ω_r the repetition frequency, and suppose that between two successive pulses, there is a phase shift ϕ that is due to the difference between the group velocity of each pulse and the phase velocity of the wave. This phase shift is fundamental for the definition of the OFC since it confers the mutual coherence between each comb line. Under the theoretical limit of infinite waveform, we can write the pulse train in the time domain as following [119]:

$$f(t) = \sum_{n=-\infty}^{\infty} [A(t)\cos(\omega_c t - n\phi) * \delta(t - n\tau)] \tag{6.1}$$

where n is an integer, δ is the Dirac distribution and $*$ is the convolution product. Then, by taking the Fourier transform we obtain the spectrum of the pulse train:

$$\widetilde{f}(t) = \mathfrak{F}[f(t)] = \int_{-\infty}^{\infty} f(t)e^{-j\omega t}dt = \pi\omega_r \widetilde{A}(\omega - \omega_c) \sum_{n=-\infty}^{\infty} \delta(\omega - \omega_0 - n\omega_r) + \\ + \pi\omega_r \widetilde{A}(\omega + \omega_c) \sum_{n=-\infty}^{\infty} \delta(\omega + \omega_0 - n\omega_r) \tag{6.2}$$

where $\widetilde{A}(\omega) = \mathfrak{F}[A(t)]$ is the spectral envelope, while $\omega_0 = \phi/\tau$ is the *carrier envelope offset frequency*, which represents the overall shift of the entire comb from the origin of

the frequency axis. From the above equation we note that each frequency of the comb can be determined by the following relation:

$$\omega_n = \omega_0 + n\omega_r \tag{6.3}$$

For typical conventional MLL, ω_r goes from few megahertz (MHz) up to several gigahertz (GHz) and also ω_0 lies into the RF domain. This allows to measure optical frequencies with an extreme accuracy provided that ω_r and ω_0 are known.

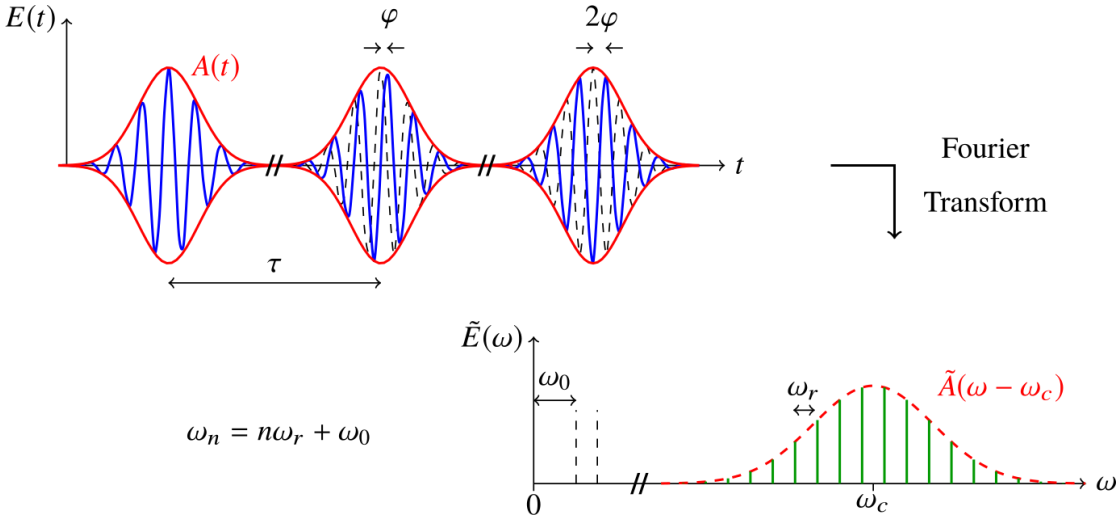

Figure 6.1 – Representation of a pulse train emitted by a MLL and its corresponding frequency spectrum. A phase shift ϕ exists between two successive pulses due to the different velocity between the pulse envelope and the carrier. The frequency spectrum is characterized by a frequency spacing between each comb line, that is equal to the repetition frequency of the pulse train, and an offset frequency that is related to the phase shift ϕ. Adapted from ref. [119].

6.1.2 Comb generation using an electro-optic phase modulator

EO frequency combs, among other sources like MLLs and recent chip-scale Kerr micro-combs [128], provide a simple yet fully flexible comb generation technique in terms of free spectral range (FSR) and bandwidth. Generally, the FSRs achieved by the EO combs also fill the gaps between MLLs and micro-combs. EO combs are typically generated by the external modulation of a continuous-wave laser in an electro-optic modulator (EOM). To date, various types of EOMs have been explored for EO comb generation, including but not limited to phase modulators [129, 130], Mach-Zehnder modulators (MZMs) [64, 131], polarization modulators [61], dual-drive [132, 133] or dual-parallel [134] MZMs, resonant phase modulators [135], as well as the combinations among them [67, 136, 137].

I will now introduce the fundamental theory behind the generation of EO frequency

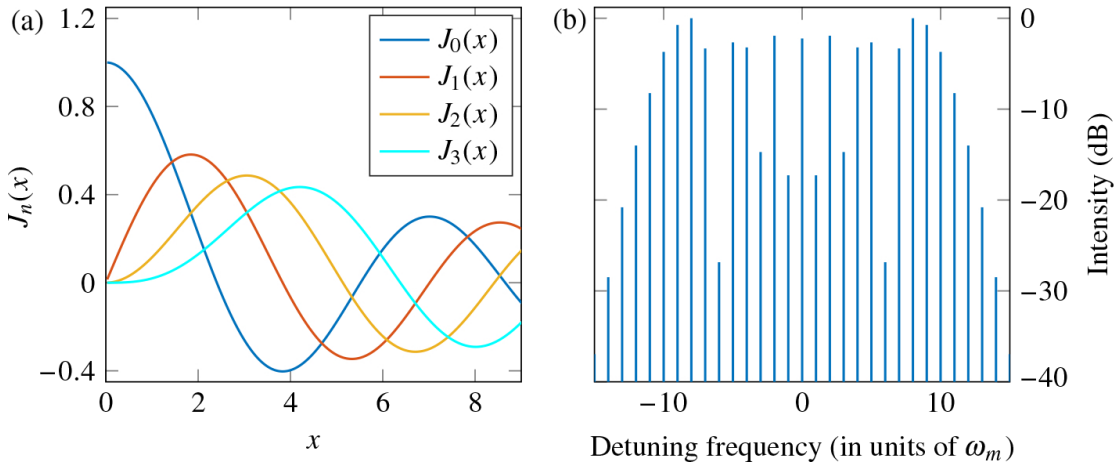

Figure 6.2 – (a) Plot of the first four Bessel functions of the first kind. (b) Plot of a simulated EO comb generated using a phase modulator with $\beta_p = 10$. The amplitude of the comb lines follows the Bessel functions of the first kind. Adapted from ref. [119].

combs. Specifically, the treatment will focus on EO combs generated using phase modulators (PM).

Let us consider a PM with modulation index K driven by an electrical sinusoidal signal whose electric field is given by $V(t) = V_0 \sin(\omega_m t)$, where V_0 is the peak voltage and ω_m is the modulation frequency. Owing to the Pockels effect, an optical signal traversing the PM acquires a phase $\Delta\theta = KV(t)$ and its electric field after exiting the modulator can be represented by the following Fourier series [138]:

$$E_{\text{out}}(t) = E_0 e^{j\omega_c t} \sum_{k=-\infty}^{\infty} J_k(\beta_p) \exp(jk\omega_m t) \qquad \text{with} \quad k \in \mathbb{Z} \tag{6.4}$$

where ω_c is the frequency of the optical carrier, $\beta_p = KV_0$ is the peak phase deviation, while J_k are the Bessel functions of the first kind, which are plotted in Fig. 6.2a until the third order. By taking the Fourier transform we get the frequency spectrum of the phase modulated optical signal, namely:

$$\widetilde{E}(\omega) = \mathfrak{F}[E_{\text{out}}(t)] = E_0 \sum_{k=-\infty}^{\infty} J_k(\beta_p)\delta(\omega - k\omega_m - \omega_c) \tag{6.5}$$

where the frequencies of the comb lines are related by:

$$\omega_k = k\omega_m + \omega_c \tag{6.6}$$

An example of the frequency comb generated using a PM with $\beta_p = 10$ is shown in Fig. 6.2b. We can note how the amplitude of the comb lines, resulting from a pure phase modulation of a single RF tone, follows the Bessel functions of the first kind,

which show a large power imbalance at a fixed modulation index and thus prevent to obtain a flat-topped frequency comb. This is an issue that has been addressed by many researchers and, as we will see in the next section, several approaches have been studied for this purpose.

6.2 Equalization of electro-optic frequency combs using a Sagnac interferometer

The equalization of EO comb-line power are desired in many occasions. For instance, it is required when the EO combs are used as the independent data carriers in optical communication systems [126], or for some applications related to fiber sensing [130] and molecular spectroscopy [122]. Several setups aiming at generating a flat EO comb have been proposed, but all of them require the use of two or more EOMs [60–66] or a further processing of the driving RF signal [67–70]. A more simple and effective EO comb equalization scheme has been demonstrated using a dual-drive MZM driven by two RF sinusoidal signal slightly offsetted in amplitude [132, 133]. They theoretically showed and experimentally verified, that a flat-topped EO frequency comb can be obtained, at large powers of the driving RF signal, if the sum of the peak-to-peak phase deviation induced in each arm and the dc bias difference between the two arms is equal to π. In mathematical terms this condition takes the following form:

$$\Delta\beta \pm \Delta\phi = \pi \tag{6.7}$$

where $\Delta\beta = \beta_{p1} - \beta_{p2}$ and $\Delta\phi = \phi_1 - \phi_2$ with 1 and 2 indicating the two arms of the MZM. At large powers of the driving RF signal the power conversion efficiency from the optical carrier to each harmonic mode results to be independent on the harmonic order of the driving signal and it is maximized when $\Delta\beta = \Delta\phi = \pi/2$. Under this condition the resulted comb presents a spectrum with a maximum power variation of 3 dB between each comb line within a spectral region equal to 1/2 of its bandwidth.

Following the idea of using the interference to achieve a flat comb, we experimentally implemented a system for the generation and equalization of EO combs, by using a more cost-effective structure that consists in a standard PM inserted in a Sagnac interferometric scheme. Figure 6.3 shows a basic illustration of such a system, whose operating principle is described below.

6.2.1 Principles of operation

The PM is connected between the two output ports of a polarization maintaining 50/50 fiber optic coupler. The branches of the coupler have different lengths so that the position of the PM within the Sagnac loop results shifted of a length $\Delta L/2$ from

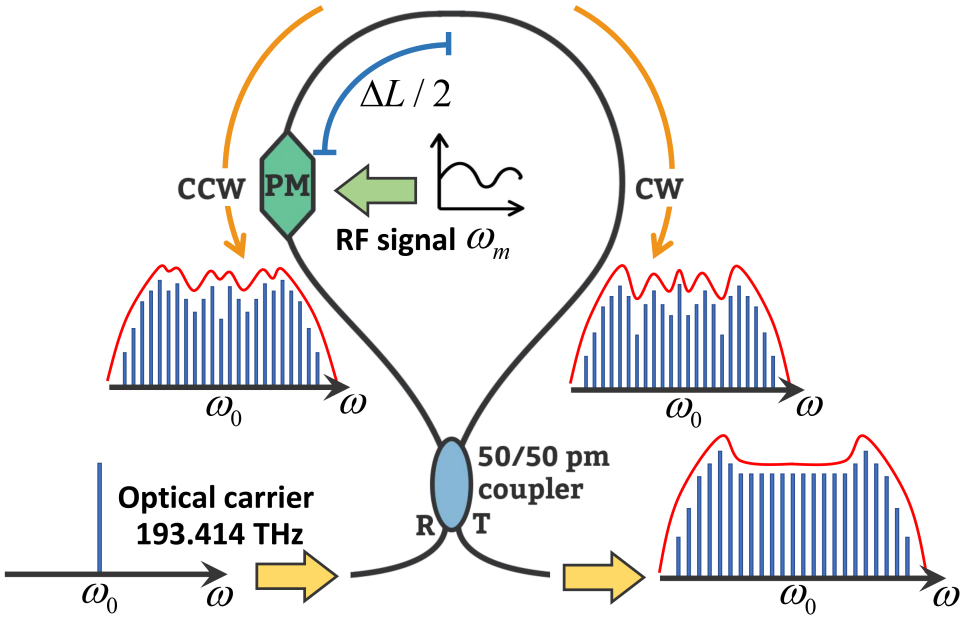

Figure 6.3 – Schematic illustration and operating principles of the Sagnac interferometer-based system for the generation and equalization of EO frequency combs.

the loop midpoint. Let be β_{cw} and β_{ccw} the peak phase deviations imparted by the PM respectively for the CW and CCW direction, and let us suppose that it is driven by an electrical sinusoidal signal whose electric field is given by $V(t) = V_0 \sin(\omega_m t)$, where V_0 is the peak voltage and ω_m is the modulation frequency. If an optical carrier $E_{\mathrm{in}} = E_0 e^{j\omega_c t}$ at optical frequency $\omega_c = 193.414$ THz (∼1550 nm) enters the Sagnac interferometer from port R of the 50/50 coupler, the electric fields of the CW and CCW wave after passing through the PM are given by the following expressions:

$$E_{\mathrm{cw}}(t) = \frac{E_{\mathrm{in}}}{2} \sum_{k=-\infty}^{\infty} J_k(\beta_{\mathrm{cw}}) \exp(jk\omega_m t) \exp\left(-jk\phi_{\mathrm{cw}}\right) \tag{6.8}$$

$$E_{\mathrm{ccw}}(t) = \frac{E_{\mathrm{in}}}{2} \sum_{k=-\infty}^{\infty} J_k(\beta_{\mathrm{ccw}}) \exp(jk\omega_m t) \exp\left(-jk\phi_{\mathrm{ccw}}\right) \tag{6.9}$$

In the above expressions $\beta_{\mathrm{cw}} = \pi V_0 / V_{\pi,\mathrm{cw}}$ and $\beta_{\mathrm{ccw}} = \pi V_0 / V_{\pi,\mathrm{ccw}}$ with $V_{\pi,\mathrm{cw}}$ and $V_{\pi,\mathrm{ccw}}$ the voltage needed to induce a π phase shift in the CW and CCW direction, respectively, while J_k are the Bessel functions of the first kind. Also, $\phi_{\mathrm{cw}} = (n\omega_m/c)L_{\mathrm{cw}}$ and $\phi_{\mathrm{ccw}} = (n\omega_m/c)L_{\mathrm{ccw}}$, where L_{cw} and L_{ccw} are the path lengths traveled by the CW and CCW combs, respectively, while n is the refractive index of the fiber, and c is the speed of light in vacuum.

The electric field of the signal exiting the interferometer from the T port of the coupler

is then given by:

$$E_{\text{out}}(t) = \frac{E_{\text{in}}}{2} \sum_{k=-\infty}^{\infty} \left[J_k(\beta_{\text{cw}}) \exp\left(-jk\frac{n\omega_m}{c}L_{\text{cw}}\right) - J_k(\beta_{\text{ccw}}) \exp\left(-jk\frac{n\omega_m}{c}L_{\text{ccw}}\right) \right] e^{jk\omega_m t} \tag{6.10}$$

from which we can retrieve the power of each comb line as follows:

$$P_k = \frac{|E_{\text{in}}|^2}{4} \left[J_k^2(\beta_{\text{cw}}) + J_k^2(\beta_{\text{ccw}}) - 2J_k(\beta_{\text{cw}})J_k(\beta_{\text{ccw}}) \cos\left(k\Delta\phi\right) \right] \tag{6.11}$$

where $\Delta\phi = n(\omega_m/c)\Delta L$, with $\Delta L = L_{\text{cw}} - L_{\text{ccw}}$ being the difference in length between the paths traveled by the two counter-propagating combs. In principle, to obtain a perfectly flat comb, the condition in Eq. 6.7 must be fulfilled. This is a situation that occurs when the PM operates at modulation frequencies where it works in both directions and exhibits two slightly different modulation indices. Conventional PMs typically works only in one direction at high modulation frequencies, due to the mismatch of the propagation speeds between the RF wave and the optical wave inside the EOM [139–141]. However, the conversion efficiency in the two directions converges to the same value when decreasing the modulation frequency. Besides, the phase delay difference $\Delta\phi$ is ensured by the asymmetric position of the PM inside the loop. However, we can immediately notice that this phase difference is dependent on the harmonic order k. Although, this prevents to obtain a perfectly flat comb due to the different phases acquired by each comb line, an equalization in the central region of the comb can be still achieved even when the above condition in Eq. 6.7 is not strictly satisfied. This can be clearly seen from Fig. 6.4a where the equalization of EO combs related to the system in Fig. 6.3 is evaluated, by using Eq. 6.11, for all the combination of β_{cw} and $\Delta\phi$, ranging from 7 to 16 and from 0 to π respectively, and imposing $\Delta\beta = 0.11$. To obtain this graph, we calculated the difference between the powers exhibited by the highest and the lowest comb line within a certain spectral bandwidth around the central frequency and varied $\Delta\beta$ until the best flatness was achieved. For small values of $\Delta\beta$, the comb exhibits a "rabbit-ears"-like shape [127], therefore, to have a quantitative measure of the flatness of the comb, we evaluated the power variation within an interval ΔN around the central frequency defined as:

$$\Delta N = \pm(N_{\text{c}} - 3) \tag{6.12}$$

where N_{c} is the comb number of the highest comb line. From Fig. 6.4a we note that although the best result is found for $\Delta\phi = 1.3$ rad and $\beta_{\text{cw}} = 9.6$ rad, a good flatness is obtained also for other combinations of $\Delta\phi$ and β_{cw}.

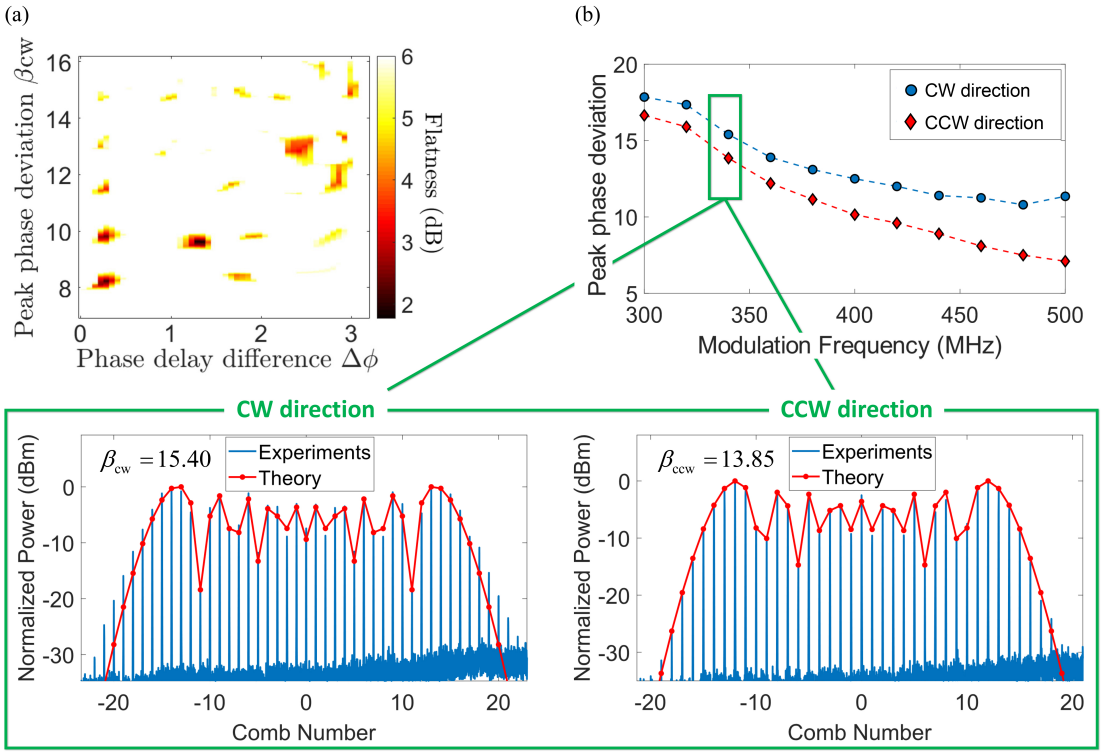

Figure 6.4 – (a) Flatness of EO frequency combs theoretically evaluated by using Eq. 6.11 for all the combination of β_{cw} and $\Delta\phi$, ranging from 7 to 16 and from 0 to π respectively, and imposing $\Delta\beta = 0.11$. (b) Top panel: Peak phase deviation exhibited by the phase modulator at 11.5 dBm, in the CW and CCW direction for different values of the modulation frequency between 300 and 500 MHz. Bottom panel: Comb spectra acquired in the two directions in single-pass configuration at a modulation frequency of 340 MHz. The theoretical fit of the Bessel functions of the first kind corresponds to a peak phase deviation of 13.85 and 15.40 for the CW and CCW direction respectively.

6.2.2 Experimental results and discussion

To find the bidirectional operating point of the PM corresponding to a value of $\Delta\beta$ lying around 0.11 rad, we first evaluated the peak phase deviation imparted by the PM in the two directions varying the modulation frequency from 300 to 500 MHz with intervals of 20 MHz. For this purpose, we measured the frequency combs generated by the PM in a single-pass configuration and fitted with the theory. The spectra were acquired in the RF domain using an electrical spectrum analyzer (ESA). To do so, we inserted the PM in a self-heterodyne setup, as illustrated in Fig. 6.5. The optical carrier at 193.414 THz, provided by a continuous-wave tunable laser, was split in two equal parts by a 50/50 polarization maintaining coupler. One part was sent to the PM for the comb generation, while the other part was modulated using a 40 GHz MZM to create side-bands at 17 GHz. The signal exiting the MZM then passed through a wave-shaper to filter out one of the two side-bands and the high-order harmonics.

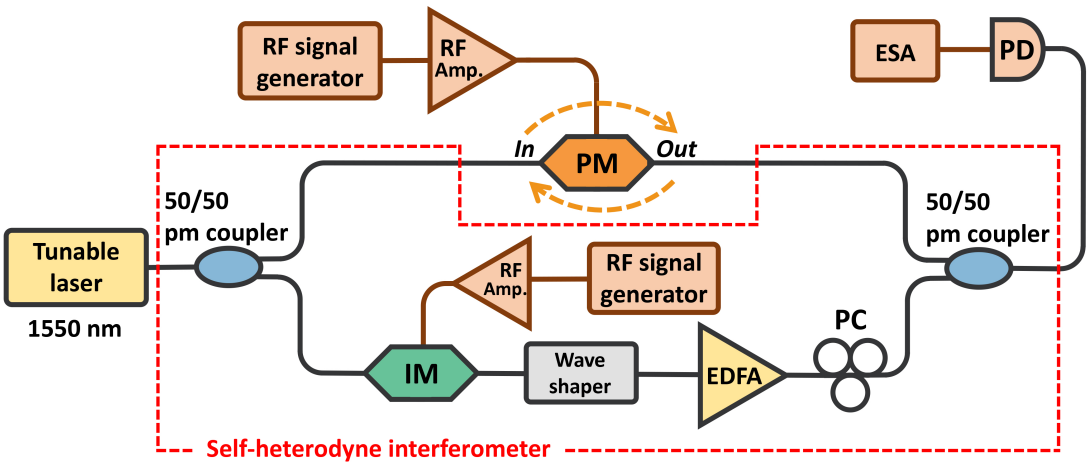

Figure 6.5 – Experimental setup used for the acquisition of the EO comb spectra in single-pass configuration. The PM is implemented in a self-heterodyne interferometer to register the combs in the RF domain using an electrical spectrum analyzer. IM: intensity modulator; PC: polarization controller; EDFA: Erbium-doped fiber amplifier; pm: polarization maintaining; PD: photodetector.

Finally, the spare side-band beat in another 50/50 polarization maintaining coupler with the comb generated by the PM, which is then mapped in the RF domain through a photodetector. The operating regime at large powers of the driving RF signal, in this case 11.5 dBm, was ensured by using a high power RF amplifier. The values of the peak phase deviation, retrieved for the CW and CCW direction, are shown in Fig. 6.4b as a function of the modulation frequency. From this study we found that the peak phase deviation corresponding to $\Delta\beta = 0.11$ rad lied around 340 MHz. The bottom part of Fig. 6.4 shows the comb power spectra with the theoretical fit of the Bessel functions of the first kind corresponding to this modulation frequency.

Using this value of the modulation frequency we then performed the experiments using the Sagnac interferometer scheme. The experimental setup used, that includes the self-heterodyne interferometer for the acquisition of the EO combs in the RF domain, is illustrated in Fig. 6.6a. A 500 m-long polarization-maintaining fiber was placed within the loop to ensure the asymmetric position of the PM from the loop midpoint. The reason for such a long fiber will be clarify later. The spectrum was collected by slightly adjusting the modulation frequency around 340 MHz and the RF power around 11.5 dBm, until the optimum equalization was found. Figure 6.6b shows the comb spectrum acquired at a modulation frequency of 340.474 MHz. The effect of the equalization can be observed in the central region of the comb characterized by an almost flat behavior with a relatively small spectral ripple. In this case we found a flatness of about 4 dB over 21 comb lines, which is a significant improvement compared to the values obtained in the single-pass configuration which were 13 dB in the CCW direction and 17 dB in the CW direction.

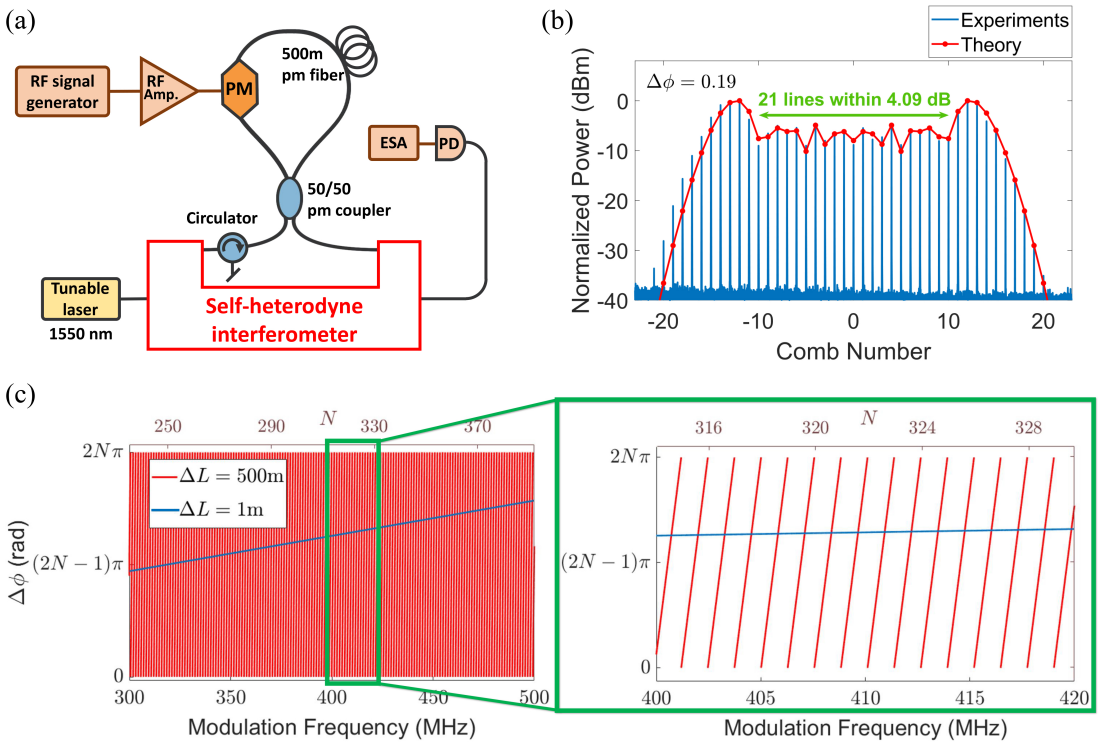

Figure 6.6 – (a) Experimental setup used for the acquisition of the equalized EO comb spectra. The Sagnac interferometer replaces the PM in the self-heterodyne setup. (b) Comb spectrum acquired at the output of the Sagnac interferometer setup at a modulation frequency of 340.474 MHz and RF power of 11.4 dBm. The effect of the equalization results in a maximum power variation of about 4 dB over 21 comb lines. The measured comb is compared with the theoretical fit obtained setting the phase $\Delta\phi$ to 0.19 rad. (c) Phase delay difference $\Delta\phi$ as a function of the modulation frequency for $\Delta L = 500$ and 1 m. The right panel shows a magnification of the graph between 400 and 420 MHz for better clarity.

As a confirmation that the equalization effectively results from the interference between the two combs in Fig. 6.4b, we implemented Eq. 6.10 and 6.11 in a MATLAB script and varied $\Delta\phi$ to fit the equalized comb of Fig. 6.6b. The theoretical fit was obtained with a $\Delta\phi$ of 0.19 rad and setting β_{cw} and β_{ccw} to 14.8 and 13.2, respectively. The reason why these values differ from those retrieved from the experimental measurements in the single-pass configuration is due to the slightly different level of RF input power used, which in the case of the single-pass experiment was 11.5 dBm, while the equalized comb was acquired at 11.4 dBm. Nonetheless, Fig. 6.6b shows a good agreement between the theory and the experimental measurements, confirming that the interference between the frequency combs carried by the two counter-propagating waves within the Sagnac loop leads to an effective equalization of the output comb. Obviously, any phase value $\Delta\phi'$ such that $\cos(\Delta\phi') = \cos(0.19)$ would give the same theoretical fit. Specifically, if $\Delta\phi$ is the angle value between 0 and π that leads to the

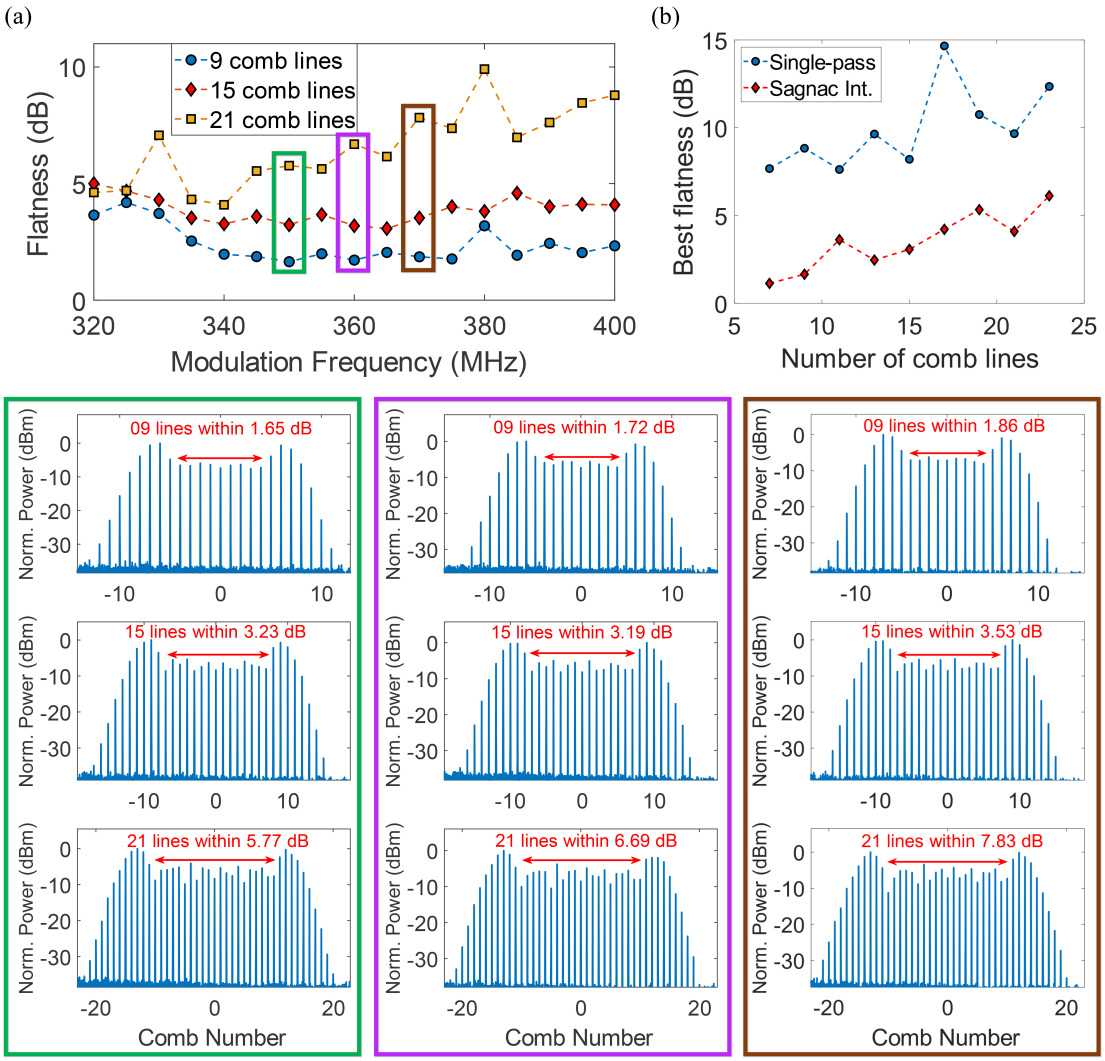

Figure 6.7 – (a) Flatness of the equalized EO comb spectra acquired at different modulation frequencies between 320 and 400 MHz for three different number of comb lines in the flat region. (b) Comparison of the best flatness obtained from the equalized combs acquired in the experiments with that calculated theoretically in case of single-pass configuration, plotted for different numbers of comb lines. Bottom panel: Comb spectra corresponding to a modulation frequency around 350 (green-bounded panel), 360 (violet-bounded panel), and 370 (brown-bounded panel) MHz. The spectra with a flat region of 9, 15 and 21 lines were acquired at RF powers of about 9.2, 10.4 and 11.5 dBm, respectively.

best flatness at a certain modulation frequency, an identical flat-topped comb can be attained at values $\Delta\phi' = \Delta\phi + 2N\pi$ or $\Delta\phi' = 2\pi(N+1) - \Delta\phi$, where N is an integer number.

Based on the above results, it seems that the comb equalization in this system is re-

stricted to only one modulation frequency, i.e. the frequency that provides the best bidirectional operation of the PM and the exact value of $\Delta\phi$ for the linear phase. However, we could obtain a quasi-flat-topped comb also at other modulation frequencies between 300 and 400 MHz at interval of about 5 MHz. This was possible thanks to the long fiber placed within the Sagnac loop. In fact, a much larger ΔL results in a steeper variation of the phase with the modulation frequency that leads to a more dense periodicity and, thus, allowing to find the right value of $\Delta\phi$ for a larger number of modulation frequencies. This concept is explained in Fig. 6.6c, where $\Delta\phi$ is plotted as a function of ω_m setting ΔL to 1 and 500 m. We note that, setting $\Delta L = 500$ m the phase span from 0 to 2π in a short range of frequencies, and harmonically repeats all over the frequency axis. Contrarily, with $\Delta L = 1$ m, the phase covers less than one harmonic cycle between 300 and 400 MHz.

By varying ω_m, also the power of the driving RF signal was slightly adjusted in order to find the corresponding bidirectional operation point of the PM. The values of the flatness calculated for the frequency combs acquired at different modulation frequencies between 300 and 400 MHz are shown in the top graph of Fig. 6.7a, while, on the bottom, there are the corresponding comb spectra at 350, 360 and 370 MHz. Each comb spectrum was acquired at different levels of power of the driving RF signal, resulting in directly proportional numbers of comb lines exhibited by the comb, which are identified on the graph by different colors and markers shapes. This variation of the RF power was much larger than that applied for finding the bidirectional operation point of the PM, where a more sensitive adjustment was required. From the graph in Fig. 6.7a we note that by increasing the number of comb lines the best flatness occurs at lower modulation frequencies. This might be due to the fact that by increasing the power of the RF signal, the best bidirectional operating point of the PM moves towards lower values of the modulation frequency. From the graphs of the comb spectra, we can see that they all show a flat-topped behavior, confirming a wide spectral range of effectiveness of the equalization effect. However, while the spectra with 9 and 15 comb lines in the flat region are characterized by a fairly constant flatness value, the combs with 21 lines show a strong degradation of the flatness with increasing the modulation frequency.

As a benchmark for these results, we calculated the theoretical values of the flatness for different number of comb lines in the central region, in case of combs generated in single-pass configuration, and compared with the best flatness obtained from the equalized combs acquired in the experiments. Figure 6.7b shows this comparison as a function of the corresponding number of comb lines in the central region. Since in the single-pass case the central region of the comb is not flat, the number of comb lines is determined within an interval $\Delta N = \pm(N_c - 2)$ around the central frequency. We note that the values of the flatness obtained in the single-pass case are much larger then those obtained experimentally with our system showing a flatness improvement ranging from 4 to 10 dB owing to the equalization provided by the Sagnac

Table 6.1 – Table showing a comparison in terms of performance and system complexity between the most common methods for the equalization of EO combs present in literature and the method proposed in this work. Pol. Mod.: polarization modulator; PS: phase shifter; DD-MZM: dual-drive Mach-Zehnder modulator.

			Complexity of the system	
Ref.	N° of comb lines	Flatness (dB)	Modulation	RF driving signal
[60]	29	1.5	1 MZM + 2 PM	1 RF source + 2 PS
[61]	25	< 1	2 Pol.Mod.	2 RF source
[64]	15	< 1	2 MZM	2 RF source
[67]	38	1	2 MZM + 1 PM	1 RF source + 1 PS
[68]	11	< 1	1 DD-MZM	2 RF source + 2 PS
[69]	9	< 2	1 DD-MZM	1 RF source + 1 PS
This work	9/15/21	1.65/3.19/4	1 PM	1 RF source

interferometer.

Table 6.1 shows a comparison in terms of performance and system complexity between the most common methods for the equalization of EO combs present in literature and the method proposed in this work. We note that, in terms of flatness, the performance of the Sagnac interferometer-based system, is competitive with that of the other proposed schemes in the case of 9 comb lines in the flat region, but less for the cases of 15 and 21 comb lines. However, there is a significant improvement in terms of complexity and cost compared to the other setups, thus offering a clear advantage from the point of view of the cost/performance ratio.

6.3 Summary

OFCs generated by a single-stage EOM, usually show a strong power imbalance between the comb lines, given their relationship with the Bessel functions of the first kind. Many setups have been proposed to solve this issue but most of them are implemented in relatively complex systems that require the use of two or more EOMs or a further processing of the driving RF signal. A simplified scheme, that provides an effective broadband EO comb equalization, has been demonstrated by driving a dual-drive MZM with slightly offsetted RF powers. In this chapter we have seen that a similar results can be obtained even in a fiber optic Sagnac interferometer using a conventional PM placed in an offset position from the loop midpoint and driven by only one RF sinusoidal signal. For the equalization to be effective, the PM must operate in a range of frequencies where it works bidirectionally and exhibits two slightly different modulation indexes such that the two counter-propagating combs in the loop are

complementary one with the other. The results have shown that an equalization, with various widths of the flat region, can be obtained for modulation frequencies between 320 and 400 MHz at intervals of 5 MHz. A comparison with the spectra obtained from the theory in case of combs generated in single-pass configuration, demonstrated a significant improvement of the flatness of the central region of the comb owing to the equalization provided by the Sagnac interferometer. Although limited to a specific range of frequencies, this setup offers a simple and cost-effective approach for the generation and the equalization of EO frequency combs since it requires only conventional off-the-shelf optical components.

7 Conclusions and outlook

The dream of an all-optical router capable to absolve all the functions of its electronic counterpart still presents several challenges that prevent it from becoming reality. Specifically, the buffering, i.e. the operation of delaying or storing of an optical signal, is a function that greatly affects the efficiency of modern optical transmission systems and is the most difficult to implement. In fact, there are three main characteristics that an ideal optical delay device has to fulfill: (1) the delay it provides should be tunable; (2) the characteristics of the delayed signal must be identical in every aspect to those of the input signal and (3) the system must be capable to accept signals with a wide frequency bandwidth.

The easiest way to delay a broadband pulse is to use an optical fiber. In this case, the delay achieved is simply related to the length of the fiber and the group velocity of the pulse. Obviously, this does not represents a compact solution for an optical buffer due to its considerable footprint. Optical resonators seem to offer a more compact and practical solution for the storage of pulses. Particularly, integrated photonic technology has reached a high level of maturity with the development of extremely high quality factors microresonators. However, as we have seen, they suffer from the restriction dictated by time-bandwidth limit (TBL), that forces to make a compromise between delay offered and bandwidth accepted.

This thesis addresses this issue either from the theoretical and experimental point of view, providing not only a practical method on how to overcome this limit, but also, and more importantly, a new insight of the time-bandwidth performance of a resonator. Inspired by a theoretical study that propose the breaking of the reciprocity property as a way to overcome the TBL [49], we imagined a resonant system with a nonreciprocal time-variant coupling interface. We performed a deep study on the spectral response and power balance of the system, showing that such a method provides effective benefits from the point of view of the intra-cavity power enhancement and the storage time. We chose to carry out this work through a simple macroscopic

fiber optic resonator based on the figure-9 cavity, since it allows to perfectly mimic a generic optical resonator in all the scenarios involving the storage of energy in case of nonreciprocal coupling. Although it does not represent the best efficient and compact solution, owing to the limitations mainly ascribable to the dispersion, in this contest it is actually used to demonstrate and implement a new insight of a physical principle. Also, its well known structure helped us in the mission of bringing the reader's attention more to the methods rather than the particular system used and its actual technological and practical advantages.

Certainly, an integrated device capable of providing the same remarkable time-bandwidth performance shown by the time-variant figure-9 resonator, would represent a more interesting approach. An exciting possibility, in fact, would be implementing the nonreciprocal coupling exploiting nonlinearity in coupled-microresonators [142, 143] or the spatiotemporal modulation in metamaterials [144]. In particular, the use of nonlinearity would allow to operate at a regime where the pulse duration is longer than the cavity round-trip time. However, in this case, the main challenge would be preserving both the waveform and spectral shape of the output pulse, a capability that is missing in the previous attempts [40, 43].

Beyond the experimental results obtained, which demonstrate that the nonreciprocal coupling in a generic resonant system unleashes arbitrarily high time-bandwidth performance, the theoretical analysis shows that the TBP is no longer related only to a limitation. Conversely, it represents a figure of merit, applicable to all kind of resonators, that gives an immediate estimation of the quantitative advantage, in terms of storage time and intra-cavity power enhancement, with respect to a standard reciprocal resonator. For instance, if a resonator exhibits a TBP of 40, I can immediately say, without any information on its structure, that it can provide an intra-cavity power enhancement 40 times stronger than a reciprocal resonator with the same cavity bandwidth, or it can store a signal for a period 40 times longer than its reciprocal counterpart with the same acceptance bandwidth.

Based on the versatile characteristics of the figure-9 resonator, we explored its potential also in the field of light generation. The features of its Sagnac-based structure have been first exploited for the development of a continuous-wave fiber laser using an Erbium-doped fiber as a gain element. The main aim of the project was to investigate theoretically and experimentally the dependence of the laser output performance from the coupling coefficient of the coupler. Interestingly, we found that the laser exhibits a strong dependence also on the phase difference between the two counter-propagating waves within the loop and, with a π phase difference, the laser transmission becomes independent on the coupling ratio of the coupler.

As a final stage of this thesis work, the Sagnac interferometer scheme has been used to realize a system for the generation and equalization of EO frequency combs. Although

the results obtained already show a significant improvement in terms of complexity and cost of the system, compared to the other approaches proposed in literature, the capabilities of this setup have not reached their highest level. In fact, we were limited technologically by the maximum RF input power provided by the RF amplifier. This prevented us to achieve larger widths of the flat region of the comb (more than 23 comb lines). Also the PM was already functioning at its maximum value of permitted input RF power. Therefore, we believe that a more performing set of equipment, that allow to overcome this technological constraints, would bring to even wider flat-topped frequency combs.

A Derivation of the acceptance bandwidth of a generic resonator

During the loading process the electric field $a_{\mathrm{L}}(t)$ inside the resonator grows exponentially at a rate $\rho_{\mathrm{L}}/2$, therefore we can write its expression as following:

$$a_{\mathrm{L}}(t) = a_{\mathrm{L}}(0) e^{\frac{\rho_{\mathrm{L}}}{2} t} e^{j\omega_0 t} u(-t) \tag{A.1}$$

where $u(t)$ is the Heaviside step function, ω_0 is the resonance frequency, while $a_{\mathrm{L}}(0)$ is the final value of $a_{\mathrm{L}}(t)$. The corresponding Fourier transform is:

$$a_{\mathrm{L}}(\omega) = \int_{-\infty}^{\infty} a_{\mathrm{L}}(t) e^{-j\omega t} = \int_{-\infty}^{0} a_{\mathrm{L}}(0) \exp\left[\frac{\rho_{\mathrm{L}}}{2} + j(\omega_0 - \omega)\right] t dt \;\Rightarrow$$

$$a_{\mathrm{L}}(\omega) = a_{\mathrm{L}}(0) \frac{\exp\left[\frac{\rho_{\mathrm{L}}}{2} + j(\omega_0 - \omega)\right] t}{\frac{\rho_{\mathrm{L}}}{2} + j(\omega_0 - \omega)} = -\frac{a_{\mathrm{L}}(0)}{j(\omega - \omega_0) - \frac{\rho_{\mathrm{L}}}{2}} \tag{A.2}$$

The expression of the energy inside the cavity is therefore:

$$|a_{\mathrm{L}}(\omega)|^2 = \frac{|a_{\mathrm{L}}(0)|^2}{(\omega - \omega_0)^2 - \frac{\rho_{\mathrm{L}}^2}{4}} \tag{A.3}$$

This is the Lorentzian function associated to the loading process, whose FWHM represents the acceptance bandwidth $\Delta\omega_{\mathrm{acc}}$ of the resonator and is given by:

$$\Delta\omega_{\mathrm{acc}} = \rho_{\mathrm{L}} \tag{A.4}$$

Bibliography

1. Kersey, A. & Morey, W. Multi-element Bragg-grating based fibre-laser strain sensor. *Electronics Letters* **29,** 964–966. (1993).
2. Koroshetz, J. *Fiber lasers for lidar* in *Optical Fiber Communication Conference, 2005. Technical Digest. OFC/NFOEC* (Anaheim, CA, USA, 2005), OFJ4. ISBN: 1-55752-783-0.
3. Dong, L. & Samson, B. in *Fiber Lasers - Basics, technology and applications* 255–268 (CRC Press, 2017). ISBN: 978-1-4987-2554-5.
4. Jang, J. K. *et al.* All-optical buffer based on temporal cavity solitons operating at 10 Gb/s. *Optics Letters* **41,** 4526–4529. ISSN: 15394794. (2016).
5. Leo, F. *et al.* Temporal cavity solitons in one-dimensional Kerr media as bits in an all-optical buffer. *Nature Photonics* **4,** 471–476. ISSN: 17494885. (2010).
6. Lukin, M. D. & Imamoğlu, A. Nonlinear optics and quantum entanglement of ultraslow single photons. *Physical Review Letters* **84,** 1419–1422. ISSN: 10797114. (2000).
7. Hu, H., Ji, D., Zeng, X., Liu, K. & Gan, Q. Rainbow trapping in hyperbolic metamaterial waveguide. *Scientific reports* **3,** 1249. (2013).
8. Demésy, G. & John, S. Solar energy trapping with modulated silicon nanowire photonic crystals. *J. Appl. Phys* **112.** (2012).
9. Eyderman, S. *et al.* Light-trapping optimization in wet-etched silicon photonic crystal solar cells. *J. Appl. Phys* **118.** (2015).
10. Eyderman, S. & John, S. Light-trapping and recycling for extraordinary power conversion in ultra-thin gallium-arsenide solar cells. *Scientific Reports* **6.** ISSN: 20452322. (2016).
11. Khurgin, J. B. Slow light in various media: a tutorial. *Advances in Optics and Photonics* **2,** 287–318. ISSN: 1943-8206. (2010).
12. Baba, T. Slow light in photonic crystals. *Nature Photonics* **2,** 465–473. (2008).
13. González-Herráez, M., Song, K.-Y. & Thévenaz, L. Optically controlled slow and fast light in optical fibers using stimulated Brillouin scattering. *Appl. Phys. Lett* **87,** 081113. (2005).

14. Schulz, S. A. *et al.* Dispersion engineered slow light in photonic crystals: a comparison. *Journal of Optics* **12,** 104004. ISSN: 2040-8978. (2010).
15. Thévenaz, L. Slow and fast light in optical fibres. *Nature Photonics* **2,** 474–481. ISSN: 17494885. (2008).
16. Krauss, T. F. Why do we need slow light? *Nature Photonics* **2,** 448–450. (2008).
17. John, S. Why trap light? *Nature Materials* **11,** 997–999. (2012).
18. Dorren, H. *et al.* Optical packet switching and buffering by using all-optical signal processing methods. *Journal of Lightwave Technology* **21,** 2–12. ISSN: 0733-8724. (2003).
19. Willner, A. E., Khaleghi, S., Chitgarha, M. R. & Yilmaz, O. F. All-optical signal processing. *Journal of Lightwave Technology* **32,** 660–680. ISSN: 07338724. (2014).
20. Deinega, A. & John, S. Solar power conversion efficiency in modulated silicon nanowire photonic crystals. *Journal of Applied Physics* **112,** 074327. ISSN: 00218979. (2012).
21. Okawachi, Y. *et al.* Tunable all-optical delays via brillouin slow light in an optical fiber. *Physical Review Letters* **94,** 153902. ISSN: 00319007. (2005).
22. Gan, Q., Fu, Z., Ding, Y. J. & Bartoli, F. J. Ultrawide-bandwidth slow-light system based on thz plasmonic graded metallic grating structures. *Physical Review Letters* **100,** 256803. ISSN: 00319007. (2008).
23. Cardenas, J. *et al.* Wide-bandwidth continuously tunable optical delay line using silicon microring resonators. *Optics Express* **18,** 26525–26534. ISSN: 1047-6938. (2010).
24. Xia, F., Sekaric, L. & Vlasov, Y. Ultracompact optical buffers on a silicon chip. *Nature Photonics* **1,** 65–71. ISSN: 17494885. (2007).
25. Khurgin, J. B. & Morton, P. A. Tunable wideband optical delay line based on balanced coupled resonator structures. *Optics Letters* **34,** 2655–2657. ISSN: 0146-9592. (2009).
26. Yoshiki, W. *et al.* All-optical tunable buffering with coupled ultra-high Q whispering gallery mode microcavities. *Scientific Reports* **7,** 8. ISSN: 20452322. (2017).
27. Sorin, W. V. & Tucker, R. S. Optical pulse storage, shaping, and wavelength conversion in resonators with controllable input coupling. *Journal of Lightwave Technology* **27,** 2587–2594. ISSN: 07338724. (2009).
28. Tucker, R. S., Ku, P.-C. & Chang-Hasnain, C. J. Slow-Light Optical Buffers: Capabilities and Fundamental Limitations. *Journal of Lightwave Technology* **23,** 4046–4066. (2005).

29. Boyd, R. W., Gauthier, D. J., Gaeta, A. L. & Willner, A. E. Maximum time delay achievable on propagation through a slow-light medium. *Physical Review A - Atomic, Molecular, and Optical Physics* **71,** 023801. ISSN: 10941622. (2005).

30. Khurgin, J. B. Performance limits of delay lines based on optical amplifiers. *Optics Letters* **31,** 948–950. (2006).

31. Van, V. *Optical microring resonators: theory, techniques, and applications* **1,** 297. ISBN: 9781315303505. (CRC Press, 2017).

32. Quimby, R. S. *Photonics and Lasers: An Introduction* 1–519. ISBN: 978-0-471-71974-8. (John Wiley & Sons, 2006).

33. Demtröder, W. *Laser Spectroscopy 1* 496. ISBN: 9780123821652. (Springer, 2014).

34. Khurgin, J. B. Dispersion and loss limitation on the performance of optical delay lines based on coupled resonant structures. *Optics Letters* **32,** 133–135. ISSN: 21622701. (2007).

35. Kippenberg, T. J., Holzwarth, R. & Diddams, S. A. Microresonator-based optical frequency combs. *Science* **332,** 555–559. ISSN: 10959203. (2011).

36. Kippenberg, T. J., Gaeta, A. L., Lipson, M. & Gorodetsky, M. L. Dissipative Kerr solitons in optical microresonators. *Science* **361,** eaan8083. ISSN: 0036-8075. (2018).

37. Poon, J. K. S., Scheuer, J., Xu, Y. & Yariv, A. Designing coupled-resonator optical waveguide delay lines. *Journal of the Optical Society of America B* **21,** 1665–1673. ISSN: 0740-3224. (2004).

38. Maleki, L., Matsko, A. B., Savchenkov, A. A. & Ilchenko, V. S. Tunable delay line with interacting whispering-gallery-mode resonators. *Optics Letters* **29,** 626–628. ISSN: 0146-9592. (2004).

39. Yanik, M. F., Suh, W., Wang, Z. & Fan, S. Stopping light in a waveguide with an all-optical analog of electromagnetically induced transparency. *Physical Review Letters* **93,** 233903. ISSN: 00319007. (2004).

40. Yanik, M. F. & Fan, S. Stopping and storing light coherently. *Physical Review A* **71,** 013803. ISSN: 10502947. (2005).

41. Wang, Z. & Fan, S. Compact all-pass filters in photonic crystals as the building block for high-capacity optical delay lines. *Physical Review E* **68,** 066616. ISSN: 1063651X. (2003).

42. Xu, Q. *et al.* Experimental realization of an on-chip all-optical analogue to electromagnetically induced transparency. *Physical Review Letters* **96,** 123901. ISSN: 00319007. (2006).

43. Xu, Q., Dong, P. & Lipson, M. Breaking the delay-bandwidth limit in a photonic structure. *Nature Physics* **3,** 406–410. ISSN: 17452473. (2007).

44. Harris, S. E. Electromagnetically induced transparency. *Physics Today* **50,** 36–42. ISSN: 00319228. (1997).

45. Vestergaard Hau, L., Harris, S. E., Dutton, Z. & Behroozi, C. H. Light speed reduction to 17 metres per second in an ultracold atomic gas. *Nature* **397,** 594–598. ISSN: 00280836. (Feb. 1999).

46. Ku, P. C., Chang-Hasnain, C. J. & Chuang, S. L. Variable semiconductor all-optical buffer. *Electronics Letters* **38,** 1581–1583. ISSN: 00135194. (2002).

47. Kim, J., Chuang, S. L., Ku, P. C. & Chang-Hasnain, C. J. Slow light using semiconductor quantum dots. *Journal of Physics Condensed Matter* **16,** S3727–S3735. ISSN: 09538984. (2004).

48. Sharping, J. E., Okawachi, Y. & Gaeta, A. L. Wide bandwidth slow light using a Raman fiber amplifier. *Optics Express* **13,** 6092–6098. (2005).

49. Tsakmakidis, K. L. *et al.* Breaking Lorentz reciprocity to overcome the time-bandwidth limit in physics and engineering. *Science* **356,** 1260–1264. ISSN: 0036-8075. (2017).

50. Caloz, C. *et al.* Electromagnetic Nonreciprocity. *Physical Review Applied* **10,** 047001. ISSN: 23317019. (2018).

51. Potton, R. J. Reciprocity in optics. *Reports on Progress in Physics* **67,** 717–754. ISSN: 00344885. (2004).

52. Mann, S. A., Sounas, D. L. & Alù, A. Nonreciprocal Cavities and the Time-Bandwidth Limit. *Optica* **6,** 104–110. ISSN: 2334-2536. (2019).

53. Tsang, M. Quantum limits on the time-bandwidth product of an optical resonator. *OPTICS LETTERS* **43,** 150–153. ISSN: 0146-9592. arXiv: 1709.10073. (2017).

54. Tsakmakidis, K., You, Y., Stefański, T. & Shen, L. Nonreciprocal cavities and the time-bandwidth limit: comment. *Optica* **7,** 1097–1101. ISSN: 2334-2536. (2020).

55. Alu, A., Mann, S. & Sounas, D. Nonreciprocal cavities and the time-bandwidth limit: reply. *Optica* **7,** 1102–1107. ISSN: 23342536. (2020).

56. Kang, J. U. in *Fiber Optic Sensing and Imaging* 119–146 (Springer, New York, NY, 2013). ISBN: 9781461474821. .

57. Cowle, G., Payne, D. & Reid, D. Single-frequency travelling-wave erbium-doped fibre loop laser. *Electronics Letters* **27,** 229–230. ISSN: 00135194. (1991).

58. Chernysheva, M. A., Krylov, A. A., Kryukov, P. G. & Dianov, E. M. Nonlinear amplifying loop-mirror-based mode-locked thulium-doped fiber laser. *IEEE Photonics Technology Letters* **24,** 1254–1256. ISSN: 10411135. (2012).

59. Kharitonov, S. & Brès, C.-S. *All-Fiber Dissipative Soliton Resonance Mode-locked Figure-9 Thulium-doped Fiber Laser* in *2017 European Conference on Lasers and Electro-Optics and European Quantum Electronics Conference, (Optical Society of America, 2017)* (2017), paper CJ_13_4. ISBN: 9781509067367.

60. Dou, Y., Zhang, H. & Yao, M. Generation of flat optical-frequency comb using cascaded intensity and phase modulators. *IEEE Photonics Technology Letters* **24,** 727–729. ISSN: 10411135. (2012).

61. He, C., Pan, S., Guo, R., Zhao, Y. & Pan, M. Ultraflat optical frequency comb generated based on cascaded polarization modulators. *Optics Letters* **37,** 3834–3836. ISSN: 0146-9592. (2012).

62. Fujiwara, M. *et al.* Optical Carrier Supply Module Using Flattened Optical Multicarrier Generation Based on Sinusoidal Amplitude and Phase Hybrid Modulation. *Journal of Lightwave Technology* **21,** 2705–2714. ISSN: 07338724. (Nov. 2003).

63. Plascak, M. E., Bustos Ramirez, R., Bagnell, K. & Delfyett, P. J. Tunable Broadband Electro-Optic Comb Generation Using an Optically Filtered Optoelectronic Oscillator. *IEEE Photonics Technology Letters* **30,** 335–338. ISSN: 10411135. (Feb. 2018).

64. Soto, M. A. *et al.* Optical sinc-shaped Nyquist pulses of exceptional quality. *Nature Communications* **4,** 2898. ISSN: 20411723. (2013).

65. Cordette, S., Vedadi, A., Shoaie, M. A. & Brès, C.-S. Bandwidth and repetition rate programmable Nyquist sinc-shaped pulse train source based on intensity modulators and four-wave mixing. *Optics Letters* **39,** 6668–6671. ISSN: 0146-9592. (Dec. 2014).

66. Fang, Y. *et al.* Frequency comb selection enabled flexible all optical Nyquist pulse generation. *Optics Communications* **349,** 60–64. ISSN: 00304018. (Aug. 2015).

67. Wu, R., Supradeepa, V. R., Long, C. M., Leaird, D. E. & Weiner, A. M. Generation of very flat optical frequency combs from continuous-wave lasers using cascaded intensity and phase modulators driven by tailored radio frequency waveforms. *Optics Letters* **35,** 3234–3236. ISSN: 0146-9592. arXiv: 1005.5373. (2010).

68. Yokota, N., Abe, K., Mieda, S. & Yasaka, H. Harmonic superposition for tailored optical frequency comb generation by a Mach–Zehnder modulator. *Optics Letters* **41,** 1026–1029. ISSN: 0146-9592. (2016).

69. Mishra, A. K. *et al.* Flexible RF-based comb generator. *IEEE Photonics Technology Letters* **25,** 701–704. ISSN: 10411135. (2013).

70. Wei, R. *et al.* Optical frequency comb generation based on electro-optical modulation with high-order harmonic of a sine RF signal. *Optics Communications* **291,** 269–273. ISSN: 00304018. (Mar. 2013).

71. Fan, S., Suh, W. & Joannopoulos, J. D. Temporal coupled-mode theory for the Fano resonance in optical resonators. *Journal of the Optical Society of America A* **20,** 569–572. ISSN: 1084-7529. (2003).

72. Fan, S. in *Optical Fiber Telecommunications V A* (eds Kaminow, I. P., Li, T. & Willner, A. E.) 5th, 160 (Elsevier, 2008). ISBN: 9780123741714.

73. Joannopoulos, J. D., Johnson, S. G., Winn, J. N. & Meade, R. D. in *Photonic crystals: molding the flow of light* 2nd, 197–203 (Princeton University Press, 2008). ISBN: 1400828244. eprint: 1011.1669.

74. Yariv, A. Universal relations for coupling of optical power between microresonators and dielectric waveguides. *Electronics Letters* **36,** 321–322. ISSN: 00251569. (2000).

75. Yariv, A. & Yeh, P. *Photonics : Optical Electronics in Modern Communications* 6th. (Oxford University Press Inc, New York, United States, 2006).

76. Siegman, A. E. *Lasers_Book* ISBN: 0935702113. (Universitz Science Book, 1986).

77. Hecht, E. *Optics, 5th Edition* ISBN: 9780133979121. (Pearson, 2016).

78. Haus, H. A. & Huang, W. Coupled-Mode Theory. *Proceedings of the IEEE* **79,** 1505–1518. (1991).

79. Haus, H. A. *Waves and Fields in Optoelectronics* 415. ISBN: 0-13-946053-5 (Prentice-Hall, 1984).

80. Zhao, Z., Guo, C. & Fan, S. Connection of temporal coupled-mode-theory formalisms for a resonant optical system and its time-reversal conjugate. *Physical Review A* **99,** 33839. (2019).

81. Leuchs, G. & Sondermann, M. Time-reversal symmetry in optics. *Physica Scripta* **85,** 058101–1 –4. ISSN: 00318949. arXiv: 1205.1374. (2012).

82. Heugel, S., Villar, A. S., Sondermann, M., Peschel, U. & Leuchs, G. On the analogy between a single atom and an optical resonator. *Laser Physics* **20,** 100–106. (2010).

83. Sedra, A. S. & Smith, K. C. in *Microelectronic Circuits* 7th ed. Chap. 2 (Oxford Universitz Press, 2014). ISBN: 9780199339136.

84. Koechner, W. *Solid-State Laser Engineering* 6th ed. ISBN: 978-0-387-29094-2. (Springer-Verlag New York, 2006).

85. Milonni, P. & Eberly, J. in *Laser Physics* (ed John Wiley & Sons, I.) 141–173 (2010). ISBN: 9780470409718.

86. Hodgson, N. & Weber, H. in *Optical Resonators* 303–326 (Springer-Verlag London, 1997). ISBN: 978-1-4471-3595-1.

87. Valerii, T.-M. in *Fundamentals of Fiber Lasers and Fiber Amplifiers* chap. 7 (Springer, 2014). ISBN: 978-3-319-02338-0.

88. McNaught, A. D. *Compendium of Chemical Terminology* (ed Blackwell Science Inc) ISBN: 0-86542-684-8. (IUPAC, 1997).

89. Becker, P., Olsson, N. & Simpson, J. in *Erbium-doped fiber amplifiers* chap. 5 (Academic Press, 1999). ISBN: 9780080505848.

90. Runge, A. F. J., Aguergaray, C., Provo, R., Erkintalo, M. & Broderick, N. G. R. All-normal dispersion fiber lasers mode-locked with a nonlinear amplifying loop mirror. *Optical Fiber Technology* **20,** 657–665. (2014).

91. Smith, K., Doran, N. J. & Wigley, P. G. Pulse shaping, compression, and pedestal suppression employing a nonlinear-optical loop mirror. *Optics letters* **15,** 1294–1296. ISSN: 0146-9592. (1990).

92. Kim, J. & Song, Y. Ultralow-noise mode-locked fiber lasers and frequency combs: principles, status, and applications. *Advances in Optics and Photonics* **8,** 465–540. ISSN: 1943-8206. (2016).

93. Duling III, I. N. All-fiber ring soliton laser mode locked with a nonlinear mirror. *Optics Letters* **16,** 539–541. ISSN: 0146-9592. (1991).

94. Kharitonov, S. & Brès, C.-S. Isolator-free unidirectional thulium-doped fiber laser. *Light: Science & Applications* **4,** e340. (2015).

95. Heebner, J. E. & Boyd, R. W. Enhanced all-optical switching by use of a nonlinear fiber ring resonator. *Optics letters* **24,** 847–849. ISSN: 0146-9592. (1999).

96. Qiang, Z., Zhou, W. & Soref, R. A. Optical add-drop filters based on photonic crystal ring resonators. *Optics Express* **15,** 1823–1831. (2007).

97. Jinno, M. & Matsumoto, T. Nonlinear Sagnac Interferometer Switch and Its Applications. *IEEE Journal of Quantum Electronics* **28,** 875–882. ISSN: 15581713. (1992).

98. Little, B. E. *et al.* Ultra-Compact Si – SiO Microring Resonator optical channel dropping filters. *IEEE Photonics Technology Letters* **10,** 549–551. ISSN: 1041-1135. (1998).

99. Mortimore, D. B. Fiber Loop Reflectors. *Journal of Lightwave Technology* **6,** 1217–1224. ISSN: 15582213. (1988).

100. Doran, N. J. & Wood, D. Nonlinear-optical loop mirror. *Optics Letters* **13,** 56–58. ISSN: 0146-9592. (1988).

101. Fermann, M. E., Haberl, F., Hofer, M. & Hochreiter, H. Nonlinear amplifying loop mirror. *OPTICS LETTERS* **15,** 752–754. (1990).

102. Ja, Y. H. An unsymmetric S-shaped double-coupler optical fibre loop. *Optics Communications* **78,** 81–89. (1990).

103. Ja, Y. H. A spectacles-shaped optical fibre ring resonator with two couplers. *Optical and Quantum Electronics* **23,** 379–389. (1991).

104. Ja, Y. H. Single-mode optical fiber ring and loop resonators using degenerate two-wave mixing. *Applied optics* **30,** 2424–2426. ISSN: 0003-6935. (1991).

105. Ja, Y. H. Simultaneous resonance of an S-shaped two-coupler optical fibre ring resonator. *Optics Communications* **102,** 133–140. ISSN: 00304018. (1993).

106. Pfeiffer, T. & Bülow, H. Analytical Gain Equation For Erbium-Doped Fiber Amplifiers Including Mode Field Profiles And Dopant Distribution. *IEEE Photonics Technology Letters* **4,** 449–451. ISSN: 19410174. (1992).

107. Asadchy, V. S., Mirmoosa, M. S., Diaz-Rubio, A., Fan, S. & Tretyakov, S. A. Tutorial on Electromagnetic Nonreciprocity and Its Origins. *Proceedings of the IEEE* **108,** 1684–1727. ISSN: 0018-9219. (Aug. 2020).

108. Wang, K. X. Time-reversal symmetry in temporal coupled-mode theory and nonreciprocal device applications. *Optics Letters* **43,** 5623–5626. ISSN: 0146-9592. (2018).

109. Ismail, N., Kores, C. C., Geskus, D. & Pollnau, M. Fabry-Pérot resonator: spectral line shapes, generic and related Airy distributions, linewidths, finesses, and performance at low or frequency-dependent reflectivity. *Optics Express* **24,** 16366–16389. ISSN: 1094-4087. (2016).

110. Upham, J. *et al.* The capture, hold and forward release of an optical pulse from a dynamic photonic crystal nanocavity. *Optics Express* **21,** 3809–3817. (2013).

111. Tanabe, T., Notomi, M., Taniyama, H. & Kuramochi, E. Dynamic release of trapped light from an ultrahigh-Q nanocavity via adiabatic frequency tuning. *Physical Review Letters* **102,** 043907. ISSN: 00319007. (2009).

112. Sokoloff, J. P., Prucnal, P. R., Glesk, I. & Kane, M. A Terahertz Optical Asymmetric Demultiplexer (TOAD). *IEEE Photonics Technology Letters* **5,** 787–790. ISSN: 19410174. (1993).

113. Agrawal, G. P. *Lightwave Technology: Telecommunication Systems* 1–461. ISBN: 0471215724. (2005).

114. Forrester, A. T. Photoelectric Mixing As a Spectroscopic Tool. *Journal of the Optical Society of America* **51,** 253–259. ISSN: 0030-3941. (1961).

115. Cundiff, S. T. & Ye, J. Colloquium: Femtosecond optical frequency combs. *Reviews of Modern Physics* **75,** 325–342. ISSN: 00346861. (2003).

116. Droste, S., Ycas, G., Washburn, B. R., Coddington, I. & Newbury, N. R. Optical Frequency Comb Generation based on Erbium Fiber Lasers. *Nanophotonics* **5,** 196–213. ISSN: 21928614. (2016).

117. Udem, T., Holzwarth, R. & Hänsch, T. Femtosecond optical frequency combs. *European Physical Journal: Special Topics* **172,** 69–79. ISSN: 19516355. (2009).

118. Durán, V., Schnébelin, C. & Guillet de Chatellus, H. Coherent multi-heterodyne spectroscopy using acousto-optic frequency combs. *Optics Express* **26,** 13800–13809. ISSN: 1094-4087. (2018).

119. Parriaux, A., Hammani, K. & Millot, G. Electro-optic frequency combs. *Advances in Optics and Photonics* **12,** 223–287. ISSN: 1943-8206. (2020).

120. Del'Haye, P. *et al.* Optical frequency comb generation from a monolithic microresonator. *Nature* **450,** 1214–1217. ISSN: 14764687. arXiv: 0708.0611. (2007).

121. Pasquazi, A. *et al.* Micro-combs: A novel generation of optical sources. *Physics Reports* **729,** 1–81. ISSN: 03701573. (Jan. 2018).

122. Picqué, N. & Hänsch, T. W. Frequency comb spectroscopy. *Nature Photonics* **13,** 146–157. ISSN: 17494893. (2019).

123. Udem, T., Holzwarth, R. & Hänsch, T. W. Optical frequency metrology. *Nature* **416,** 233–237. ISSN: 00280836. (2002).

124. Trocha, P. *et al.* Ultrafast optical ranging using microresonator soliton frequency combs. *Science* **359,** 887–891. ISSN: 10959203. arXiv: 1707.05969. (Feb. 2018).

125. Suh, M. G. & Vahala, K. J. Soliton microcomb range measurement. *Science* **359,** 884–887. ISSN: 10959203. arXiv: 1705.06697. (2018).

126. Hillerkuss, D. *et al.* 26 Tbit s-1 line-rate super-channel transmission utilizing all-optical fast Fourier transform processing. *Nature Photonics* **5,** 364–371. ISSN: 17494885. (2011).

127. Torres-Company, V. & Weiner, A. M. Optical frequency comb technology for ultrabroadband radio-frequency photonics. *Laser & Photonics Reviews* **8,** 368–393. ISSN: 18638880. (2014).

128. Gaeta, A. L., Lipson, M. & Kippenberg, T. J. Photonic-chip-based frequency combs. *Nature Photonics* **13,** 158–169. ISSN: 17494893. (2019).

129. Jiang, Z., Huang, C. B., Leaird, D. E. & Weiner, A. M. Optical arbitrary waveform processing of more than 100 spectral comb lines. *Nature Photonics* **1,** 463–467. ISSN: 17494885. (2007).

130. Yan, X., Zou, X., Pan, W., Yan, L. & Azaña, J. Fully digital programmable optical frequency comb generation and application. *Optics Letters* **43,** 283–286. ISSN: 0146-9592. (2018).

131. Bao, Y. *et al.* A digitally generated ultrafine optical frequency comb for spectral measurements with 0.01-pm resolution and 0.7-μs response time. *Light: Science and Applications* **4,** e300. ISSN: 20477538. (2015).

132. Sakamoto, T., Kawanishi, T. & Izutsu, M. Asymptotic formalism for ultraflat optical frequency comb generation using a Mach-Zehnder modulator. *Optics Letters* **32,** 1515–1517. ISSN: 0146-9592. (2007).

133. Sakamoto, T., Kawanishi, T. & Tsuchiya, M. 10 GHz, 24 ps pulse generation using a single-stage dual-drive Mach-Zehnder modulator. *Optics Letters* **33,** 890–892. ISSN: 0146-9592. (2008).

134. Wang, Q., Huo, L., Xing, Y. & Zhou, B. Ultra-flat optical frequency comb generator using a single-driven dual-parallel Mach–Zehnder modulator. *Optics Letters* **39,** 3050–3053. ISSN: 0146-9592. (2014).

135. Zhang, M. *et al.* Broadband electro-optic frequency comb generation in a lithium niobate microring resonator. *Nature* **568,** 373–377. ISSN: 14764687. (2019).

136. Torres-Company, V., Lancis, J. & Andrés, P. Lossless equalization of frequency combs. *Optics Letters* **33,** 1822–1824. ISSN: 0146-9592. (2008).

137. Chen, C. *et al.* Generation of a flat optical frequency comb based on a cascaded polarization modulator and phase modulator. *Optics Letters* **38,** 3137–3139. ISSN: 0146-9592. (2013).

138. Couch, L. W. *Digital and Analog Communication Systems* 8th ed., 336–337. ISBN: 9780874216561. (Pearson, 2012).

139. Dong, P. Travelling-wave Mach-Zehnder modulators functioning as optical isolators. *Optics Express* **23,** 10498–10505. ISSN: 1094-4087. (2015).

140. Becker, R. A. Traveling-wave electro-optic modulator with maximum bandwidth-length product. *Appl. Phys. Lett* **45,** 1168–1170. (1984).

141. Guo, H. *et al.* Single-Arm Frequency-Shifted Interferometry Using a Bidirectional Electro-Optic Modulator. *Journal of Lightwave Technology* **37,** 1310–1316. ISSN: 07338724. (Feb. 2019).

142. Rodriguez, S. R. K., Goblot, V., Zambon, N. C., Amo, A. & Bloch, J. Nonreciprocity and zero reflection in nonlinear cavities with tailored loss. *Physical Review A* **99,** 013851. (2019).

143. He, B., Yang, L., Jiang, X. & Xiao, M. Transmission Nonreciprocity in a Mutually Coupled Circulating Structure. *Physical Review Letters* **120,** 203904. ISSN: 10797114. (2018).

144. Chen, Y. *et al.* Nonreciprocal Wave Propagation in a Continuum-Based Metamaterial with Space-Time Modulated Resonators. *Physical Review Applied* **11,** 064052. ISSN: 23317019. (2019).

IVAN CARDEA

CONTACT

+41 78 403 2457

ivancardea@gmail.com

ivancardea

Ch. de Chantemerle, 12
1010, Lausane, Switzerland

Citizenship: Italian
(with type B residence permit)

NETWORK

facebook.com/ivan.cardea

twitter.com/ivancardea

linkedin.com/in/ivan-cardea
-63894166

LANGUAGES

Italian

English

French

CORE COMPETENCIES

Optical and radio-frequency (RF) communications: engineering of novel transmission systems in the RF and optical frequency domain based on advanced modulation formats.

Fiber lasers and optical resonators: design, modeling and implementation of customized fiber lasers and optical resonant systems.

Electro-optic frequency combs: realization of opto-electronic systems for the generation and equalization of electro-optic frequency combs.

EDUCATION

Ph.D. in Photonics

Photonic Systems Laboratory at EPFL, Switzerland 2020

Major: Fiber optic resonators and electro-optic frequency combs

MSc in Electronic Engineering

University of Pavia, Italy 2016

Specialization: Photonics, optical communication systems and networks. *Final Grade: 110/110 with honors*.

BSc in Electronic and Telecommunication Engineering

Polytechnic of Bari, Italy 2013

Multidisciplinary program with a focus on Microelectronics and Telecommunications. *Final Grade: 105/110*

CORE EXPERIENCE

Research and teaching assistant

Photonic Systems Laboratory at EPFL, Switzerland 2016 - 2020

- Theoretical modeling and experimental characterization of fiber optic resonators and fiber lasers.
- Design and implementation of optical fiber systems for efficiently storing multiple pulses without detectable distortions.
- Realization of an interferometric optical fiber system for the equalization and optimization of electro-optic frequency combs.

Research student assistant

2015 - 2016

Optoelectronic Research Centre, University of Southampton, UK

- Design and implementation of a short-reach optical transmission system based on discrete multi-tone modulation for high bit rate data-centre
- Numerical simulations of complex optical communication systems using MathWorks Simulink.

Research student assistant

Integrated Photonics Laboratory, University of Pavia, Italy Feb - Apr 2012

Study and characterisation of hydrogenated amorphous silicon waveguides (a-Si:H) for integrated optical devices.

ADDITIONAL EXPERIENCE

Web designer

Assbenaz di Emiliano Bonassi 2013 - 2014

Responsible for the websites graphic design and content editing.

Commercial agent

INDDE di Marco Francesco Carrino 2008 - 2011

Responsible for the sale of “Livù Magazine” and distribution of third parties commercial material.

OTHER ACTIVITIES

President of Cinetyk Student Association

Polytechnic of Bari, Italy 2011 - 2013

Responsible for the direction of the activities planned and voted by the association directive board.

Student Representative

Polytechnic of Bari, Italy 2011 - 2012

Representative of the students at the Council of the Engineering Department.

SOFTWARE KNOWLEDGE

Expert

- MATLAB and Simulink
- VPI Transmission Maker Optical System
- LabView
- Adobe Photoshop
- Microsoft Office
- iWork
- Latex

Familiar with

- Origin
- Adobe Illustrator
- BeamPROP
- Mathematica

MAIN PUBLICATIONS

International peer reviewed journal publications

- C. Lacava, I. **Cardea, I**. Demirtzioglou, A.E. Khoja, Li Ke, D. J. Thomson, X. Ruan, F. Zhang, G.T. Reed, D.J. Richardson, and P. Petropoulos, "49.6 Gb/s direct detection DMT transmission over 40 km single mode fibre using an electrically packaged silicon photonic modulator," *Opt. Express* 25, 29798-29811 (2017).
- **I. Cardea**, D. Grassani, S. J. Fabbri, J. Upham, R. W. Boyd, H. Altug, S. A. Schulz, K. L. Tsakmakidis, and C.-S. Brès, “Arbitrarily high time bandwidth performance in a nonreciprocal optical resonator with broken time invariance, *Sci. Rep.* 10, 15752 (2020).
- **I. Cardea**, D. Grassani, J. Upham, S. A. Schulz, K. L. Tsakmakidis, and C.-S. Brès, “Unconventional time-bandwidth performance of resonant cavities with nonreciprocal coupling”, *Physical Review A.* (2020), (*accepted*).

INTERESTS

Sport // **Music** // **Cinema** // **Technology** // **Board Games**

REFERENCES

Prof. Camille-Sophie Brès

Photonic Systems Laboratory, EPFL-STI-IEL-PHOSL, Station 11, 1015 Lausanne, Switzerland.

Phone: +41 21 693 7866
camille.bres@epfl.ch

Prof. Periklis Petropoulos

Optoelectronics Research Centre, University of Southampton, University Rd SO17 1BJ Southampton, United Kingdom

Phone: +44 23 805 92014
pp@orc.soton.ac.uk

Dr. Cosimo Lacava

Integrated Photonics Laboratory, University of Pavia, via A. Ferrata, 5 27100 Pavia, Italy

Phone: +39 0382 985221
cosimo.lacava@unipv.it

RELEVANT COURSES

- Antennas and Propagation
- Applied Electronics
- Automatic Controls
- Business Management
- Digital and Analog Communication Systems
- Electronic Instrumentation
- Electronic Devices for Information Systems
- Industrial Laser Design
- Integrated Optics
- Microwave Devices
- Nonlinear Optics
- Optical Communications
- Optical Fibers and Fiber Devices
- Optoelectronic Devices
- Quantum Electronics
- Semiconductor Device Physics